

ALMA MATER STUDIORUM
UNIVERSITA' DI BOLOGNA

SCUOLA DI INGEGNERIA E ARCHITETTURA
- Sede di Forlì -

CORSO DI LAUREA
IN INGEGNERIA AEROSPAZIALE
Classe L-20

TESI DI LAUREA IN DINAMICA E CONTROLLO ORBITALE

Sea Level Measurement Using Single GNSS Antenna SNR Signals

Student: Pietro Rauzi

Main Supervisor: Prof. Paolo Tortora

Tutor: Prof. Alessandro Avanzi

Anno Accademico 2012/2013

Sessione III

*To Mattia, Giulio, Cristina et Andrea,
who have believed in me since the beginning
and sustained my journey of discovery*

*"Even in the Darkest of Suffering a Man can Sleep,
But for the Man Who Inflicts that Suffering, his Mind Cannot Rest, Ever"*

Abstract

This thesis presents a possible method to calculate sea level variation using geodetic-quality Global Navigation Satellite System (GNSS) receivers. Three antennas are used: two small antennas and a choke ring one, analyzing only Global Positioning System signals. The main goal of the thesis is to test a modified configuration for antenna set up. In particular, measurements obtained tilting one antenna to face the horizon are compared to measurements obtained from antennas looking upward. The location of the experiment is a coastal environment nearby the Onsala Space Observatory in Sweden. Sea level variations are obtained using periodogram analysis of the SNR signal and compared to synthetic gauge generated from two independent tide gauges. The choke ring antenna provides poor result, with an RMS around 6 cm and a correlation coefficients of 0.89. The smaller antennas provide correlation coefficients around 0.93. The antenna pointing upward present an RMS of 4.3 cm and the one pointing the horizon an RMS of 6.7 cm. Notable variation in the statistical parameters is found when modifying the length of the interval analyzed. In particular, doubts are risen on the reliability of certain scattered data. No relation is found between the accuracy of the method and weather conditions. Possible methods to enhance the available data are investigated, and correlation coefficient above 0.97 can be obtained with small antennas when sacrificing data points. Hence, the results provide evidence of the suitability of SNR signal analysis for sea level variation in coastal environment even in the case of adverse weather conditions. In particular, tilted configurations provides comparable result with upward looking geodetic antennas.

A SNR signal simulator is also tested to investigate its performance and usability. Various configuration are analyzed in combination with the periodogram procedure used to calculate the height of reflectors. Consistency between the data calculated and those received is found, and the overall accuracy of the height calculation program is found to be around 5 mm for input height below 5 m. The procedure is thus found to be suitable to analyze the data provided by the GNSS antennas at Onsala.

Abstract

La presente tesi tratta di un possibile metodo per ottenere informazioni riguardanti la variazione del livello del mare utilizzando ricevitori di segnali appartenenti al Global Navigation Satellite System (GNSS), utilizzati per studi geodetici. Tre diverse configurazioni sono analizzate che prevedono l'utilizzo di due tipologie di antenna, una "choke ring" e due antenne a disco più piccole. Nello studio si osserveranno unicamente segnali provenienti dal sistema Global Positioning System (GPS). Lo scopo principale della tesi è di analizzare una nuova configurazione, costituita da un'antenna ruotata rispetto alla normale disposizione, in modo da puntare l'orizzonte. Le rilevazioni compiute con tale layout sono poi confrontate con le altre antenne in configurazione standard. Il luogo dove è stato compiuto l'esperimento è l'Osservatorio Spaziale di Onsala (OSO) in Svezia. La variazione del livello del mare è calcolata analizzando il periodogramma del rapporto segnale rumore (SNR) del segnale. Questa è poi confrontata con una sonda artificiale ottenuta combinando dati provenienti da sensori di marea localizzati in zone limitrofe. L'antenna di dimensioni maggiori presenta i dati più scarsi, con uno scarto quadratico medio (SQM) di 6 cm ed un coefficiente di correlazione pari a 0.89. Le antenne più piccole presentano invece coefficiente intorno a 0.93. Lo scarto quadratico medio per l'antenna diretta verso l'alto si assesta sui 4.3 cm mentre per la nuova configurazione sui 6.7 cm. Una notevole variazione di tali grandezze è osservabile al variare dell'intervallo temporale osservato. In particolare, dei dubbi sono sollevati sull'affidabilità di specifici dati poco congruenti, causa principale del degrado dei parametri statistici. Non viene specificata nessuna particolare relazione diretta tra l'accuratezza del metodo e le condizioni atmosferiche, eccetto per un possibile influenza dovuta alla direzione del vento. E' inoltre investigata la possibilità di aumentare la qualità dei dati in possesso, ottenendo coefficienti di correlazioni di poco superiori a 0.97 ma sacrificando alcuni dati. I risultati ottenuti dimostrano quindi la concreta possibilità di utilizzazione del valore del SNR per il tracking della variazione del livello del mare in ambienti costieri anche in caso di condizioni atmosferiche avverse. In particolare, modificando la configurazione e ruotando l'antenna è possibile ottenere risultati comparabili con antenne geodetiche posizionate tradizionalmente lungo la perpendicolare.

In aggiunta, si è analizzato un simulatore di valore di SNR, ai fini di testarne le performance e la possibilità di utilizzo. Numerose configurazioni vengono esaminate e verificate in combinazione con il programma di analisi utilizzato in seguito per il calcolo dell'altezza del livello del mare. Viene osservato un certo grado di corrispondenza tra i dati simulati e quelli ricevuti durante la campagna test. La precisione ottenuta, utilizzando come input altezze della superficie riflettente non superiore a 5 m, è di circa 5 mm. Il procedimento risulta quindi essere adeguato per l'analisi dei dati proveniente dai ricevitori posizionati all'osservatorio di Onsala.

THIS PAGE WAS INTENTIONALLY LEFT BLANK

Introduction

Nowadays, measuring the sea level has gained more and more importance in order to analyze its impact on current societies. In fact, this not only modifies the environment of coastal societies, but it also affects the inland due to economic interdependence. The melting of ice mass in the polar region could bring to increment of the sea level and thus to mass migration to inner localities. Salinity is also affected by the sea level, and thus also evaporation, precipitation and capacity of natural storage and supply of fresh water. The change on water precipitation could also alter the agriculture production (Watkins, 2007). Planned measurements of the sea level could bring to a better understanding of the global warming phenomenon. In this manner it would be possible to predict future development of sea level. It could also bring to a more clear determination of the behavior of underwater stream. These drive high quantity of energy thought the world and deeply affect local weather conditions (Bindoff et al., 2007).

Usually, the trend of the sea level has always been kept under control with the aid of tide gauges. These typically perform the measurements by mean of mechanical sensors. In one of these cases, pressure variation of a water column is calculated through Pascal Law. Other sensors that can be found for this porpoise are stilling wells sensors, sometimes combined with the previous model. Acoustic and Radar (for which temperature and humidity are not relevant) gauges have been also used to achieve the same task. These have the advantage of avoiding the usage of moving part and sometime the direct contact with water. While this kind of sensors produces an accurate and frequent observation of the behavior of the sea, their power consumption is relatively large and they do not guarantee a full coastal coverage (Loddè,

2006). A general problem that affects these sensors though is the lack of direct information regarding the ground motions. This could generate errors in the results due to the movement of the reference points.

An alternative and aiding system to retrieve sea level measurements can be retrieved by means of the GNSS widespread infrastructure. GNSSs or *Global Navigation Satellite Systems* indicates a family of systems whose goal is to provide information about the user's position and velocity. The signal is transmitted by satellites all over the world at any time. One of the most famous systems is the Global Positioning System or GPS, supervised by the US Government. One common problem related to satellite-based navigation, is the presence of obstacle and objects throughout the path of the signals. These generate the phenomenon called "*Multipath*". This refers to the multiple paths that the signal travels being reflected by third objects in order to arrive to the receiver. Using this unwanted signal it is possible to gain useful information about the reflecting surfaces.

An abundant number of receivers are nowadays already spread all over the world for various purposes, mostly for geodesy studies such as tectonic movement and other local ground motion. Analyzing the GNSS signals could bring in this case not only to calculate this land surface movement of the crust, but also to a combined detection of the changing on sea level (Löfgren et al.2011; Larson et al., 2012; Lowe et al, 2002). In this manner the problems related to lack of direct information regarding the ground movement would be resolved. Moreover, GNSS perform well also in case of tough weather conditions (Larson, 2012).

In this thesis, the goal is to achieve sea level measurements by mean of GNSS detection using two different antennas. Three different installations will be tested featuring two different antennas. The determination of the sea level will be carried out analyzing the multipath effect, i.e. the reflection of the signal by the sea surface. A software simulator will be also used to simulate the GNSS receiving signal. In this way it will be possible to observe the behavior of the signal in case of variation of physical parameters. Before this, the simulator will be tested in order to verify its reliability. Furthermore, a set of data collected on the coast of Sweden (Onsala) will be processed in order to calculate the sea level. All three configurations will be observed and the measurements will be compared. Finally, the most suitable setup for sea level measurements will be determined.

Contents

Introduction	I
1. Global Navigation Satellite Systems.....	1
1.1. Introduction	1
1.2. The GPS: Global Positioning System	2
1.2.1. Constellation	2
1.2.2. Features and usages of the main signal	3
1.2.3. Modernization.....	5
1.3. Other Systems.....	6
2. GPS Surface Sensing.....	7
2.1. Introduction	7
2.2. Reflection theory, multipath and SNR	8
2.3. Lomb Spargle Periodogram.....	17
2.4. Previous Experiments	18
3. Antennas	21
3.1. Introduction	21
3.2. LEICA AT 504GG	22
3.3. LEICA AX 1202GG	26
4. The Simulator	29
4.1. Introduction	29
4.2. Simulator output: SNR Trends	31
4.2.1. Height.....	32
4.2.2. Antenna Orientation	34
4.2.3. Polarization	35
4.2.4. Observations	36
4.2.5. Surface material.....	37
4.3. Testing procedure for simulated results.....	38
4.4. Simulation setup and height calculation.....	39
4.5. Test results and discussion	43
5. Sea Level Measurements	51
5.1. Introduction	51
5.2. Experiment Configurations	51

5.3.	Experiment Parameters and Physical Constraints.....	55
5.4.	DATA Acquisition and Pressure Gauges.....	59
5.5.	Software and Procedure	65
5.6.	Results.....	71
5.6.1.	Sea level Variation	71
5.6.2.	Error distribution and statistical parameter variation.....	76
5.6.3.	Antenna Comparison	80
5.6.4.	Weather Conditions.....	81
5.6.5.	Interpolation and smoothing	84
5.6.6.	Coupled antennas improvements.....	88
5.6.7.	Total Campaign Dataset.....	90
5.7.	Discussion	97
6.	Conclusions	103
6.1.	Simulator.....	103
6.2.	Sea Level Measurements.....	103
7.	Future Work.....	105
8.	References	107
9.	Appendix	111
9.1.	Basic Functioning of the Simulator	111
9.2.	Scripts	115
	Acknowledgments	117

1. Global Navigation Satellite Systems

1.1. Introduction

Navigation and position acquisition have always been linked, from the dawn of times. They have also played an important role in human history of discovery and exploration. Our ancestors were relying on calculating the position of the stars from their location with astrolabes and quadrants. Firstly known as “The Antikythera mechanism”, the former is known to be used since the II sec. A.D. (IMSS, 2004). The development on communication science has brought to the implementation of more accurate systems. We still look at the sky, but instead of stars this time we search for signal transmitting systems. These take the name of GNSSs: Global Navigation Satellite Systems and consist of three main “segments”. The Space Segment, a constellation of satellites, that we could call our stars. Instead of calculating the position of these space vehicles by means of astrolabe, we measure the distance from the satellites to a signal receiver, what it is called the User Segment. The receiver is created in order to detect the signal and demodulating it. This allows to retrieve the distance to the satellite and the velocity with respect to the space vehicle, if moving. For this reason this is called a PVT system, or Position, Velocity and Time. Time in fact is very important to correlate the time of the signal of the receiver and the one of the signal of the transmitter and correct possible relativity errors. The signal received by the receiver also contains a message modulated into the carrier. This provides high precision on the position of the satellite, time variation and it enhances the accuracy of the positioning (Misra, 2011). This is done by the aiding of what is called the Control Segment: a system of land structures that provide refinements to the service. This is done by comparing the position calculated through the GNSS with the known position of ground

stations (Kaplan, 2006). The chapter will focus on one particular system, the Global Positioning System (GPS), while a brief overview of other systems will be given at the end.

1.2. The GPS: Global Positioning System

Commissioned by the U.S. Government, the GPS is the most used and reliable GNSS at the moment of writing. The organism is under the direct control of the U.S. Department of Defense (US DOD) and for this reason it presents delicate problematic due to its reliability. For instance, the service could be suddenly switched off or partially jammed as it was until May of 2000 (OSTP, 2000). Nevertheless, it represents one of the most reliable, worldwide and robust system available (Kaplan, 2006). Due to his long active life and to the amount of material talking about this system, this will be used as example in order to understand the general purpose and functioning of a GNSS.

1.2.1. Constellation

The successful launch of the first test satellite is dated 1989 and from then on the number of satellite, or space vehicles (SVs) has risen. The nominal number of satellites at the time of conception was 24, distributed on 6 orbits with 4 satellites each. These are located on 6 relative planes that are equally spaced by 60° of the longitude of the ascending node (Ω) across the equator and with an inclination of 55° with respect to the Equatorial plane. This provides full world coverage, ensuring that 4 satellites are in sight at any time. Now 32 satellites are present. Their orbits are nearly circular and semi-synchronous (11 hrs. and 58 min.) with a distance of approximately 26.600 Km from the centre of mass of the Earth. These are Medium Earth Orbits (MEOs), chosen after a rational comparison with other altitudes orbits. The necessity of worldwide coverage and navigation accuracy has brought to this choice. In particular, on MEO air drag and pressure solar radiation forces can be neglected (Hoffman et al, 2008). Moreover, Low Earth Orbits would have brought additional problems related to the accuracy and the geometry of the system. The cost of a LEO System would have resulted in a cost differential of billions of dollars. Otherwise, the usage of Geostationary Earth Orbits (GEOs) orbit would have required heavier payload and so higher costs in order to generate a sufficiently powerful signal. Even though, this would have provided consistency on the satellite signal (Kaplan, 2006).

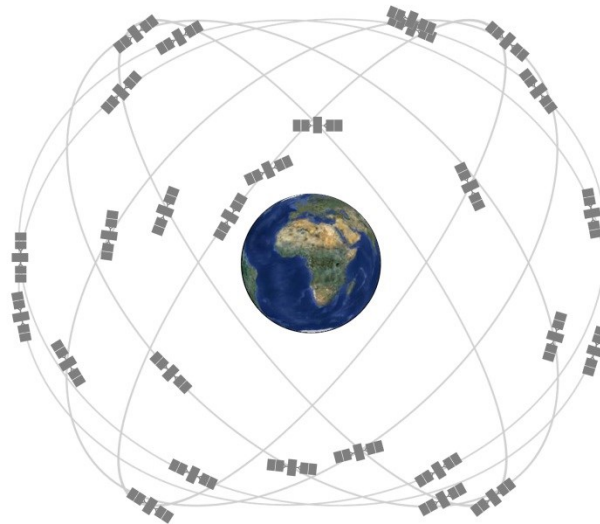


Figure 1: GPS Constellation representation (<http://www.gps.gov/multimedia/images/constellation.jpg>)

1.2.2. Features and usages of the main signal

The signal structure of the GPS is based on a Binary phase shift keying modulation (BPSK). The internal components generate a carrier signal that is later modulated simply allowing a signal of ON and OFF. In other words, the signal modulating the carrier is a series of 1 and 0. The zero does not affect the carrier, while the one triggers the modulator to switch the phase of the carrier of 180° ($\pi/2$) (Zogg, 2001). At the moment two carrier frequencies are utilized by this system for PVT, L1 at 1575.42 MHz and L2 at 1227.6 MHz. L1 supports two types of code: Coarse/Acquisition and Precision Code, while L2 only the P code. The first code is for general use, while the second is usually encrypted with higher security (Antispoofing and Selective Availability) and it is in fact mainly used for military purpose. The main differences between civil and military signals are on the clock rate and on the encoding method of the signal. The GPS signal is in fact a waveform characterized for a Pseudorandom (PRN) code that identifies each satellite. In other words the signal is a pseudo random variable sinusoid that has a proper variation for every satellite. This sequence is called pseudo random because it can be detected as informative signal only by the GPS receivers that know the various possible sequences; otherwise it can be seen as random. The difference from C/A and P is the time of repetition of this sequence: the former sequence repeats every 1 ms while the latter every once a week. For this reason the P code is much more complicated to decrypt and replicate. The portion of signal between two transitions in the PRN waveform is called *chip*, this because it does not contain an information in itself differently for what happened for a bit. The chipping rate of C/A signal is 1.023 MChip/s while for P is ten times greater, 10.23MChip/s, from here their classification as BPSK-R(1) and BPSK-R(10). As said the P signal is not

accessible by the average user thanks also to an encryption of the code itself that take the name of Y, or P(Y) code. On the other hand, the data rate is the same for both the codes: 50Hz (Kaplan, 2006). This combines with the PRN code to modulate the carrier and generate the final output as shown in Figure 2:

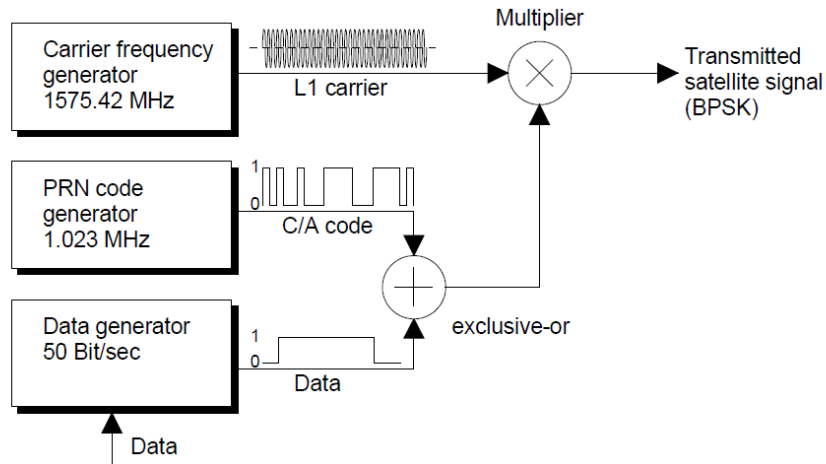


Figure 2: L1 C/A signal generation (Zogg, 2001)

The message contains useful information such as correction of time, satellite position, GPS week and more. This is used by the receiver to obtain the exact time of the satellite and to enhance the operation of calculating the position. This is due by calculating the pseudorange as presented in Equation 1. This distance is called pseudo-range because it contains an error due to the time difference between the GPS, the time kept from the satellites and the one kept by the receiver. In other words, it is not the exact range satellite-receiver, but it is a good approximation.

$$\rho_j = \|s_j - u\| + ct_u$$

Equation 1: Pseudorange equation

Where p is the pseudorange from the single satellite, s is the position of the satellite, u the receiver position, c the speed of light and t_u is the offset of the receiver from system time at time of receiving the signal.

In order to calculate the position, it is necessary to obtain the signal of 4 different satellites, so as to be able to resolve whole 4 unknowns: position(3) and time offset(1). The latter represent the time error of the GPS receiver in relation to the GPS time. Another time error is present in the satellites clock but this is detected and minimized by the Control Segment. The position definition is pretty straight forward and can be represented in Figure 2. The distance (pseudorange) from all 4 satellites (SV 1-2-3-4) is calculated and four spheres are ideally generated. They are centered on each satellite and with radius equal to the pseudorange just obtained (red arrow). These spheres create an intersection area where

the receiver position is supposed to be (yellow dot). Once more, the spheres do not usually collide in one point, and this is the origin of the error intrinsic to the GPS system.

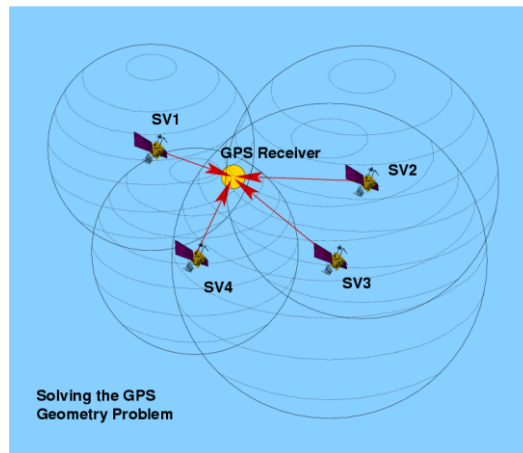


Figure 3: GPS Position acquisition scheme (<http://www.ousairpower.net>)

A secondary task of the GPS system is carried out by the NUDET, or Nuclear Detonation Detection System (Kaplan, 2006). This consists in several sensors collecting information about radiation phenomena occurring on the Earth surface. The message is then communicated on the L3 band (Carrier frequency 1381.05 MHz) to the US DOD where can be analyzed in case on alerts. L4 (Carrier frequency 1379.913 MHz) is also used for further ionospheric correction, i.e. to enhance the signal precision passing through the atmosphere (Auerbach, 2010).

1.2.3. Modernization

Two type of modernization of the GPS system are undergoing at this moment. Regarding the signal, more codes and frequencies are planned to be introduced. On L1 band another code called Civilian or L1C will be implemented, in order to give higher accuracy to the C/A already present. On L2, L2C code is already being broadcasted but only from recent times. The first launch occurred in 2005 while full operational capabilities, i.e. world coverage given by 24 operative satellites, are programmed to be obtained in 2016 (Dobberstein, 2012). Another encrypted code, the M code is also being transmitted both on L1 and L2 but not much is known, its transmission frequency is of 5.115 MChip/s.

Other enhancements made to the GPS are related to the hardware/satellites used to broadcast the signal. Most of the implementation made to the code can be broadcasted only in these new satellites models, regrouped into "blocks". After Block I and IIA, from 1997 IIR (Replenishment) were launched until 2005. Figure 4 shows an artistic conception of an IIR Block SV in orbit. For the following 4 year the IIR-M satellites were launched to support the transmission of M code. From 2010 IIF (Follow-On) block have been launched to support L5 band transmission and enhancing of accuracy. A major upgrade will take place with the launch of third generation III Block satellites. This is done with the intention of

provide almost a new generation GPS with enhanced flexibility, accuracy, anti-interference requirements and system robustness. The first launches are planned to take place in 2014 in order to have complete operability by 2030 (Kaplan, 2006; Misra, 2008).



Figure 4: Block IIR Satellite, concept (<http://www.julioizquierdo.com>)

1.3. Other Systems

As explained before, GPS is not the only positioning system operative at this moment. Europe, China, Russia and other countries have developed similar or supporting system in order to provide the same service.

1. Galileo: The European system aiming to provide a reliable source of signals that could substitute the current GPS system. This is done to make EU independent from the US DOD and provide a global service in the near future. This will be guaranteed by a constellation of 30 satellites that will transmit the signal ensuring global coverage.
2. GLONASS is the Russian counterpart with 24 satellites in orbit. It is the only active system that provides a service comparable to the GPS regarding global coverage and accuracy.
3. BeiDou is the Chinese positioning system, which concept consists of 3 satellites. Differently from the previous systems it requires two-way range measurements. This means that the actual calculation of the position is operated by a ground station once it has collected the signal from both the receiver and the satellite, and then the result is sent to the receiver. The Chinese government has planned to launch around 35 satellites in order to obtain what is called BeiDou 2 or COMPASS and provide full global coverage by 2020 (Kaplan, 2006). Even this system will provide two codes with higher and lower accuracy.

Other systems have been developed as augmentation system, i.e. to enhance the quality of the service provided in certain countries, one of this is the Japanese QZSS program (Kaplan, 2006).

2. GPS Surface Sensing

2.1. Introduction

During the years, GPS receivers have spread all over the world both for private and scientific usages. In particular, a dense network of detectors has been put in place by national and international organizations in order to acquire geographic and geodynamic data. These detectors are constituted by the combination of both antenna and receiver in order to capture and register the signal from space. Figure 5 and Figure 6 show some examples of these functioning networks:



Figure 5: EUREF Permanent Tracking Network, particular (<http://epncb.oma.be/>)

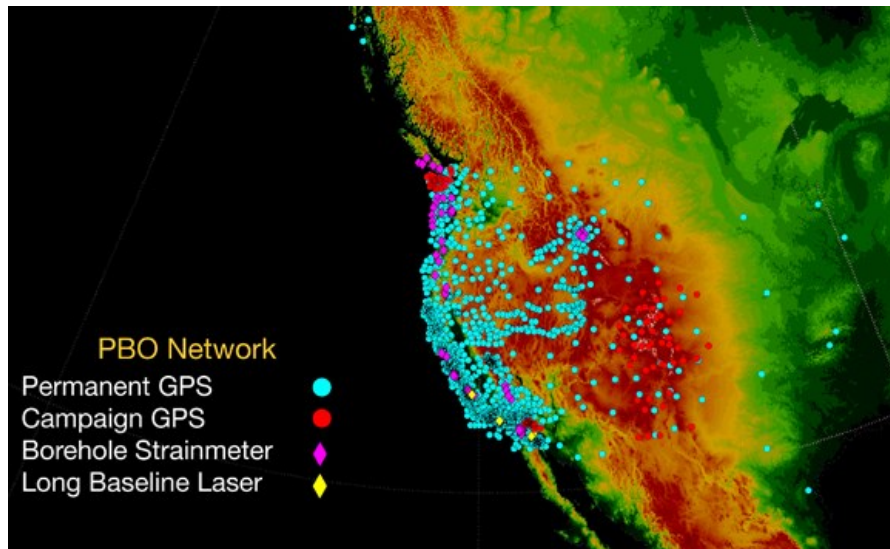


Figure 6: UNAVCO Plate Boundary Observatory Network (<http://pbo.unavco.org/>)

These systems keep track of the movements of the earth crust. In particular they observe tectonic motions and the raising of the earth surface. One of the major products of these systems is thus the set of coordinates of each station that also allow to calculate the movements described in relation to the various Terrestrial Reference Systems. Moreover, the systems perform analyses on the atmosphere behavior via remote sensing, e.g. it provide information on tropospheric delays. The peculiarity of these networks is that they collect data for the whole day, 365 days a year. This builds up a wide quantity of data that can be post processed to extrapolate the values required.

For this reasons a numerous experiments have been carried out in order to verify the possibility to use such a resource to detect sea and land movements and proprieties. This could also be used to verify existing systems already available and related to tide gauges sensors. Moreover, it will bring the possibility to operate in areas where such gauges are not installed with a cost that is practically zero. It could be also possible to validate airborne measurement and consolidate the results. GPS measurements could also been used on board of maritime and land vehicles as environment data analyzers.

2.2. Reflection theory, multipath and SNR

A common GPS receiver, such as those used in the networks depicted above are designed to primarily detect the direct signal from the satellite, trying to avoid any kind of interference and noise. One indicator of the quality of the incoming GPS signal is the so called *SNR* or Signal to Noise Ratio. The higher the SNR, the higher the quality of the signal is. Neglecting part of RF interference, such as

jamming and spoofing, one relevant source of error in GPS processing is due to the phenomenon of the so called *multipath*. This takes its name from the behavior of the signal that, instead of reaching the receiver by one unique path, it is reflected by nearby surface that multiply the paths on which the signal travels to the receiving antenna as shown in Figure 7. The signal received is thus a combination of a direct signal plus multiple copies of it shifted in time and phase, which can be modeled as in Equation 2:

$$r(t) = A_0 e^{-i\phi_0} x(t - \tau_0) e^{-i2\pi f_c \tau_0} + \sum_{n=1}^N A_n e^{-i\phi_n} x(t - \tau_n) e^{i2\pi f_n t}$$

Equation 2: Complex envelope of GPS signal affected by multipath effects

Where A_0 and A_n are the amplitudes of the direct and of the N indirect signals reaching the receiver, ϕ_0 and ϕ_n are the carrier phase of the direct and indirect signals, f_c is the carrier frequency and f_n are the frequency of the reflected signals, τ_0 and τ_n are the propagation delays from the direct path and from the N indirect paths, respectively.

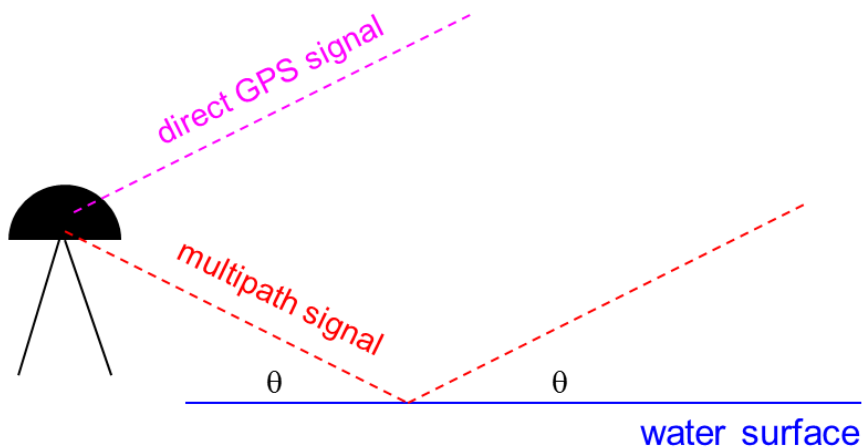


Figure 7: Multipath basic concept, θ is the elevation angle (Löfgren et al., 2012)

Even though the multipath is almost always assumed as an unwanted phenomenon, it represents a useful form of information regarding the effect of the reflecting surface on the signal. In particular there is a straight relation between the incidence angle of the GPS signal related to the surface, and the shape of the SNR:

$$SNR = A \cos(4\pi h \lambda^{-1} \sin e + \varphi)$$

Equation 3: Signal to Noise Ratio

Where A is the magnitude of the signal, h is the distance of the reflector from the antenna phase center, λ is the wavelength, e the elevation and ϕ the phase.

For the purpose of calculating the reflector height, Equation 3 was partly handled and inverted in order to be a solution for h . By looking at the formula we can neglect the phase shift of the SNR, because it is unknown and not necessary to perform the calculation. It is useful to compare the general equation of a sinusoid with the one given by the formula above:

$$\cos(2\pi ft) = \cos\left(\frac{4\pi h}{\lambda} \sin e\right)$$

Equation 4: Simulated SNR for general cosine formula with the cosine component of Equation 3 (with no phase)

In this case, the sine of elevation is the driving parameter of the function, and so it can be simplified with t , or time, that appears on the left side of the equation. By canceling the common 2π factor, the comparison brings to detect the relation between the frequency and the height.

$$f = \frac{2h}{\lambda}$$

$$h = \frac{f\lambda}{2}$$

Equation 5: Relation between height of the reflector and frequency

In this way the relation between the frequency and the reflector height is established.

As presented, the SNR depends on the height of the reflector, on the frequency of the signal and on the sine of the elevation. The sinusoidal shape is given by the phase changing of the reflected signal. The phase depends on the angle of incidence and on the distance from the reflector. Hence, the acquisition of the direct signal plus the reflected one at various angle and height can create alternative cases of constructive and destructive interference. When the signals are in phase the magnitude has a maximum while when they are in counter-phase the SNR has a minimum. Both phase and magnitude depend on the rate of reflection and refraction observed by the signal reaching the surface. The signals coming from GNSS are Circularly Polarized; hence their characterization is represented as a sum of both linear and vertical polarization. These two components can be represented as function of dielectric constant (ϵ) and the angle of incidence(θ):

$$\Gamma_H = \frac{\sin \theta - \sqrt{\epsilon - \cos^2 \theta}}{\sin \theta + \sqrt{\epsilon - \cos^2 \theta}}$$

Equation 6: Reflection Coefficient for horizontal polarization (Hannah, 2001)

$$\Gamma_V = \frac{\epsilon \sin \theta - \sqrt{\epsilon - \cos^2 \theta}}{\epsilon \sin \theta + \sqrt{\epsilon - \cos^2 \theta}}$$

Equation 7: Reflection Coefficient for vertical polarization (Hannah, 2001)

Where we can calculate ε as follows:

$$\varepsilon = \varepsilon_r - j60\lambda\sigma$$

Equation 8: Dielectric constant (Hannah, 2001)

Where ε_r is the relative permittivity, equal to 20 in the case of sea water, λ is the wavelength of the signal (0.1905 in case of the GPS system), σ is the conductivity, in the case of sea water equal to 4.

Figure 8 presents the trend of the two coefficients with the increasing of the elevation angle:

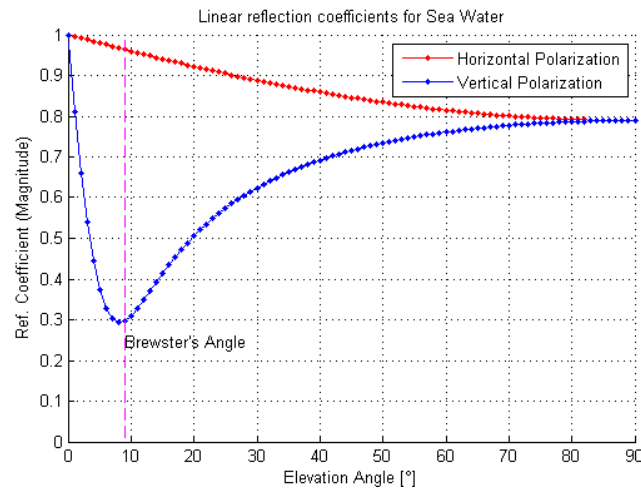


Figure 8: Behavior of Vertical and Horizontal linear reflection coefficient at varying elevation angle

It is interesting to observe the phase shift that differently applies for the two polarizations. The horizontal one is shifted by 180° while the Vertical one falls rapidly from 180° to almost 0° across the Brewster's angle. This angle represents the situation when the signal becomes mostly polarized perpendicularly to the incidence plane. Figure 9 presents the phase trend: above 20° the phase of the vertical coefficient changes slightly. This brings to an inversion of the polarization in the case of circularly polarized signals, where the contributes of the two polarization are summed together.

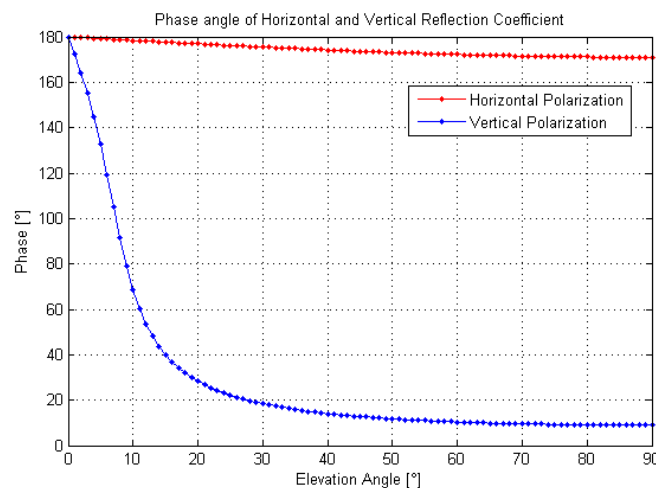


Figure 9: Phase trend for Horizontal and Vertical linear reflection coefficient (Hannah, 2001)

Hence, it is possible to calculate the coefficient for the case of circular polarized signals. In this situation, the signal reflected can be considered as constituted by two distinct signals. One of them maintains the same polarization, while the other obtains cross polarization. These two signals can be easily calculated by resolving Equation 9 and Equation 10.

$$\Gamma_O = \frac{\Gamma_H + \Gamma_V}{2}$$

Equation 9: Original polarization coefficient (Co-Polarized) (Hannah, 2001)

$$\Gamma_C = \frac{\Gamma_H - \Gamma_V}{2}$$

Equation 10: Opposite polarization coefficient (Cross-Polarized) (Hannah, 2001)

Using the formula above it is possible to depict the trend of these coefficients, as shown in Figure 10:

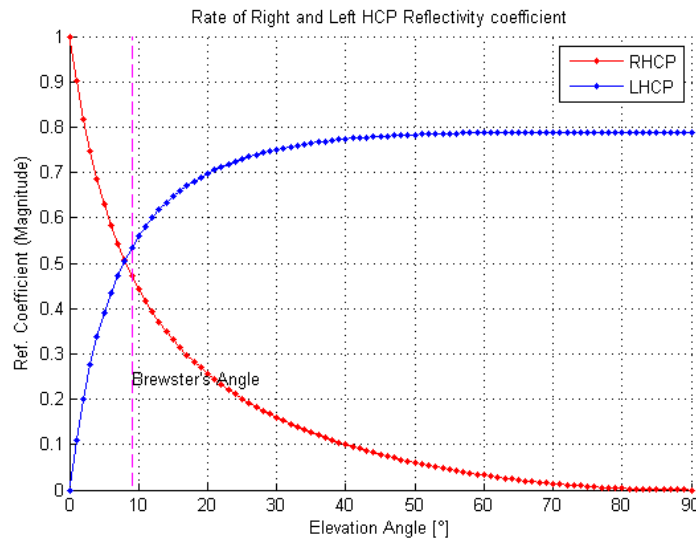


Figure 10: Original (R) and Opposite (L) polarization reflectivity coefficients (Hannah, 2001)

As can be seen in Figure 10, when only one RHCP antenna is used, the disturbance coming from the reflected signal are more intense at low elevation angle. At angle above 40° the coefficient fall below 10% of the power of the direct signal. Hence, the SNR fluctuation is not so evident and loses of interest for the case in exam. The coefficient in the case of single circularly polarized antenna can be also rewritten as *effective circularly polarized coefficient*. In this case the rejection of the opposite polarization by the antenna is taken in count on the formulation of the coefficient. Equation 11 shows the definition of the coefficient while Figure 11 presents its behavior for a rejection ratios K of 10 dB, assuming RHCP antenna and signal.

$$\Gamma_R = \left(\rho_o + 10^{-\frac{K}{20}} \rho_c \right)$$

Equation 11: Effective RHCP reflection coefficient (Hannah, 2001)

Where ρ_o is the co-polarization circular reflection coefficient magnitude (RHCP in this case), ρ_c is the cross-polarized circular reflection coefficient magnitude (LHCP in this case).

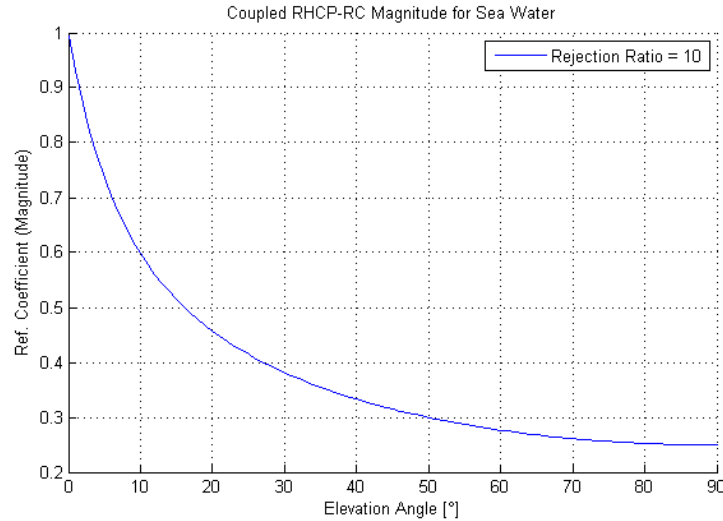


Figure 11: Effective CP reflection coefficient (Hannah, 2001)

Moreover, the effect of surface roughness could be added by means of the *Rough surface reduction factor*. The multiplication of this factor with Equation 11 brings a correction that takes count of the roughness. Assuming a roughness of 10 centimeters the calculation continues as follows. After the Rayleigh criterion in Equation 12 is verified the phase difference presented Equation 13 in can be calculated. Otherwise the roughness effects can be considered as negligible.

$$\Delta H \geq \frac{\lambda}{8 \sin \theta} \text{ valid until } \theta \geq 14^\circ \text{ for GPS}$$

Equation 12: Rayleigh Criterion for the roughness of a surface (Hannah, 2001)

$$\Delta\varphi_H = \frac{4\pi\Delta H}{\lambda} \sin \theta$$

Equation 13: Phase difference between two rays being reflected at location with a difference in height equal to ΔH (Hannah, 2001)

The roughness factor can be calculated using Equation 14:

$$\rho_s = e^{(-\frac{1}{2}\Delta\varphi_H^2)} I_0(\frac{1}{2}\Delta\varphi_H^2)$$

Equation 14: Rough surface reduction factor (Hannah, 2001)

Where I_0 is the modified Bessel function of zero order.

Using the previous formula and parameters it is possible to depict the behavior of this factor as presented in Figure 12.

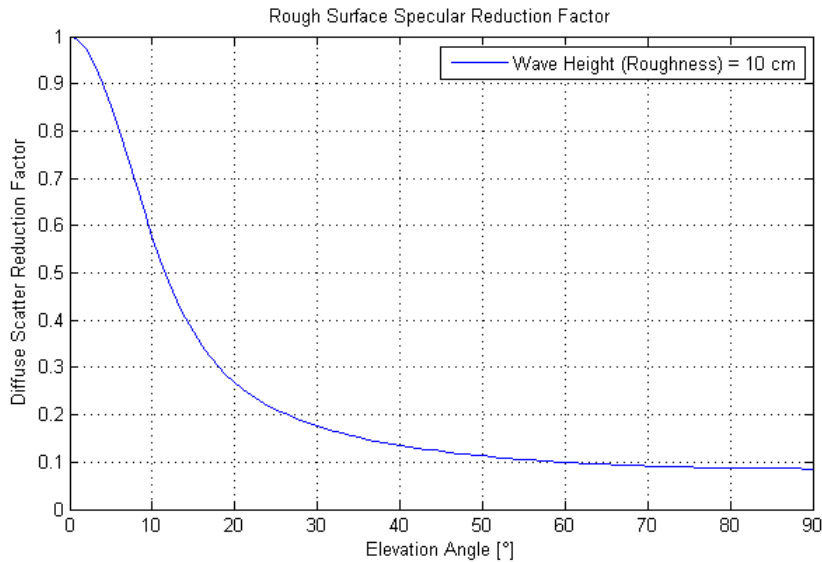


Figure 12: Rough surface specular reduction factor (Hannah, 2001)

As shown, the factor enhances the reduction of the reflected power acquired by the antenna at high elevation angles. As can be easily observed, in order to detect relevant fluctuation in the SNR it is indicated to use a medium-low elevation angle (<50°) .

For circularly polarized signals the phase variation at the moment of reflection is of 180° (Hannah, 2001). The fluctuation in the SNR is due to the variation on the length of the path traveled by the reflected signal. The area over the reflection occurs is generally individuated by the first Fresnel zone. This is in fact usually intended as the main contributor on the magnitude of the reflected signal. In the case of signal reflection the Fresnel zones can be identified as the intersection between the reflecting surface with a series of ellipsoid with the focuses on the satellite and on the projection of the antenna parallel to the direct signal, as shown in Figure 13. All the ellipsoids are generated by using the relation depicted in Equation 15:

$$AM + MB = AB + n \frac{\lambda}{2} \quad n \in N$$

Equation 15: Fresnel ellipsoid equation (Hannah, 2001)

Where A and B are the two focuses of the ellipse and M is a point on the perimeter of the intersection area.

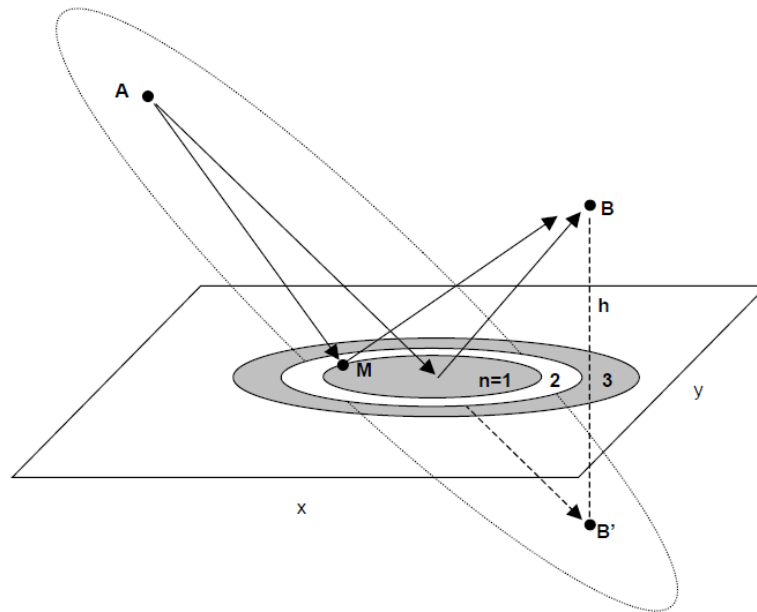


Figure 13: Fresnel Zone scheme in case of surface reflection (Hannah, 2001)

It is then possible to define the main dimension for each Fresnel zone. In the case of the first Fresnel zone ($n=1$) the radius can be calculated by using Equation 16, while the semi-major axis using Equation 17.

$$R_F = \sqrt{\lambda \frac{h}{\sin \theta}}$$

Equation 16: Radius of the first Fresnel zone (Hannah, 2001)

$$L_{SMA} = \frac{R_F}{\sin \theta}$$

Equation 17: Semi-major axis of the first Fresnel zone (Hannah, 2001)

As shown, the radius is dependent on the height of the antenna with respect to the reflecting surface. Figure 14 shows a set of possible radii at various heights from 1.5 to 2.5 m. Figure 15 depicts the relative semi-major axis. As from the formula above, the area of major reflection increases with the increasing of the height. Hence, it has to be supposed that by rising the antenna it should be possible to enhance the magnitude of the reflected signal. Vice versa, by increasing the elevation angle the signal intensity diminishes. Once more then, at higher elevation the reflected signal tends to lose its effect on the SNR.

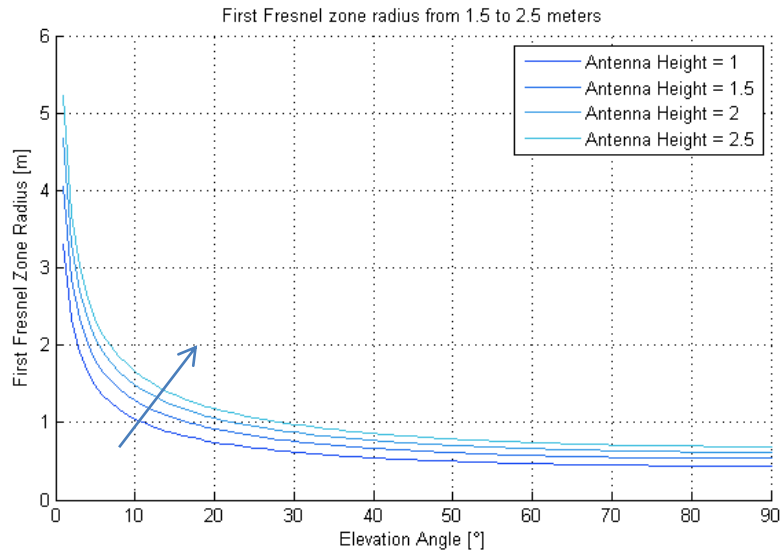


Figure 14: Radius of the first Fresnel zone at increasing antenna heights

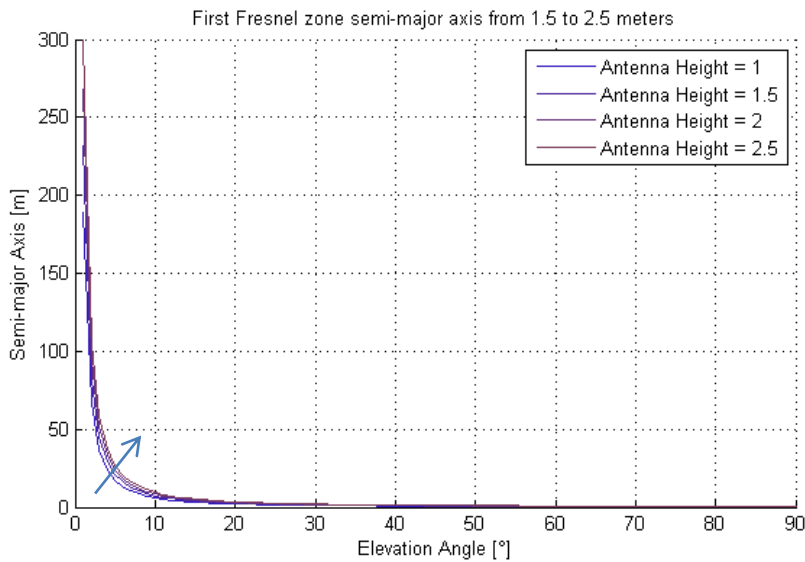


Figure 15: Semi-major axes of the first Fresnel zone at increasing antenna heights

Another factor that affects the shape of the SNR is the antenna gain: this tends to enhance the signal coming from a certain direction that is usually near the zenith (90° Elevation from horizon). On the contrary, higher interaction between the direct and reflected signal can be seen at lower elevation. This is due to the gain pattern of the antennas and to the higher reflectivity of the surface reached by the GPS wave at low incidence angle. At low elevations in fact, the gains reduces usually its value. Moreover, both signals tend to come from a common direction, remaining inside a small angle interval. For this reason the gain applies its action on both of them almost equally. The importance of the antenna gain can be seen in Equation 18, where the power received by the antenna is linearly dependent from its gain:

$$C = \frac{P_T G_T G_R}{L} \left(\frac{\lambda}{4\pi R} \right)^2 \quad [\text{watts}]$$

Equation 18: Received Power (Kaplan, 2006)

Where C is the power of the carrier wave received by the antenna, P_t the transmitted power, G_t and G_r are the gain of the transmitting and receiving antenna respectively, L is the propagation loss, while R is the distance between receiver and transmitter.

The gain is dependent on the type of the antenna. It has been observed that choke ring antennas tend to well behave against multipath, reducing its interference with the main signal (Kalman, 2006).

Another effect of the multipath is related to an error in pseudorange. If the time delay of the reflected signal is less than a chip period, the correlation functions adjusting the received signal(s) inside the receiver bring to a miscalculation of the distance within the order of meters. In Equation 18 it is possible to see also another kind of interference related to pseudorange errors, due to the traveling medium of the signal. Ionosphere (Ionospheric Scintillation) and troposphere tend to deviate it, reducing the power and adding a delay on the GPS wave coming from space (Kalman, 2006; Hofmann-Wellenhof, 2008). Even though this effect cannot be ignored while calculating the position of the receiver, while handling the SNR it has not such an impact. In this case in fact both direct and reflect signals have the same disturbance and so their relation is not modified. The power of the signal reaching the receiver is highly reduced but the signal is still well detectable in many cases.

2.3. Lomb Spargle Periodogram

As stated in 2.2, there is a link between the frequency induced by the multipath to the SNR and the sea level. What is acquired from the simulator is a vector containing the value of the SNR equally spaced with regard to the elevation. As shown in Equation 3, the variation of the height has to be referred as a function of the sine of elevation. This brings to a first complication for what the handling is concerned. The height calculation requires a method to acquire the main frequency of the arc, having non-equally spaced samples. Thus, in this case it is not possible to use the well-known FFT implemented in MATLAB. Another tool had to be used: the Lomb-Scargle Periodogram. This is a Least-squares spectral analysis method that is able to approximate a discrete set of data, even not equally spaced, into a weighted sum of sinusoids. The technique tends to fit the discrete data set with sinusoids at progressively determined frequencies, choosing those that minimize the residual after least squares fitting. The method is based on a simplified case of the Vaníček method (Craymer, 1998): the functions are chosen as sine and cosine with equally spaced samples. Thanks to Lomb first, and Scargle later, this *least-squares spectral analysis* (LSSA) was shown to be applicable also in cases where the data were not equally spaced. Specifically, an

original method regarding LSSA was presented in order to acquire the spectrum of a set of data not evenly spaced as sum of weighted sinusoidal functions. Equation 19 presents in simplicity the starting point, where a set of data D is represented as multiplication of weight function in matrix w and the sinusoidal ones in S .

$$D \approx Sw$$

Equation 19: LSSA approximation of the data set

Once chosen the sinusoids, the only unknowns that remain are contained in w , calculable by inverting the system:

$$w = (S^T S)^{-1} S^T D$$

Equation 20: Weight functions formula

If in this case the functions chosen are sinusoids and the samples are equally spaced, the first product in Equation 20 is the identity matrix, so it can be taken away from the equation. In this way the formula becomes more simple and faster. Lomb and Scargle have shown that this last simplification can remain valid also with not evenly sampled data, in particular by adding the parameter τ presented in this formula:

$$\tan 2\omega\tau = \frac{\sum_j \sin 2\omega t_j}{\sum_j \cos 2\omega t_j}$$

This represents the time delay after which the pair of sinusoids chosen is mutually orthogonal at sample time t_j . The main output value of the analysis is the L-S Periodogram, represented with respect to the frequency in Equation 21:

$$P_x(\omega) = \frac{1}{2} \left(\frac{[\sum_j X_j \cos 2\omega(t_j - \tau)]^2}{\sum_j \cos^2 2\omega(t_j - \tau)} + \frac{[\sum_j X_j \sin 2\omega(t_j - \tau)]^2}{\sum_j \sin^2 2\omega(t_j - \tau)} \right)$$

Equation 21: Amplitude of the LS Periodogram as a function of the frequency

This is reported to have the same statistical distribution as the periodogram in the case of equally spaced sample.

2.4. Previous Experiments

Various experimental work has been done in order to assess the reliability of using GNSS signal to retrieve surface position in relation to the antenna receiver. One of the first experiment used reflected signals from the water surface to calculate the distance. This was called *Passive Reflectometry and*

Interferometric System (PARIS) which was using existing satellite systems for remote sensing. This usage was particularly convenient because it made use of preexisting, widespread, reliable GNSS signals. It allowed to use the signal generated by GNSS not to calculate the position of the receiver, but for ocean altimetry and sea state analysis. The basic functioning consisted on comparing the direct signal with the reflected signal when received from a satellite located in a lower orbit with respect to the transmitting satellite. It was called passive because there was not a direct communication between transmitter and receiver, but the latter was constantly and independently acquiring information from the signals. As said, in this case both transmitter and receiver were located in space. Differently, the evolution of these concepts brought also to measurements regarding sea level to be performed by airborne and terrestrial receivers.

Lowe et al. (2002b) achieved a 5 cm precision calculating the altimetry of the ocean from a flying aircraft. In this case, direct range measurements were performed in order to calculate the delay of the reflected signal and from this calculate the distance from the aircraft. Another work presented by Semmling et al. (2011) shows the detection of ocean tides using L1 and L2 band GPS signal. In this experiment a residual height mean (mean of $H_{surface}-H_{reference}$) of 9.7 and 22.9 cm for the two bands respectively has been retrieved. Tropospheric error is pointed out to be relevant in these measurements. Löfgren et al. (2010 and 2011), Soulat et al. (2004), Dunne et al.(2005) and others have performed studies on reflected GPS signal in coastal environments. All these works found their processing the relation between the direct and reflected signal. This was done mainly by retrieving the coherence time via statistical analysis. Dunne et al.(2005) presented also a brief study on sea state and significant wave height (SWH), which indicates the grade of motility of the sea. By mean of autocorrelation function it was shown to be possible to calculate the mean value of this variation (18.1 cm). Löfgren et al. (2010 and 2011) presented various configurations in order to calculate the effect of reflected signals. In particular the usage of single and multiple antennas was presented. While in many work a single Right Hand Circularly Polarized (RHCP) antenna is used, double antennas, RHCP and LHCP proved to be effective and accurate in the height calculation. This is made because the power received by LHCP when the signal is reflected at high elevation angles appears to be higher, as shown in Figure 10. In both these cases the antenna main axes is pointing orthogonal with respect to the ground/surface. This is made to maximize the signal coming from the satellite directly in case of antenna looking upward. Vice versa, the signal reflected is coming from the surface and it is partially Left Handed Circularly Polarized. This should bring the down looking antenna to increase the magnitude of the acquired signal. Treuhaft et al. (2001) proved to retrieve a 2 cm accuracy altimetry. This was also done, once more, by calculating the delay of the reflected signal using correlation processes. In this case the water surface was not sea but a lake. This helps the height calculation due to the stability of the

surface that was not so affected by tidal variation and wind.

It is worth to remember that the established working network provides usually upward looking antenna. This should tend to partially reduce the multipath signal that is intended as deleterious to the analysis.

A work by Larson et al. (2010) presents useful notion regarding the influence of soil moisture on signal reflection. In this case the interaction of direct and reflected signals was observed by analyzing the SNR values. The variation of this parameter is shown to be related on the modification of the soil characteristics. The frequency of the interference of the reflected signal on the direct one was used to calculate the depth fo the reflective surface. If data were collected not too close to any event of rain, they showed a direct connection between the soil moisture content (SMC) and the variation of the distance of the reflector. This is due to the propriety of the signal to penetrate more in dry soil than in wet soil. A partial limitation is settled by an SMC of $0.1 \text{ cm}^3/\text{cm}^3$ from which this relationship commences to fade. Larson et al. (2009 and 2012a) also performed experiments on snow sensing utilizing the EarthScope Plate Boundary Observatory, a wide US GPS network primarily used for geodynamic studies. In this case snow depth was analyzed. It has been shown that for terrain slope less than 8° the height retrieval error remain below 5 cm. For this experiment L2C code on L2 band was used and it has shown to generate accurate results. Larson et al. (2012b) showed the relation between the height of the reflector and the SNR behaviour for coastal environments. In this case one RHCP antenna looking upward was used, differently from the previous experiment. The analyis was performed in two different locations: at Onsala in Sweden and at Friday Harbour in Colorado, USA. The results showed slight discrepancy on the accuracy of the measurements. The RMS between the GPS measurements and synthetic tide gauges for the former experiment was of 4.8 cm. Differently at Friday Harbour the RMS obtained was around 10 cm.

The experiment carried out by Larson et al. (2012b) utilizes one single antenna to acquire the signal, halving the price in comparison to previous experiment. It would be now interesting to tilt the antenna in order for the dish to directly face the horizon. This should enhance the magnitude of the signal reflected when acquired by the antenna. In this manner, the lack of the second antenna would be partially compensated and the gain of the antenna would operate as beneficial factor not only for the direct signal, but also for the reflected one. Having this in mind, this thesis has also the purpose to calculate sea level variations for an antenna tilted by 90° , i.e. pointing the horizon.

3. Antennas

3.1. Introduction

A multitude of GNSS antennas have been designed and constructed in the past years with the purpose of receiving the GNSS signals. Their primary task is to acquire GNSS signals and try to enhance their power. For this reason, these antennas have much of their gain concentrated on high elevation, usually higher than $10\text{-}15^\circ$ above the horizon (Kaplan, 2006). The graphs mapping this gain are called antenna radiation pattern. Furthermore, they are usually Right Handed Circularly Polarized (RHCP) antennas, even though they acquire part of Left Handed Circular Polarized (LHCP) energy anyway. It has to be taken in count the fact that when an RHCP signal is being reflected by a surface it can change its polarization (or part of it) to LHCP. This occurs especially at high elevations, where the angle of incidence of the wave on the surface is relatively acute, and it is related on the reflective proprieties of the surface. This behavior is directly related to the phenomenon of the multipath, i.e. multiple reflections of the direct signal due to objects present along the path of the wave. An instrument to quantify the quality of an antenna in regards to multipath effects is the MCR, or *multipath ratio*. This consists in the ratio between the RHCP gain of the antenna at the direct signal incident angle with respect to the sum of RHCP and LHCP gain components at the multipath signal incident angle (Kaplan, 2006).

The position where the antenna acquire the GNSS signals is called APC, or *antenna phase center*. This is also specified in electrical antenna phase center, not to be confused with the physical one. The former is in fact the actual location where the antenna captures the signal. It can move by usually not more

than 10 mm (vertical component) depending on the direction of the incoming signal, i.e. azimuth and elevation, and on the frequency. The latter is a fixed physical point that is commonly defined by the location of the chipset within the antenna. Both these points cannot be defined directly. For this reason the APC is usually defined with an offset from the ARP or *antenna reference point*, usually located at the base of the antenna, along its axis of rotation. Tabulated offsets can be found at <http://www.ngs.noaa.gov/ANTCAL/>.

Antennas differentiate themselves also for the type of band and signals they can acquire. As said before, the most utilized GNSS signals come from GPS and GLONASS systems on L1 (G1 for GLONASS) and L2 (G2 for GLONASS) band. It has to be pointed out that these antennas can usually capture a bandwidth of 1-2% of the signal center frequency (Kaplan, 2006), the carrier frequency. In any case, the signal received is very weak, around -160 dB (Kaplan, 2006), so the antenna requires an accurate system to reduce the noise and the interference. This is usually integrated in the receiver, due to the complexity of the design. Nevertheless, a low noise amplifier is usually put between antenna (active antenna) and receiver to roughly “clean” the signal and enhance the GNSS signal with respect to the noise. In other words, it already amplifies the signal without adding as little noise possible before this is manipulated by the receiver. Lastly, antennas can be covered by a radome in order to be protected by adverse weather conditions. At the same time the radome delays the direct signal, it adds minimal losses (Manz, 2001) and it marginally modifies the APC (Braun, 2007).

Two antennas were used to perform height measurements during this test campaign. Both of them belong to the Leica family, a known company on the GNSS sector. In order to understand their characteristics a short overview is presented below. The antenna gain patterns will be shown, along with basic schematics on their geometry, principal reference points and APC fluctuation.

3.2. LEICA AT 504GG

The first antenna is a Leica AT 504GG. It is a choke ring antenna with no radome assembled by Leica. It can both acquire L1 and L2 band, on both GPS and GLONASS systems. The main geometrical characteristics can be found in Table 1.

Table 1: Leica AT 504 GG main dimensions

Parameter	Height	Diameter	Weight
Dimension	14.0 [cm]	37.8 [cm]	4.3 [Kg]

The sketch in Figure 16 depicts the main geometry of this antenna with its points of interest according to the International GNSS Service (IGS) (<http://igscb.jpl.nasa.gov/igscb/station/general/antenna.gra>):

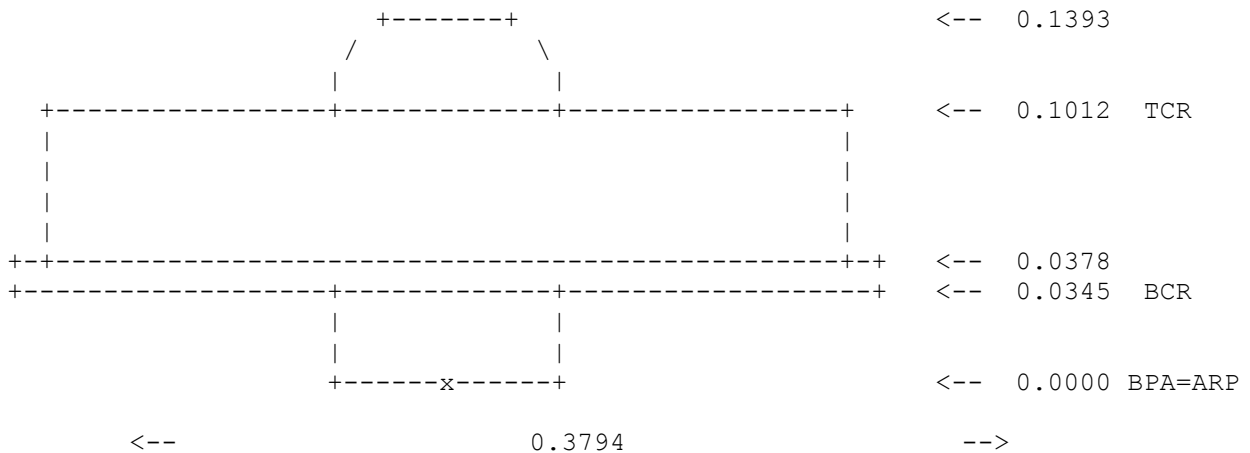


Figure 16: Leica AT504 GG point of interest

Table 2: IGS Abbreviations

Abbreviations	
ARP	antenna reference point
BCR	bottom of chokering
BPA	bottom of preamplifier
TCR	top of chokering

In Figure 17 the same antenna is represented in a draw depicting its side view. As it can be seen, the distances are measured by the Naval Geodetic Survey (NGS) with respect to a base reference surface.

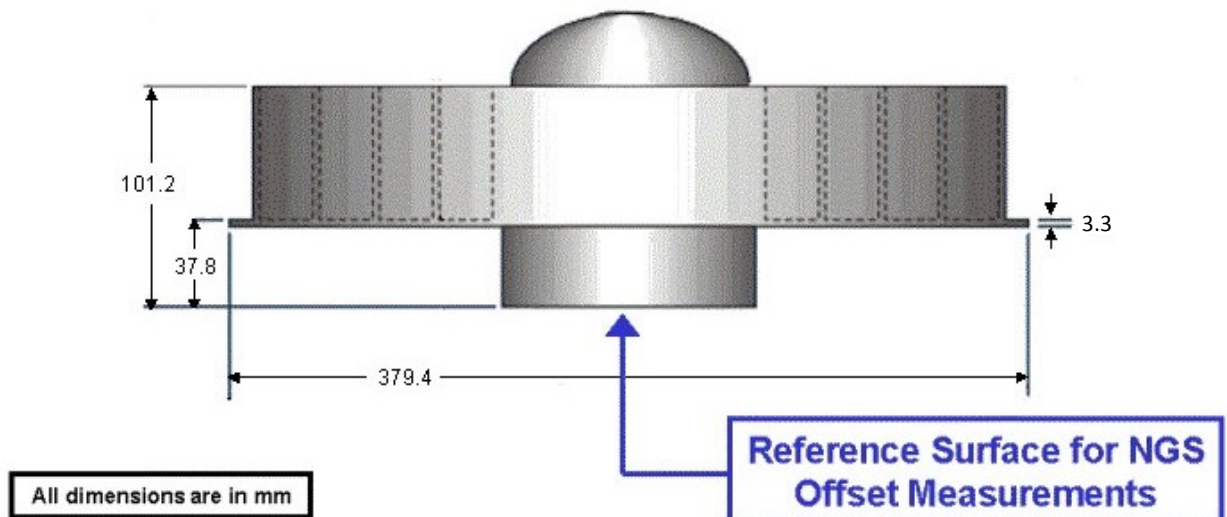


Figure 17: Leica AT 504 GG side view (NOAA <http://www.ngs.noaa.gov/ANTCAL/Antennas.jsp?manu=Leica>)

The antenna gain pattern is depicted in Figure 18 (Bedford et al. 2009): the peak is clearly visible at higher elevations for L1 and L2 RHCP. The graph has been normalized in order to easily depict the changing in gain due to variations in satellite elevation. The peak of the gain is 5.5 dB at zenith and it falls rapidly when the elevation decreases. At the horizon the radiation pattern is around -11.1 dB as

can be calculated from the graph (Bedford, 2009). At plus and minus 170° the gain drops drastically below 30 dB. On the other hand, LHCP signals are almost equally enhanced throughout all the elevations at an averaged normalized gain of -25dB. As can be seen by the absence of an azimuth reference, the antenna is multidirectional, so the gain is applied to every satellite in the same way.

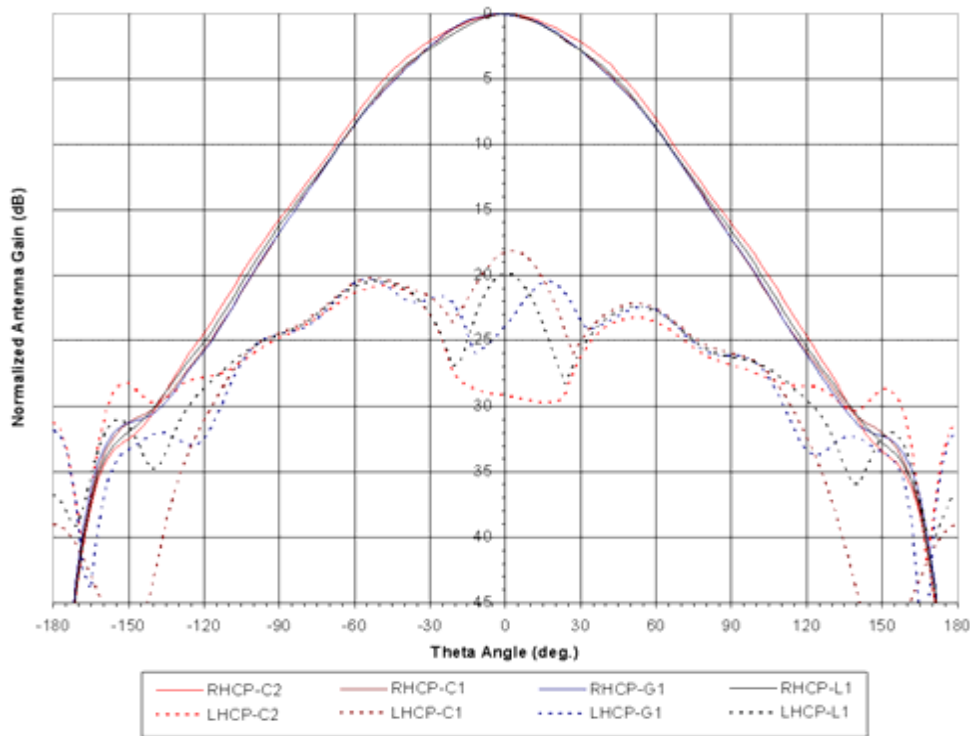


Figure 18: LEIAT 504GG Normalized Gain Pattern (Bedford, 2009)

Leica AT 504 GG presents remarkable performances regarding APC definition with a type-mean phase centre offsets below 1mm. This means that it is possible to determine the position of the antenna phase center allowing a narrow uncertainty in the measurement. This ensures high quality in position estimation and also in distance measurements while working with multipath effects. IGS has carried out a test campaign in order to analyze various antennas typically used in GNSS signal measurements. Thanks to the data acquired it was possible to determine the eccentricity of the mean APC relative to the ARP. In other words, it was possible to determine the mean position of the phase center, i.e. the location where the signal is actually acquired, with respect to a reference point fixed on the antenna.

Table 3: Mean APC offset relative to the ARP [mm]

Direction	North [mm]	East [mm]	Up [mm]
Offset	0.62	1.16	89.56

In addition, at every elevation and azimuth angle the APC varies slightly as can be seen in Figure 19 and Figure 20. These graphs present the direct and inverse variation of the APC from the mean value

regarding the direction of the L1 signal. The negative values have been used to better depict the shape of the pointing vector and allow an easy understanding. Figure 19 represents it with respect to elevation and azimuth while Figure 20 shows this pattern with respect to the antenna. When the antenna receive signals from other bands, e.g. L2 and GLONASS signals, the phase pattern for this signals will differ according to the frequency of the incoming wave. A complete set of data for GPS AND GNSS L1 and L2 phase patten can be found at http://www.ngs.noaa.gov/ANTCAL/LoadFile?file=LEIAT504GG_NONE.atx.

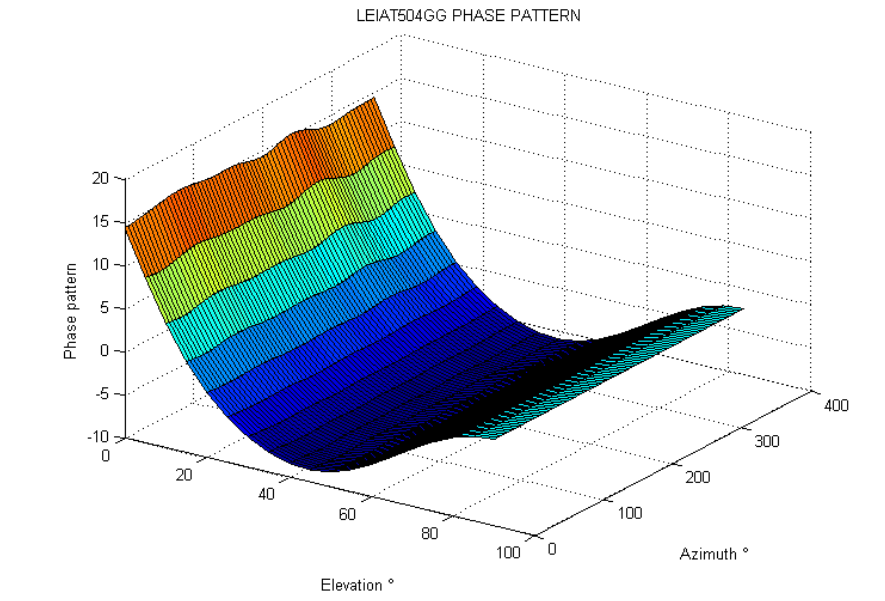


Figure 19: Phase Pattern for Leica AT 504 GG with respect to azimuth and elevation

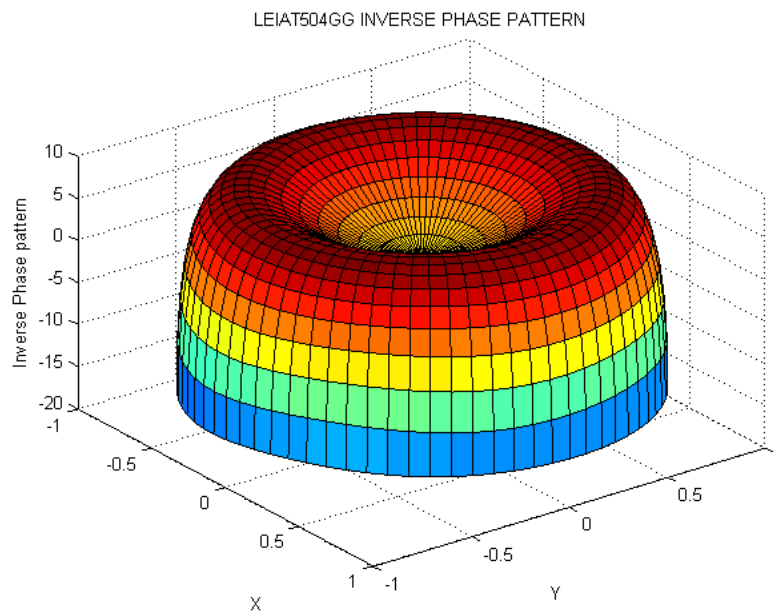


Figure 20: Phase Pattern for Leica AT 504 GG with respect to the antenna

3.3. LEICA AX 1202GG

The other two antennas used during the test campaign were both the same model: Leica AX 1202GG or, according to the IGS code, Leiax1202GG (ftp://igscb.jpl.nasa.gov/pub/station/general/rcvr_ant.tab). This antenna supports both GPS and GLONASS on both L1 and L2 as the other antenna model. Its bandwidth is almost 40 MHz in both bands. The useful features of this antenna are the light weight of 0.5 kg, the flexibility and high performance that bring it to be comparable to the choke ring. In particular, the reduced weight and dimensions make it easier to position it on various stands and with various tilting angles. The high gain pattern, the stability of the APC and the behavior against multipath interferences are comparable to its competitors. Table 4 reports the antenna main dimensions, decidedly reduced compared to the values in Table 1.

Table 4: Leica AX 1202 GG main dimensions

Parameter	Height	Diameter	Weight
Dimension	6.2 [cm]	175 [cm]	0.5 [Kg]

From the IGS sketch in Figure 21 and NOAA side draw in Figure 22 it is possible to identify the ARP and the dimensions presented above, as well as a basic schematic of its design.

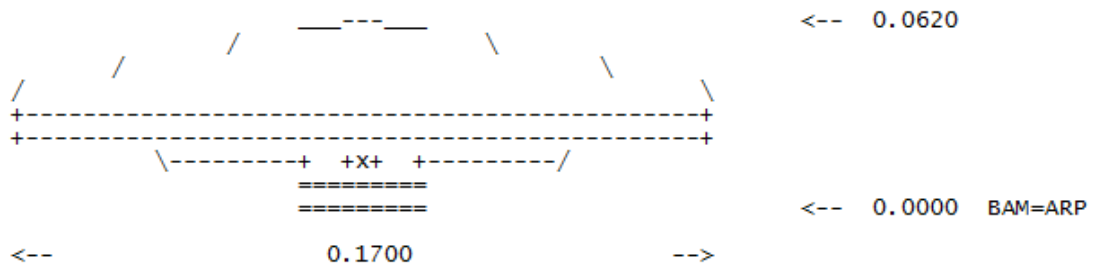


Figure 21: Leica AX 1202 GG Nasa Sketch (<http://igscb.jpl.nasa.gov/igscb/station/general/antenna.gra>)

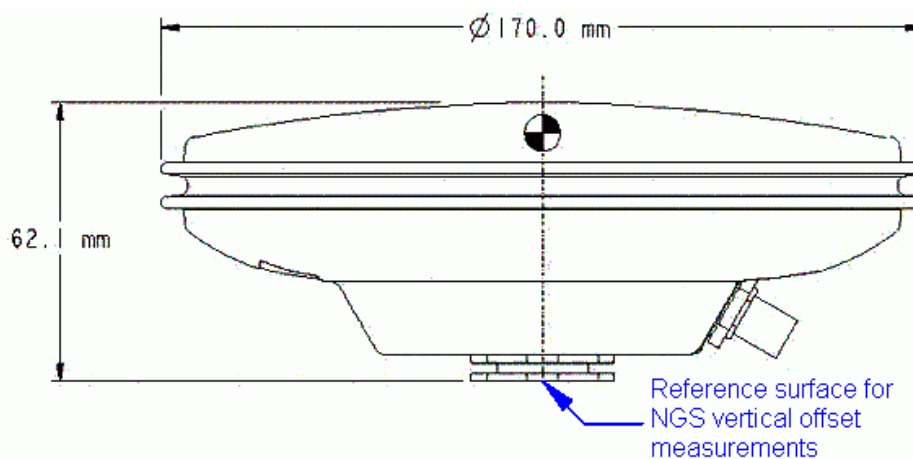


Figure 22: Leica AX 1202 GG side view (NOAA <http://www.ngs.noaa.gov/ANTCAL/Antennas.jsp?manu=Leica>)

The normalized gain pattern of the antenna for L1 band (red GPS, blues GLONASS) is shown in Figure 23, for L2 it is similar. Once again the graphic has been normalized to easily understand the trend with respect to variations in elevation. In this graph the horizon is set at 0° and the zenith at 90° differently from the previous pattern presented above. The peak is still at zenith, with a value of 5dB while at the horizon, the gain experiences a roll-off of 13 dB (Novatel, 2011). Once again it is possible to see that the antenna is RHCP due to its poor gain on LHCP signals. Nevertheless, for low elevation below the horizon the LHCP gain shows a minimal peak.

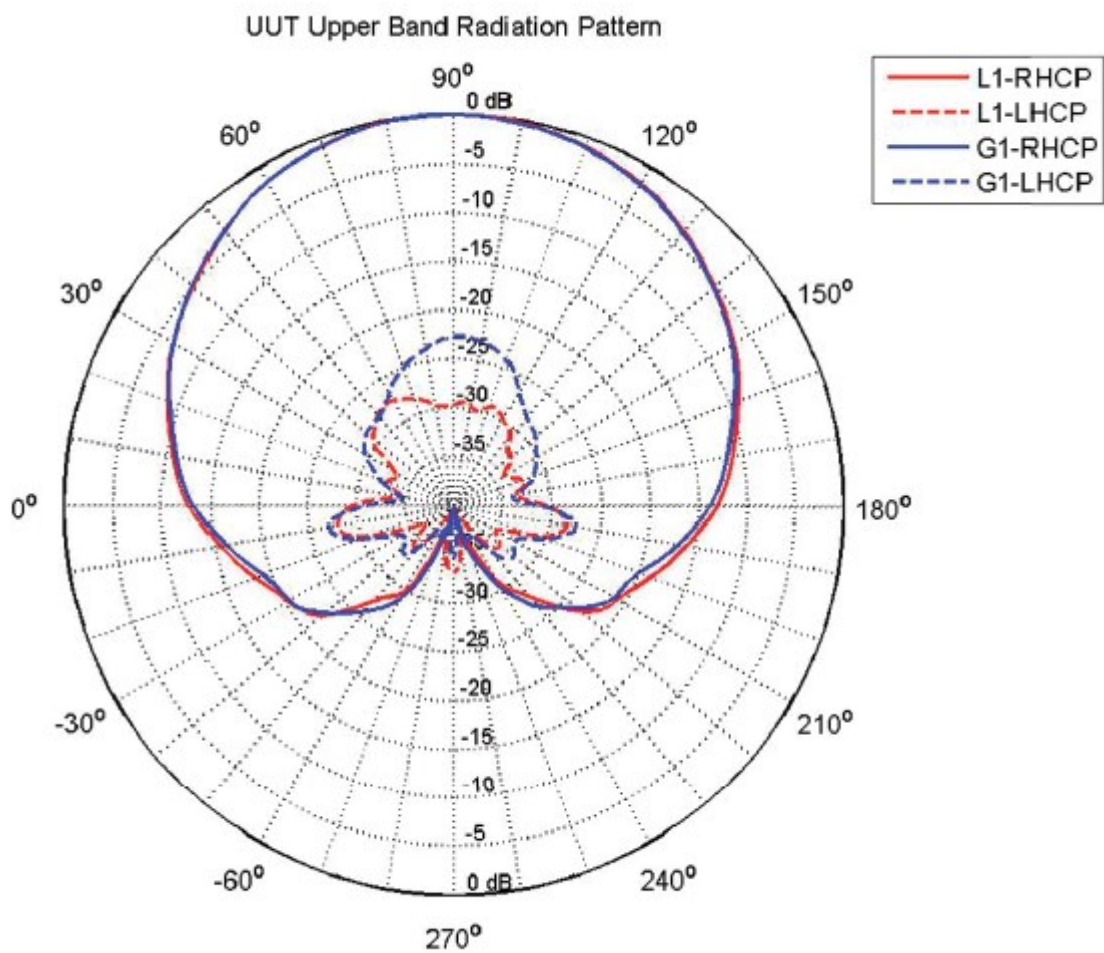


Figure 23: Leica AX1202 GG Normalized Gain Pattern (Novatel, 2011)

Table 5 presents the mean APC offset related to the ARP, in this case located at the base of the antenna. Once more the major offset of 63.42 mm is represented by the up component.

Table 5: Mean APC offset relative to the ARP [mm]

Direction	North [mm]	East [mm]	Up [mm]
Offset	1.64	-0.52	63.42

Figure 24 and Figure 25 represent the direct and inverse phase pattern with respect to elevation and azimuth in the former and to the antenna in the latter (http://www.ngs.noaa.gov/ANTCAL/LoadFile?file=LEIAX1202GG_NONE.atx). The amplitude of the variation appears to be less wide but more irregular if compared to the one of Leiat504GG. This could be due to the improved performances of Leiax1202GG that tends to stabilize the APC and to enhance the quality of the position measurement.

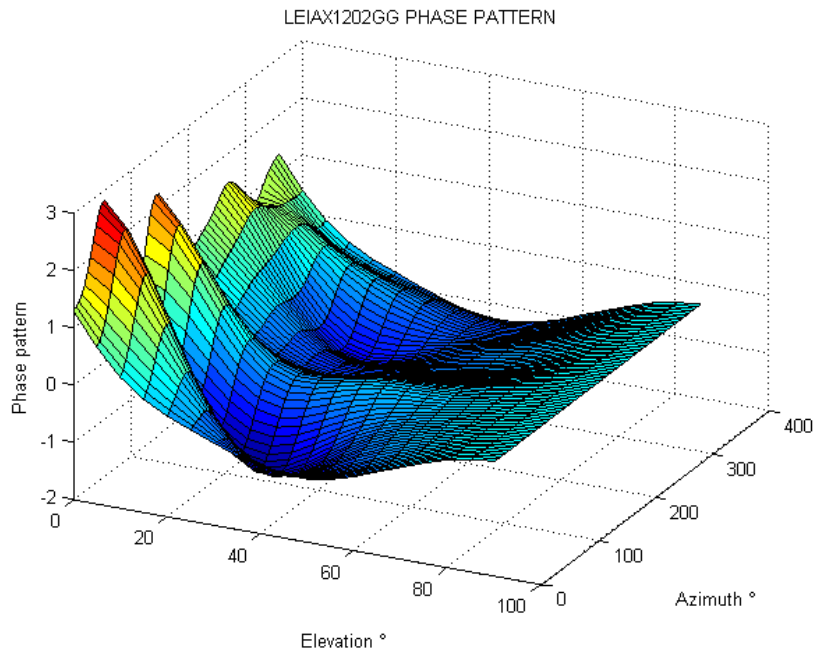


Figure 24: Phase Pattern for Leica AX 1202 GG with respect to azimuth and elevation

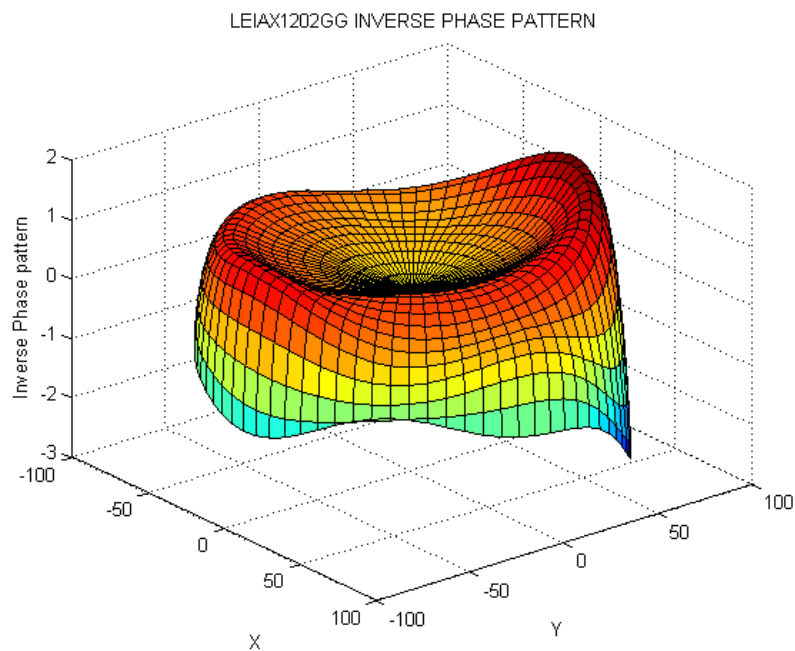


Figure 25: Inverse Phase Pattern for Leica AX 1202 GG with respect to the antenna

4. The Simulator

4.1. Introduction

A test campaign was carried out to ensure the effective feasibility of retrieving useful height values from SNR data of three antenna configurations. This concerned the use of two types of antennas as follows:

- Leica AT 504 GG facing upward named SEA1
- Leica AX 1202 GG facing upward named SEA2
- Leica AX 1202 GG facing the horizon named SEA 3

This was done in order to determine the different performances of these three configurations and in particular to observe the effect of tilting the antenna on the analysis results. The aim is in fact to define the behavior of the SNR wave for these setups and thus to determine the way to obtain more precise height measurements. Along with this experiment, the possible use of an SNR simulator in MATLAB environment was tested. The SNR simulator was developed by Nievinski F.G. at University of Colorado at Boulder in order to rapidly simulate the ideal SNR signal received by a GPS. A common array of settings that resembles the actual setups is presented in Table 6.

Table 6: General Simulation Parameters

Parameter	Value [unit]	Description
Frequency - Band	L1 – 1575.42 [MHz]	
Code	C/A	Coarse Acquisition, 1023 chips, repetition period: 1ms, message freq.: 50Hz
Polarization	RHCP	Related to the antenna Gain Pattern
Model SEA1	Leica AT 504 GG	Leiat504GG, GPS and GLONASS, L1 and L2, G1 and G2, chokering
Model SEA 2&3	Leica AX 1202 GG	Leiax1202GG, GPS and GLONASS, L1 and L2, G1 and G2
Radome	-none-	No shelter against weather precipitations
Bandwidth Noise	1 Hz	Common factor to easily compare the antennas
SEA 1 tilt angle	0 [°]	Facing Upward
SEA 2 tilt angle	0 [°]	Facing Upward
SEA 3 tilt angle	90 [°]	Facing the Horizon
Top Material	Air	
Bottom Material	Sea Water	
T Bottom Material	0 [°C]	Chosen as a simplified average of the temperature of the water at the test location

The main output of this software is the generation of SNR data and correlated graph on a GNSS signal affected by multipath. The purpose, as stated on the main script is to act as “A GPS multipath simulator for near-surface reflectometry and positioning applications”. The main advantage of using the simulator is the possibility to rapidly obtain the possible SNR shape of a GNSS signal affected by multipath. The positioning and collection of the data for a GNSS antenna takes in fact longer time. To collect available data for an analysis such as the calculation of the height, an average timespan of 30 minutes is usually required. During this time the antenna should have the possibility to capture data from usually 4 or more satellites. Four is in fact the minimum guaranteed number of GPS satellite visible in the sky at any time. In case of physical constraint due to the environment it is not obvious that all of the visible satellites are useful. On the other hand, the simulator can generate such SNR values in a matter of seconds. Moreover a wide range of parameters allow the user to reproduce various types of situations and environments. The output data can also be used as a matter of comparison with the real collected data to ensure a better understanding of the interference affecting the signal.

4.2. Simulator output: SNR Trends

In this paragraph a set of results obtained by varying some options in the simulator will be displayed. More specifically, settings related to the following test campaign were tested in order to compare the results and understand the behavior of three different setups. The generated graphs present the SNR in dB while the abscissas axis in sine of elevation.

Figure 26 and Figure 27 present a first overview of these three configurations for a height over the reflector of 2 m. The first figure shows the SNR trend of the two antennas looking upward. In general the trend of both the signal is a sinusoidal wave. When the sine of elevation increases the signals tend to increase in mean value as well. Vice versa, the amplitude of the sinusoidal oscillations drastically reduces. This is consistent with the gain patterns shown in Figure 18 and Figure 23, reaching their maximum at zenith. The multipath fades away at increasing elevation due to the decreasing portion of RHCP signal reflect by the sea (Figure 14), followed by an increase in the absorption due to the water. The figures show how the choke ring antenna provides higher gain throughout the whole elevation interval. The graphs also highlight that fluctuations in SNR due to multipath are still observable at higher elevations with the choke ring compared to the other antenna. The higher gain of the choke ring antenna could be also source of high scattering whenever other interferences on the signal were not suppressed accordingly.

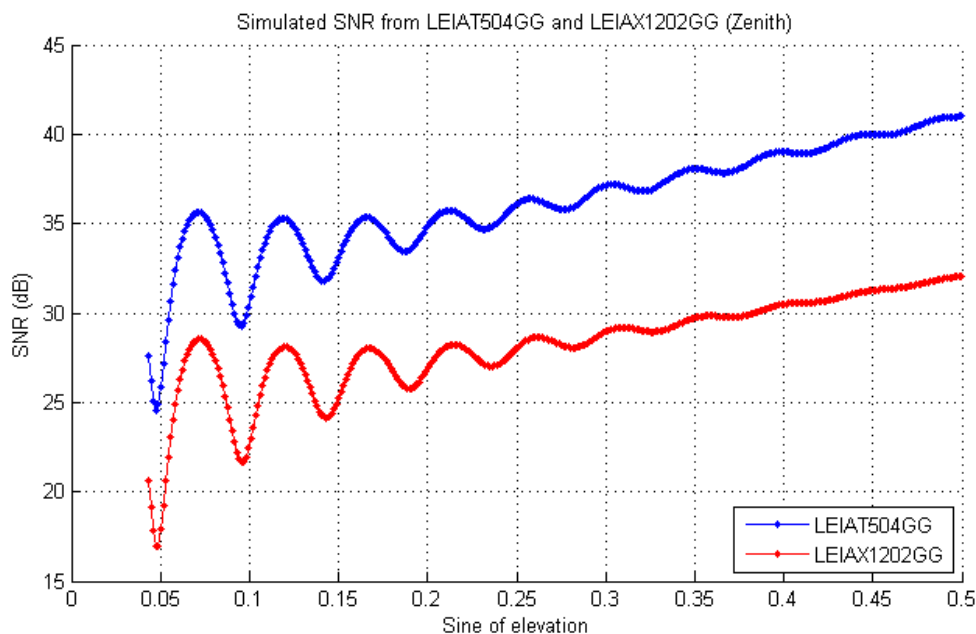


Figure 26: Simulated SNR for SEA1 and SEA2, both antennas are facing upward. Red = SEA1, Blue = SEA2

Figure 27 depicts the SNR of the same antenna, Leica AX 1202 GG, in two different positions: the blue arc is related to the antenna pointing upward while the green one relates to the antenna facing the horizon. This is primarily important when it comes to the gain pattern. In the second case in fact the antenna should enhance both signals: the direct one and the one from multipath. The graph shows this behavior: the blue trend is the same as in the previous figure while the green one has a much wider envelope. The elevation does not produce such a relevant effect as before. Vice versa, the trend seems to decrease with the rising of the satellite in its path on the sky. The situation presented in Figure 27 is inverted: when the satellite reaches its zenith the antenna has almost no gain in that direction.

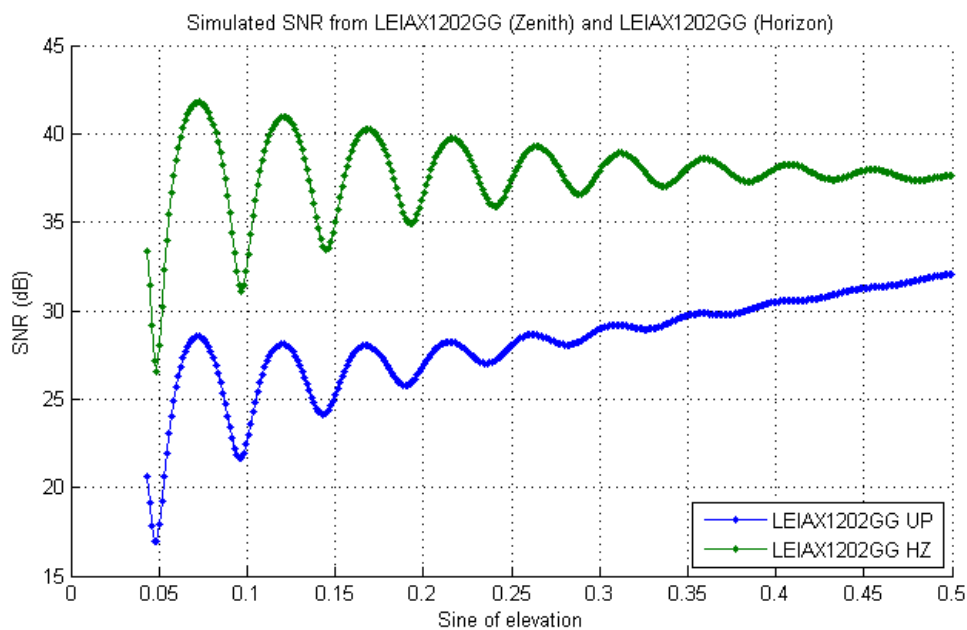


Figure 27: Simulated SNR for SEA2 and SEA3, same antenna facing upward and the horizon. Blue = SEA2, Green = SEA3

In the following paragraphs the importance of various parameters will be shown. In particular the input values for height, antenna angle, polarization, number of observations will be changed in order to observe the repercussion on the SNR. When not defined, general options are used as stated in Table 6.

4.2.1. Height

One of the parameters that can be changed inside the program is the height of the APC relative to the reflector. In our case this would be the sea surface, rising for decreasing height and decreasing for increasing height. Firstly a set of simulations for Leica AT 504 GG will be presented. Figure 28 and Figure 29 present this same antenna tested for three different heights: 1, 3 and 10 meters. It is straightforward to observe the increment of frequency when the distance between the antenna and the sea surface increase. This is consistent with Equation 3.

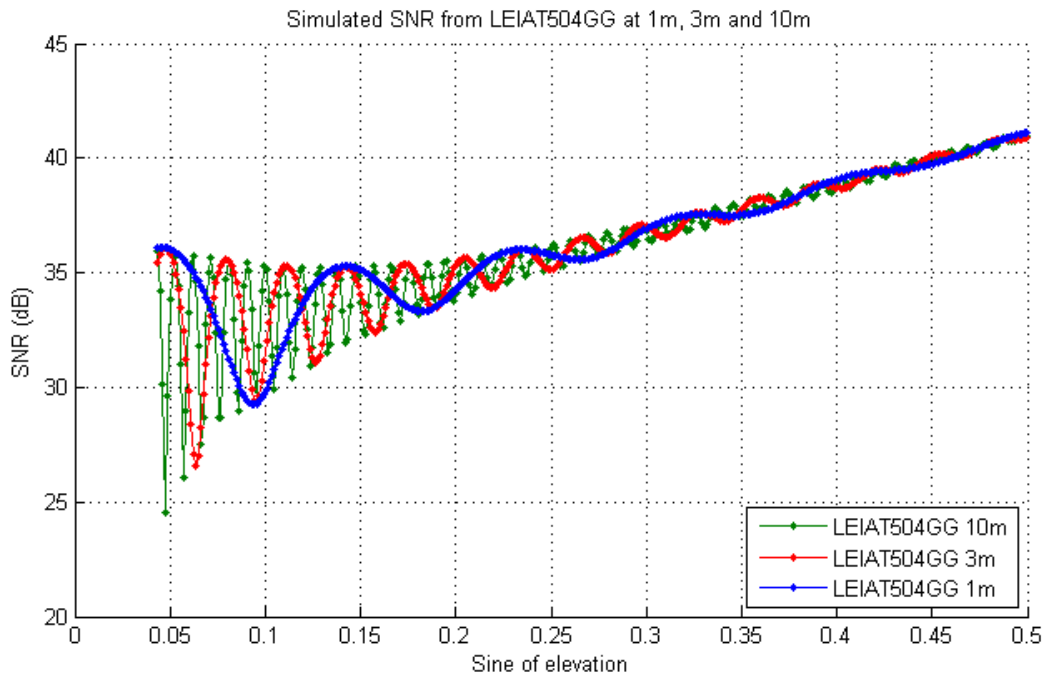


Figure 28: Simulated SNR for Leica AT 504 GG for heights of 1, 3 and 10 meters

Leica AX 1202 GG was also tested; the results are presented below and they are consistent with those acquired for the previous configuration.

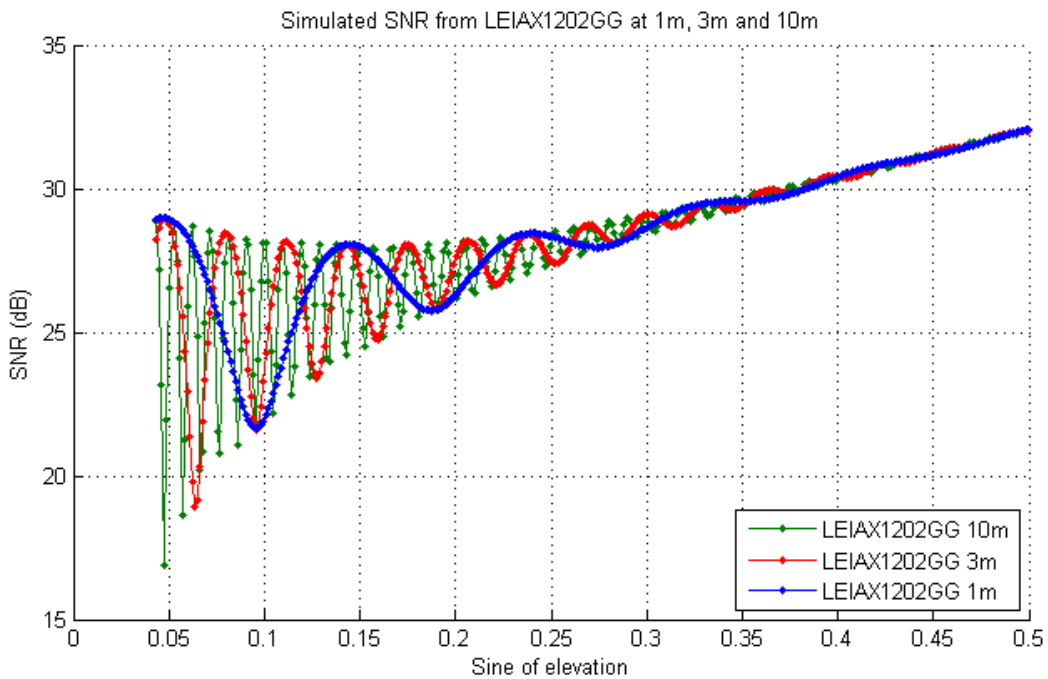


Figure 29: Simulated SNR for Leica AX 1202 GG for heights of 1, 3 and 10 meters

4.2.2. Antenna Orientation

In this paragraph, the relevancy of the antenna orientation will be observed. For this purpose only Leiax1202GG was used in order not to make the presentation of the data too repetitive. Figure 30 presents the antenna at 0, 45 and 90 degrees, where 0° means that the axis of revolution of the antenna is pointing upward towards the zenith. The blue arc depicts this configuration; the red sinusoid shows the signal for the antenna tilted by 45 ° while the purple one indicates the antenna facing the horizon.

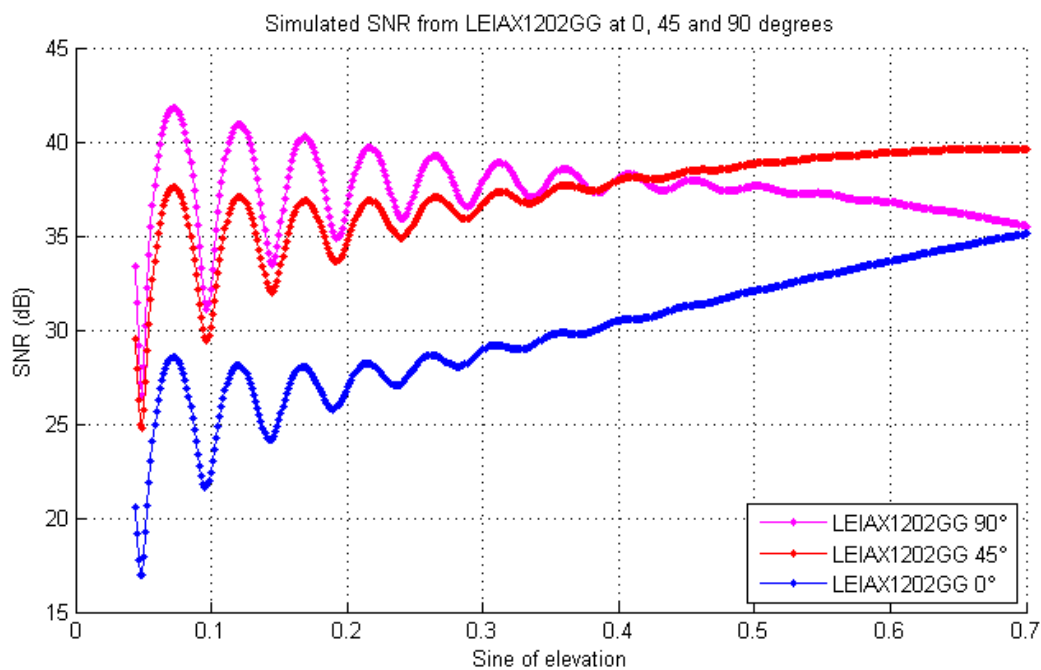


Figure 30: Simulated SNR for Leica AX 1202 GG at 0, 45 and 90 degrees

This is, again, consistent with what has been seen in Figure 27. For tilting angle of 90° the wave acquires a more stable shape fluctuating around a mean value of 35 dB. The Multipath effect interaction is increased; this can be seen by an increase of the wave amplitude throughout the entire elevation interval. It is possible to see that the magnitude of the first peak at 0° is around 10 dB while at 90° the same semi period covers an amplitude of 15 dB. By observing the graphs it can also be seen that the fluctuation continues to propagate even at elevation around 32° (sine32° is equal to 0.52). This allows a better estimate of the frequency of the arc, since more peaks are available for the analysis that will be described in 4.4. Lastly, Figure 31 presents both Leica AT 504 GG and AX 1202 GG tilted by 90 degrees with respect to the zenith. Once again the fluctuations are equally shaped with a constant offset of almost 11dB. The choke ring antenna shows better performance regarding signal acquisition, collecting more power from the incoming signals. For both antennas the effect of multipath is clearly visible until around 30° of elevation; in this case the choke ring antenna doesn't suppress the multipath in such

manner as in vertical position, due to the gain pattern that in this case enhance direct and reflected signals equally.

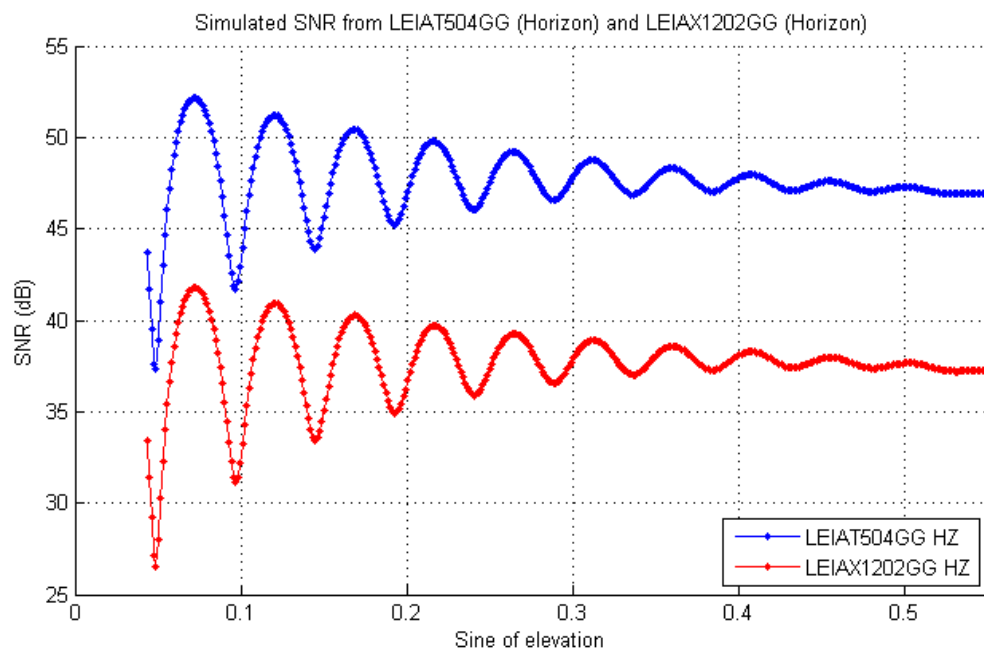


Figure 31: Simulated SNR for Leica AT 504 GG and AX 1202 GG at 90 degrees of orientation (Horizon)

4.2.3. Polarization

As it was said above, the following test campaign focus on the usage of RHCP antenna for L1 C/A signals. However, the usage of LHCP antenna could bring interesting results because circularly polarized signals can in some cases alter their reflection polarization from right handed to left handed (Hannah, 2001). This effect is more significant at higher elevations i.e., for reflective surfaces closer to the antenna. A test campaign focused on this issue has been previously carried out by Löfgren et al. (2010). Figure 32 depicts the simulated signal, with the blue arc presenting the standard input settings of a RHCP antenna. On the other hand, the crimson arc, depicting the LHCP antenna, shows a decisive different trend. Every peak is very clear and intense until around 30° while the fluctuation remains visible for all elevation observed. The graph also shows the irregularity of the SNR simulated, the signal is stronger between 15 and 22° of elevation and is not centered on a mean value. This could bring some problems for a further handling process that could follow the acquisition of the data. On the other hand the frequency of the peaks seems fairly regular, allowing to easily obtain useful results. An explanation on the shape of this arc can be found of an interaction between the gain pattern and the behavior of the reflected signal. As we said before in 2.2, the reflected signals from satellites with a high elevation angle are mostly LHCP. Hence, we assume that the LHCP component amplitude travelling to the antenna due to multipath is increasing with the elevation. Similarly for what happens for RHCP signal though, at a certain elevation an increasing portion of the signal is being refracted instead of reflected, leaving less

power to be received by the antenna. On the other, hand the gain pattern of the LHCP antenna is similar to the one for RHCP even though its behavior is more constant at high elevations. A small peak can be also seen at some negative elevation, as shown in Figure 23. For this reason we can think that the gain pattern affects the SNR in a similar way as for RHCP signals. It enhances multipath effects at low elevation while it slowly suppresses them for higher elevations. The combination of these effects brings to the graph presented. On the other hand, the antennas used in this thesis are not designed to be used to acquire such signals. Figure 32 clearly shows that the gain pattern for LHCP signals is an average of 10 dB lower than the one from RHCP signals (Markvart, 2003).

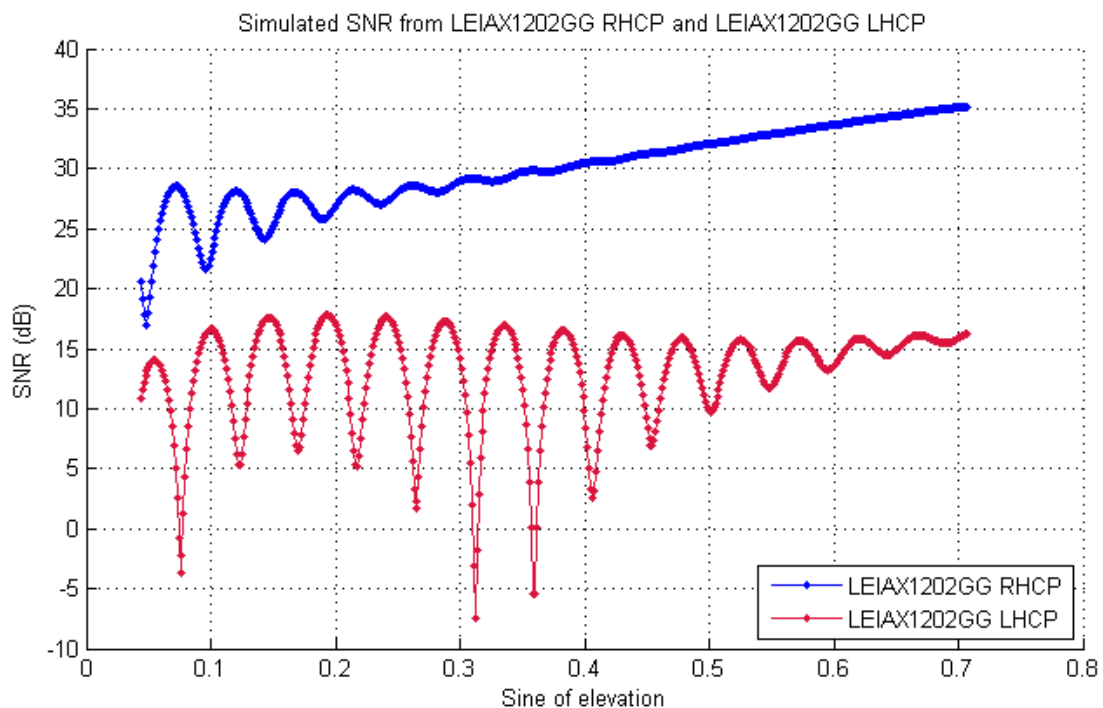


Figure 32: Simulated SNR for Leica AX 1202 GG RHCP (blue) and LHCP (crimson)

4.2.4. Observations

The number of observations is a factor that can be also set; this consists in the number of points that underline the function. Increasing its values brings to a denser data set that can be further analyzed. While this allows better results and less probability of errors, it also brings to a major increase of the processor work-load. Figure 33 presents two simulations, one carried out using 300 points (blue circles) and one using 900 points (purple dots). As it can be seen, the shape of the sinusoid is the same, but the density of points is higher; this allows better time accuracy and better characteristics estimation while handling the output data.

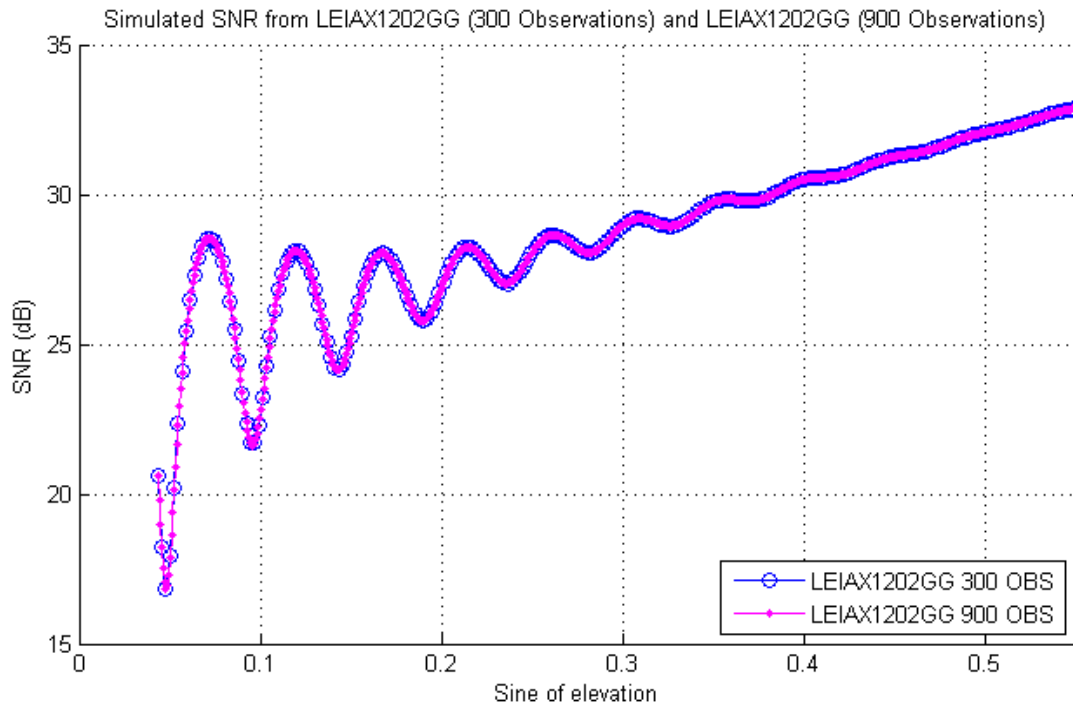


Figure 33: Simulated SNR for Leica AX 1202 GG simulations achieved through 300 and 900 observations

4.2.5. Surface material

The last set of options evaluated regards the bottom material composition. This is important for the SNR simulation because it determinates the properties of the reflecting surface, such as reflectivity and refractivity. Figure 34 presents the SNR for two similar materials: sea water in blue and fresh water on light blue. A small offset in phase can be seen in this graph: fresh water appears to anticipate the in-phase off-phase phenomenon. In other words, the same trend is observed also with fresh water but the same value occurs at minimally lower elevation. At the same time the amplitude of the oscillation seems slightly reduced for sine of elevations between 0 and 0.2 and slightly higher above 0.2. This behavior appears reversed in Figure 35, where salt water is compared to snow. In this case the effect of multipath is enhanced and the amplitude of the oscillations is larger. In fact, the composition of the snow tends to have a higher reflection.

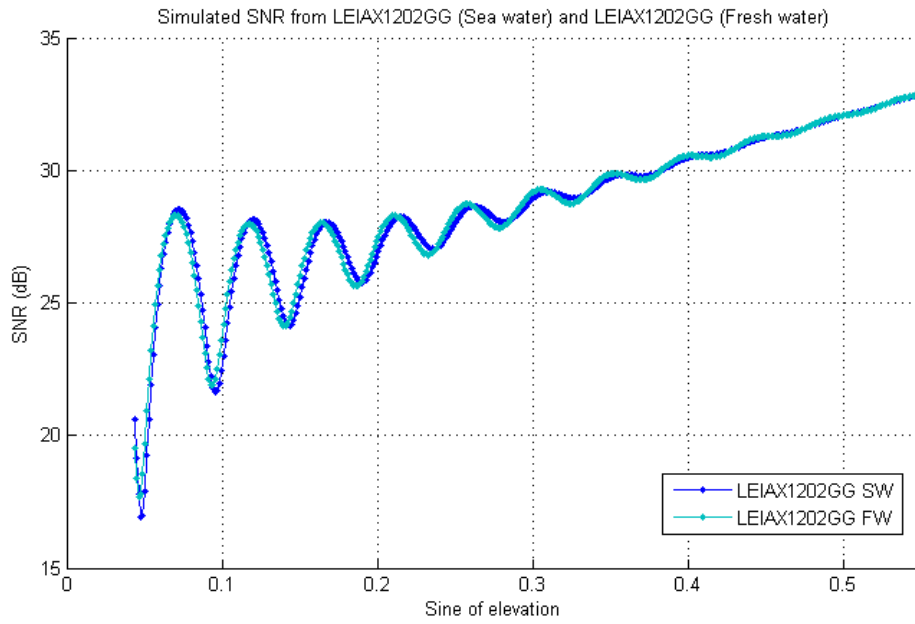


Figure 34: Simulated SNR for Leica AX 1202 GG simulations over salt (blue) and fresh water (light blue)

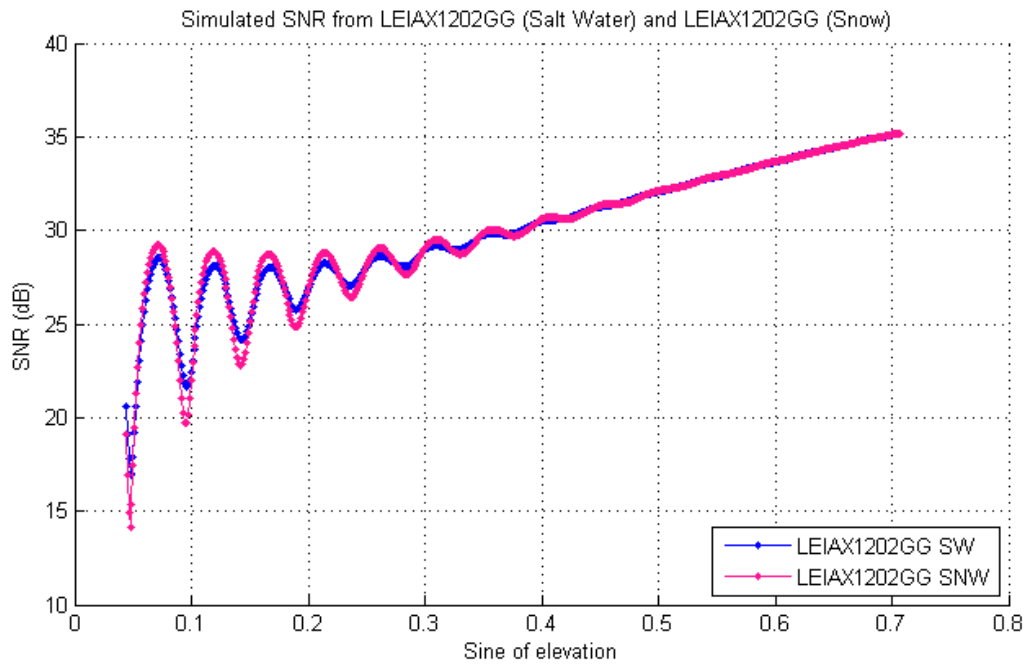


Figure 35: Simulated SNR for Leica AX 1202 GG simulations over salt (blue) and snow (violet)

4.3. Testing procedure for simulated results

Once this general evaluation was carried out, the accuracy of the MATLAB code itself was tested. Even though the graphs well resembled the shape of an actual signal with multipath interference, errors could have been introduced by the simulator. In particular, the arcs could have been generated with

features resembling reflector heights different from those of input. In order to verify this possibility, a small test was performed. A set of reflector heights were given as input to the simulator, ranging differently for SEA1 than for SEA2 & 3. This is due to the fact that in the test campaign, the choke ring antenna was positioned at higher over the ocean than the other 2 antennas. Table 7 presents additional parameters added to the simulator settings in order to perform the test.

Table 7: Additional parameters set in the simulator to perform the testing

Parameter	Value [unit]	Description
Number of observation	500	Number of points per arc
Elevation Mask	5-32 [°]	Elevation path of the signal
SEA1 Range	2 – 5 [m]	Interval of height tested
SEA2 & 3	1 – 5 [m]	Interval of height tested

The procedure of the test is depicted in Figure 36: a reflector height was given as input to the simulator which simulated the received SNR signal. The simulated SNR data were given as input to a function that was performing a Lomb-Scargle Periodogram. From the LSP a new reflector height was estimated. After this process, the estimated reflector height relative to the SNR data was extrapolated and compared to the one inserted in the simulator as input by the user.

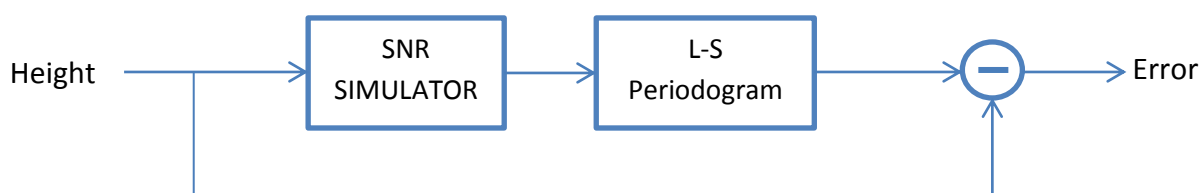


Figure 36: Simple scheme resembling the testing procedure to evaluate the accuracy of the simulator.

4.4. Simulation setup and height calculation

The MATLAB script presents also other characteristics both in input and output, as shown in Table 8. The program requires multiple inputs: the data set, the coordinate vector related to the data, the oversampling factor “*ofac*”, and the highest frequency analyzed for the periodogram.

In some cases the data were detrended before being given as input in the function. This is done by subtracting a second order polynomial function fitted to the data, to the data themselves.

Moreover, the conversion from dB to linear scale was performed and from the results the mean value

was subtract, to enhance the quality of the results.

The oversampling factor, as the name says, is the ratio at which the script oversample the data. In other words, the fundamental sampling frequency is related to the time difference between two points. The minimum independent frequency examinable is the inverse of the timespan of the data, and every other frequency analyzed is an integer multiple of this base frequency. Because it is important in this analysis to observe all the peaks closely and define their importance inside the periodogram, it is useful to oversample the curve. This means to reduce the minimum frequency and moreover refine the increment step of the analysis. In this way more points would be available close to the peaks that are the most critical points. In this analysis the oversampling factor is chosen to be 80 after a previous testing session with a value of 40. This brings slightly higher precision while it doesn't apparently affect the time needed for the calculation.

The highest frequency analyzed is introduced into the function as a multiple of the Nyquist frequency. This factor is been chosen as 0.95 to slightly reduce the workload of the function, given the fact that the peak is supposed to be detected at low frequency. Moreover, using a wider range of frequency, i.e. having a *high frequency factor* above one, could bring to mirroring of the peaks that complicates the resolution of the problem. The general setting of the LS functions can be summed as shown in Table 7 and Table 8.

Table 8: General setting used for the test session

<code>[f,P,prob,conf95]=lomb(sind(result.elev),result.snr,80,.95)</code>		
	Parameter	Description
INPUT	<code>sind(result.elev)</code>	Sine of elevation of the sampled points
	<code>result.snr</code>	SNR of the sampled points
	80	Oversampling Factor
	0.95	Highest frequency evaluated as a fraction of the Nyquist frequency
OUTPUT	<code>f</code>	Frequencies
	<code>P</code>	Amplitude of the LS Periodogram
	<code>prob</code>	False-alarm probability of the null hypothesis
	<code>conf95</code>	95% confident level amplitude
<code>[P,f,prob]=lomb_2(result.snr_db,sind(result.elev),0,.95,80)</code>		
INPUT	0	Flag imposing to the function not to create any graph

As outputs, the function produces the frequency analyzed and used to define the periodogram along with the amplitude associated to the related frequency. In addition, the statistical significance for every amplitude value is given, i.e. an indicator of the quality of the data set and on the possibility of them to be composed of independent Gaussian random variables. Low probability of noise is related to a high significance on the periodogram, in other word this means that the data set is highly related to sinusoids with that proper frequency. Lastly the 95% confident level amplitude is produced and given as output.

Two different scripts were used in order to ensure the truthfulness of the results obtained, one made by Dmitry Savransky in 2008 and the other by C. Saragiotis also in 2008. Figure 38 and Figure 39 show a typical result obtainable from these functions. The former presents the actual normalized LS Periodogram, as amplitude against height while the latter presents the significance of each frequency. As said, in the graph the frequency does not figure as abscissa, but it has been converted to by the height in order to easily understand the distance between the antenna and the reflector. If we compare the detrended data with the formula, we observe that the arc is shaped as a sinusoid with a given frequency driven by the sine of elevation. The sinusoidal trend is given in the formula by the cosine. The amplitude A in Equation 3 is not relevant for the experiment, what remains to do is to match the trend of the fluctuation with the argument of the sinusoidal function. Another small routine had to be implemented in the program to obtain the actual height of the reflector, by detecting the highest amplitude of the periodogram, and retrieve the related height. Figure 38 and Figure 39 show a general result from the functions described above. The data inserted to achieve the graph are shown in Figure 37, as a detrended linearized version of the SNR profile ($dSNR$). Figure 38 present the output form the LSP converted to show the data with respect to reflector height. Figure 39 depicts the significance of each height (frequency) and it is obtained subtracting the probability value, output of the MATLAB function, to 1.

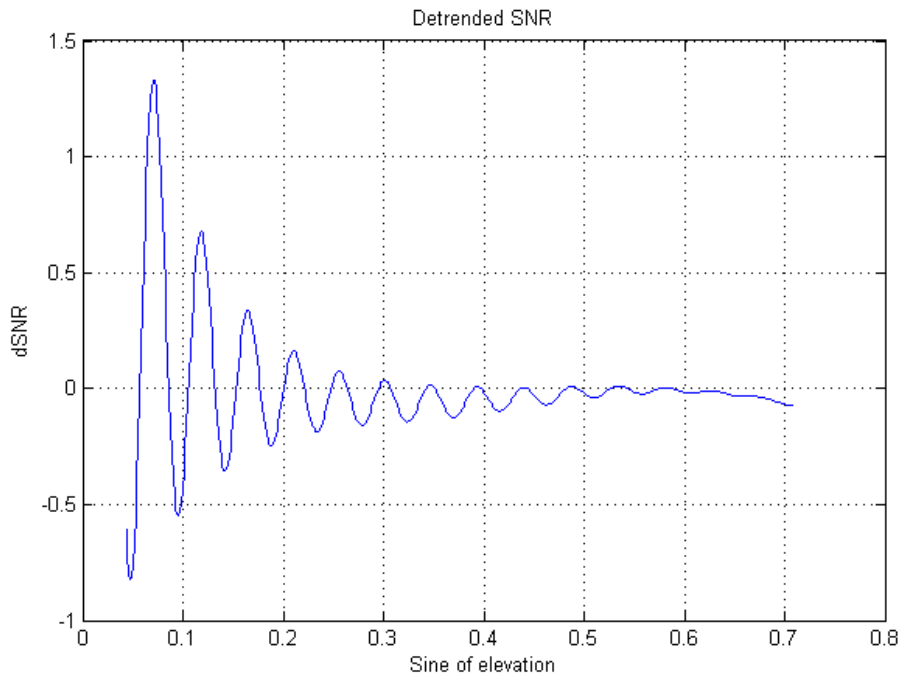


Figure 37: Typical shape of a detrended SNR profile

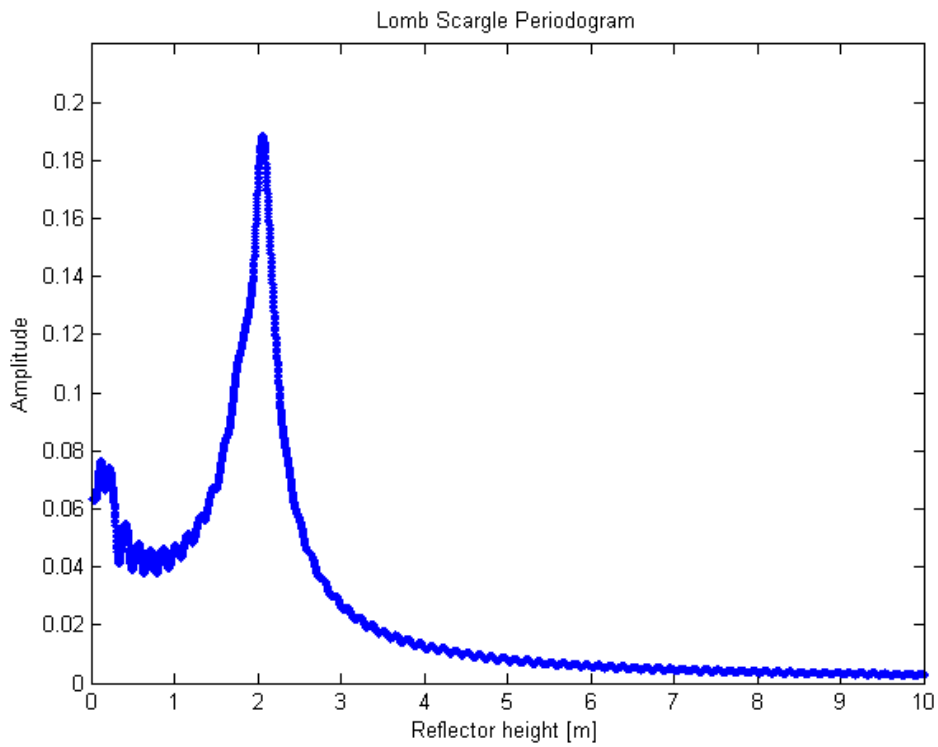


Figure 38: Typical normalized LS Periodogram

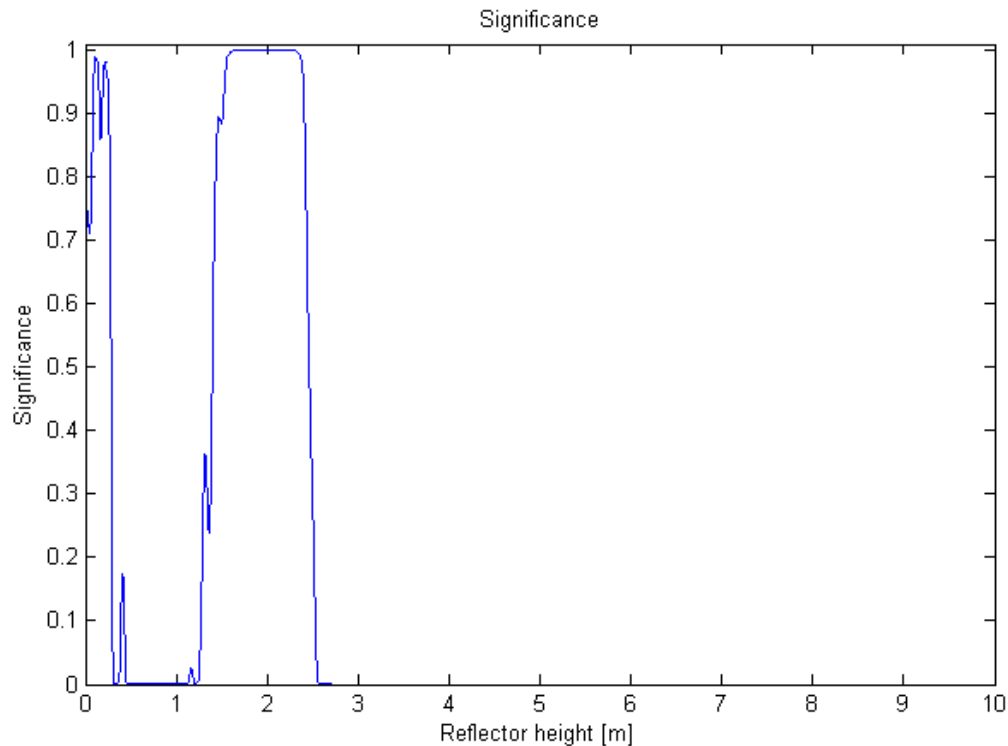


Figure 39: Relative significance of each height

4.5. Test results and discussion

In order to test the accuracy of the simulator, a simple routine was implemented in MATLAB: a set of reflector heights was inserted in the simulator. The SNR data were generated, then the heights were estimated via LS Periodogram and they were compared to those used as input.

All three configurations were firstly evaluated with an oversampling factor of 40; Figure 40, Figure 41 and Figure 42 show the results obtained for SEA1, SEA2 and SEA3 respectively. In each figure both trended and detrended data are shown. In this way it is possible to observe the enhanced stability of the resulted obtained after detrending the data. The results in the first two figures appear to be similar: this is probably due to the orientation of the antenna that is the same. In fact both SEA1 and SEA2 are directed with their vertical axes pointing upward. As explained before, in these cases the interaction between direct and reflected signal does not generate an SNR with such amplitude as the one for the tilted antenna. The SNR trend shows an oscillating value that increase with the sine of elevation. If this trend is subtracted, the remaining data resemble a sinusoid whose frequency of the oscillation is easier to estimate. The error for trended data oscillates between 3.5 and almost 17 centimeters while if the data are detrended the error remains almost stable near 7 cm circa. This behavior is similarly reproduced by SEA2, while in this case the average error is slightly less: around 4.5 cm. The higher value

of SEA1 can be justified by the different structure of the gain pattern of the two antennas. SEA1 is more suitable to suppress multipath effects and could make the height estimation slightly less precise.

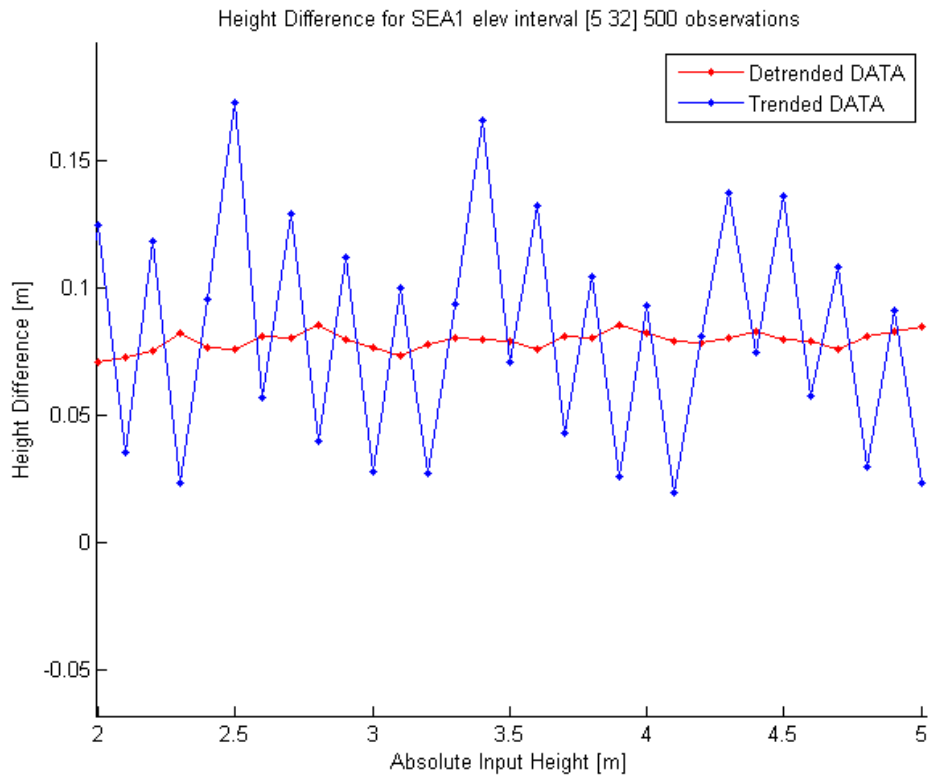


Figure 40: Height difference between input data and simulated data for LEICA AT 504 GG (upward)

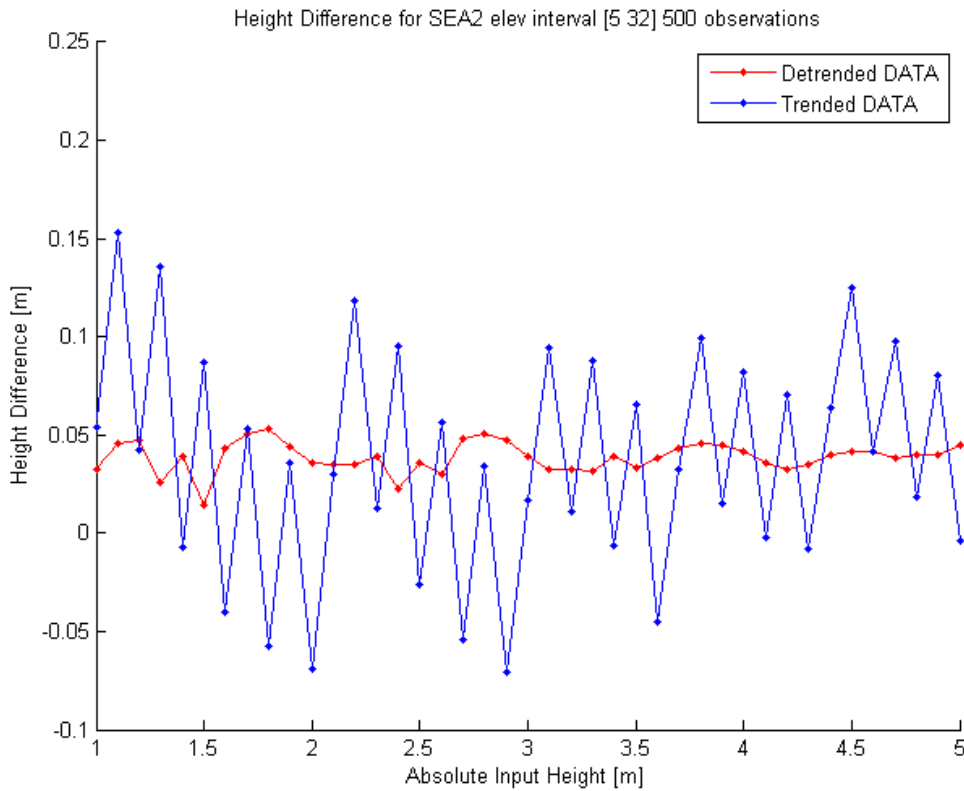


Figure 41: Height difference between input data and simulated data for LEICA AX 1202 GG (upward)

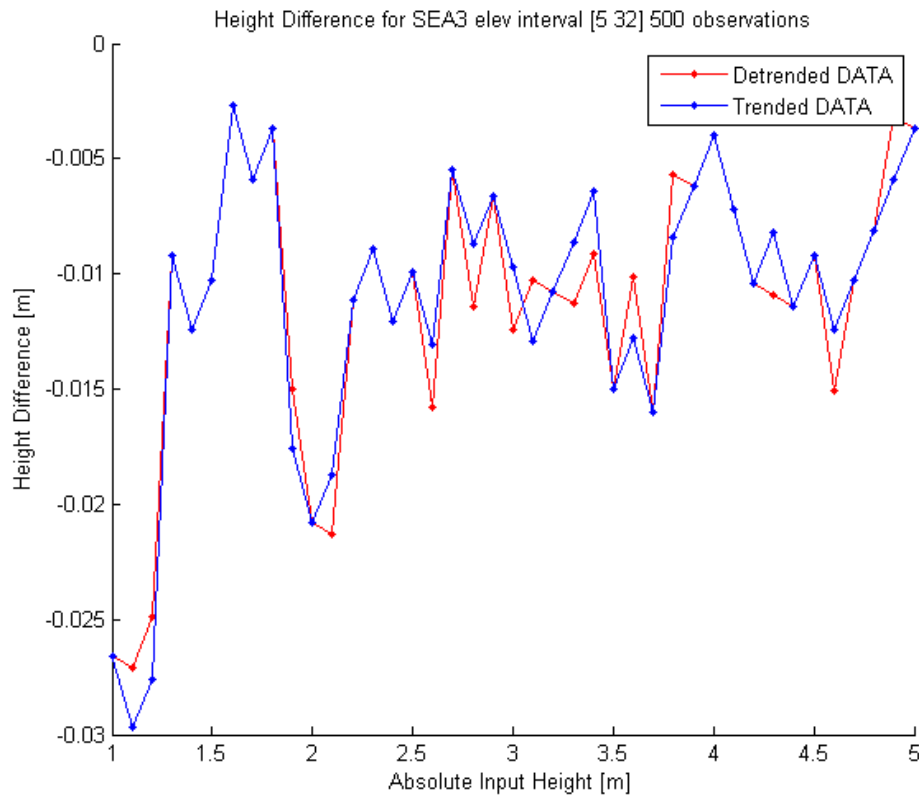


Figure 42: Height difference between input data and simulated data for LEICA AX 1202 GG (horizon)

As it is shown in Figure 42, the error in height for oSEA3 is less affected by the detrending procedure. In this case, the unprocessed data from the simulator are already suitable for the LS Periodogram analysis because they well resemble a sinusoid with almost constant mean value. In both cases the error remain less than 3 cm and for most of the heights is also minor than 2 cm. This probably due once more to the higher power acquired and the higher number of peaks noticeable with SEA3 in comparison with the other setups. Moreover, the sinusoidal function develops with high linearity with respect to the sine of elevation. This allows to easily and univocally detect the frequency of the oscillation. The peaks highly differ from the mean value of the SNR and the interaction between signal and interferences is maximized.

As said before, the oversampling factor incidence was analyzed. Even though this has minor relevance compared to the error due to detrending or other setup settings, it could play a role for further implementation in case of increasing the precision or in case of high frequency data introduced in the LS function. When the data used for this were taken directly from the simulator without any modification, the behavior for the three configurations was similar. As shown in Figure 43, using a factor of 80 instead that 40 generates a slight discrepancy on the result that remains below 1 cm. This is due to the higher density of points on the Lomb Scargle Periodogram that allows defining more precisely the effective peak frequency, and from it the height. Even though this few millimeters does not change the result as much, the computational load added does not seems to create an appreciable increment of time

needed for the calculation. For this reason, the usage of such value is recommended for further LS analysis, especially in case of data with strong variations. On the other hand, its effectiveness seems absent in case of detrended data, as shown in Figure 44. The lines match perfectly and there is no error. In this case is thus inefficient to use a higher factor even though when handling real data the difference can result more relevant.

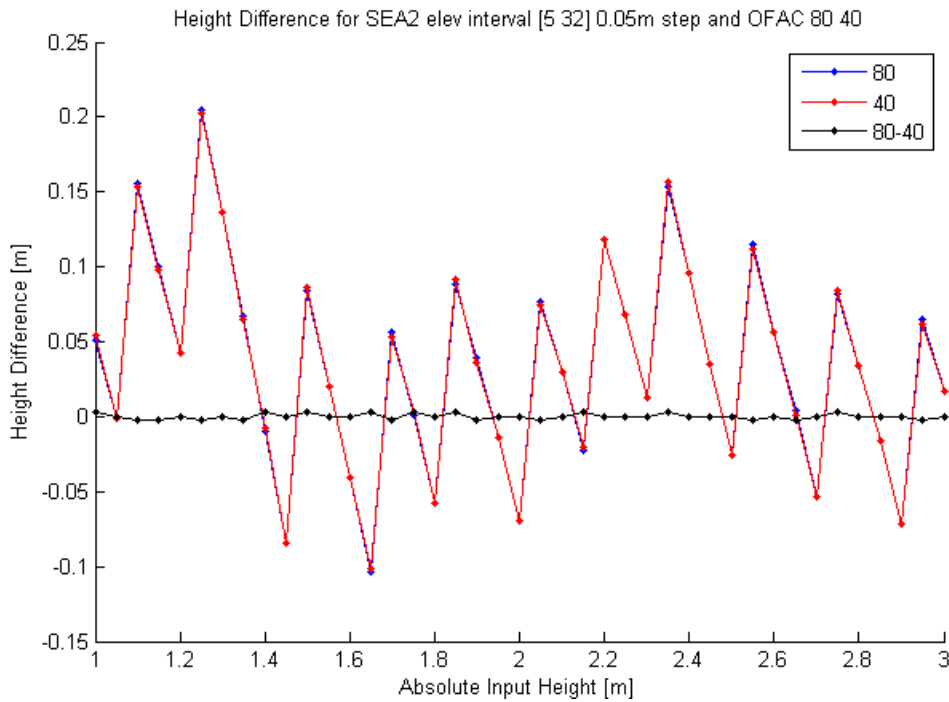


Figure 43: Offset between height calculation with oversampling factor of 80 and 40, using LEICA AX 1202 GG (trended)

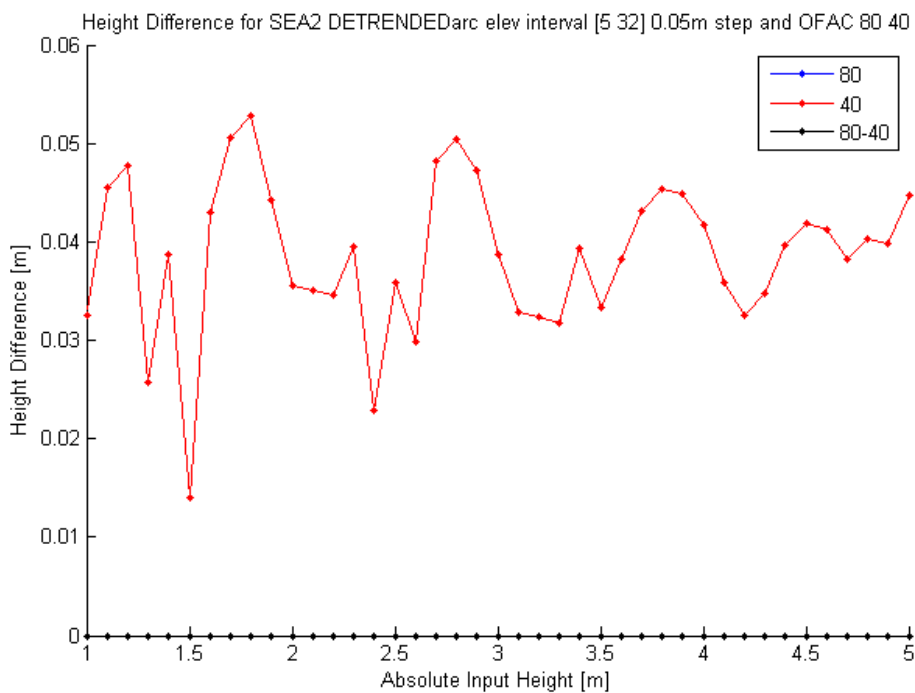


Figure 44: Offset between height calculation with oversampling factor of 80 and 40, using LEICA AX 1202 GG (detrended)

At the end of this analysis, there is still to understand the reason why the error, whatever the configuration is used, is still persistent on a value that is of the order of centimeters. This could be due to other characteristics of the environment that were not taken into consideration. For example roughness, reflectivity and refractivity affects the behavior of the signal and the power received by the antenna. The impact of the bottom material on the SNR behavior was later investigated. The input data were set to *perfectly electric conductor* as bottom material. This imposes the signal to be entirely reflected by the surface with no loss of information due to absorption or scattered diffusion. In this way, the SNR fluctuation is more constant in amplitude throughout the elevation interval, the shape is more homogenous and the multipath effect is clearly visible at high elevations. Figure 48 shows an example of detrended data, it can be seen that the oscillation is regular, clearly noticeable and with high amplitude for the whole interval allowing a precise calculation of the height. If compared with Figure 37 where the high peaks were essentially three/four, the latter graph provides at least six/seven high peaks. Results can be observed in Figure 45, Figure 46 and Figure 47 for SEA1, SEA2 and SEA3 respectively. As can be seen, the error is now constrained into an interval of few millimeters, with a maximum of 5 mm in the interval from 1 to 5 meters. This residual error can be due to imperfection in the program generating the data or in the LS analysis for reason related to sampling, transformation and processing limitations. The values are nevertheless so minimal that can be accepted as an imprecision of the entire program that for this reason appear to be fairly accurate. Moreover, previous experiments on height calculation have shown the possibility to measure the reflector height with a precision of few centimeters (see 2.4). Hence, the simulator error is negligible when compared to these results.

SEA LEVEL MEASUREMENT USING SINGLE GNSS ANTENNA SNR SIGNALS

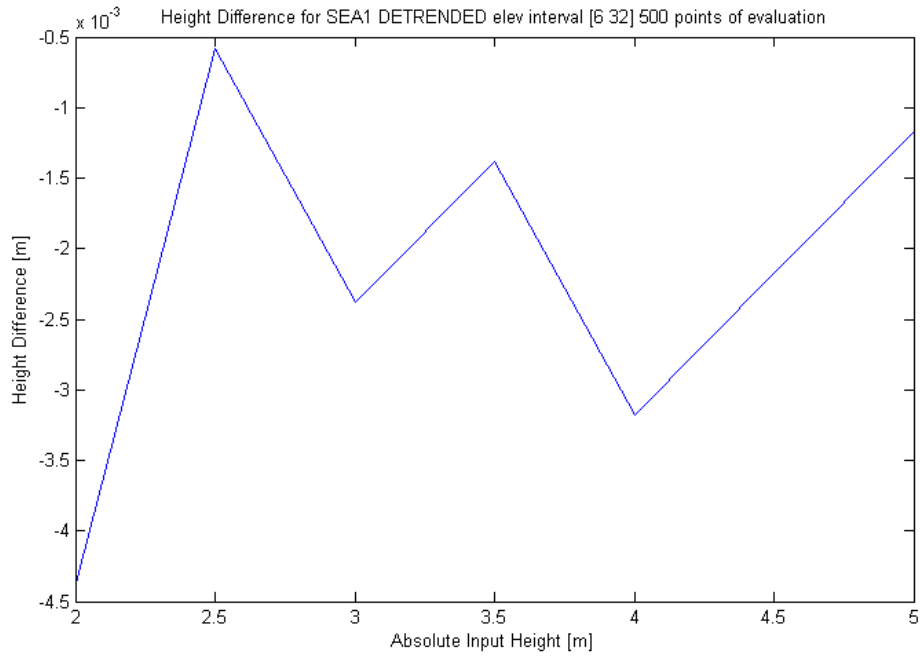


Figure 45: Height difference between input and output data for LEICA AT 504 GG (PEC, detrended, ofac 80, upward)

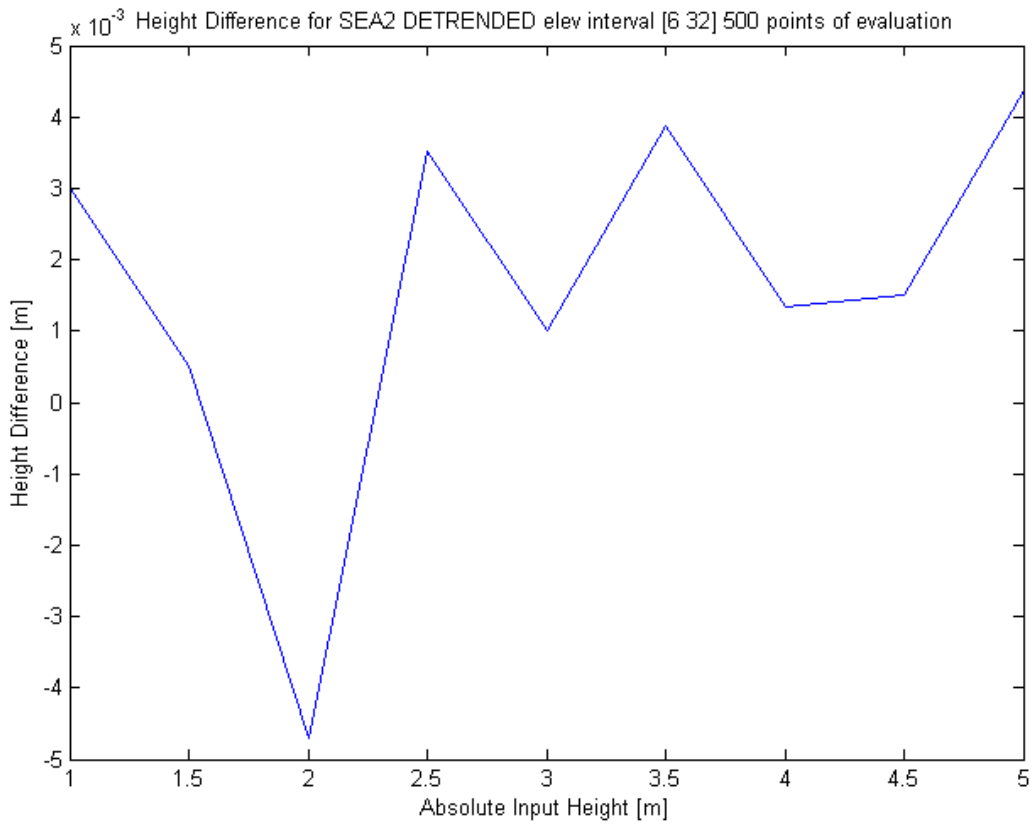


Figure 46: Height difference between input and output data for LEICA AX 1202 GG (PEC, detrended, ofac 80, upward)

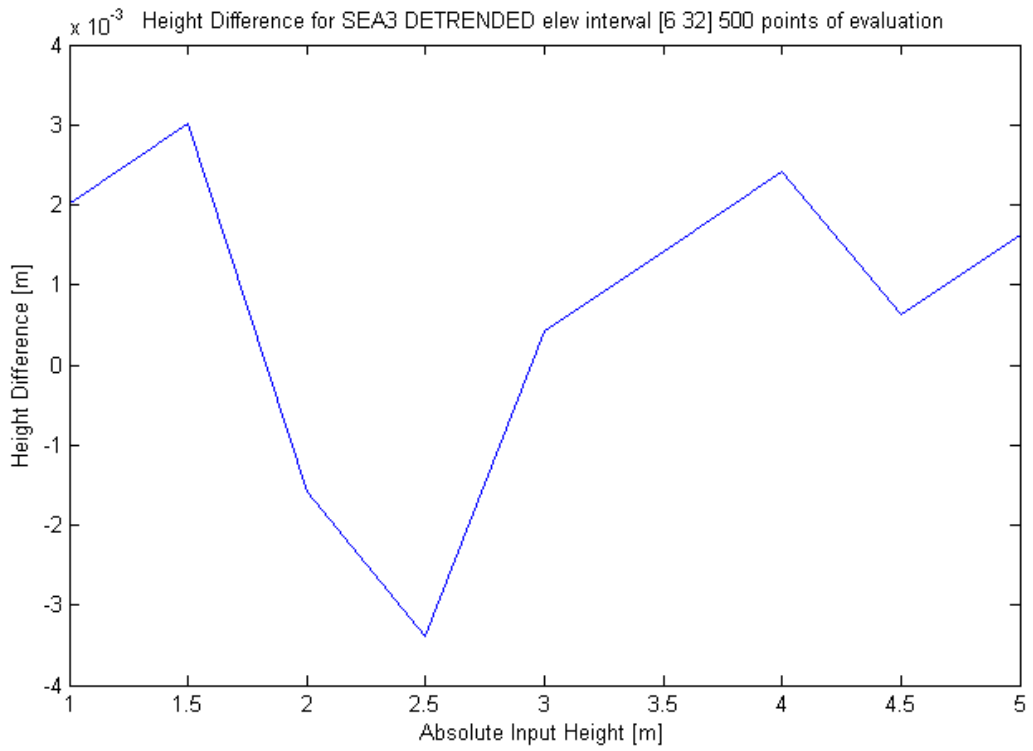


Figure 47: Height difference between input and output data for LEICA AX 1202 GG (PEC, detrended, ofac 80, horizon)

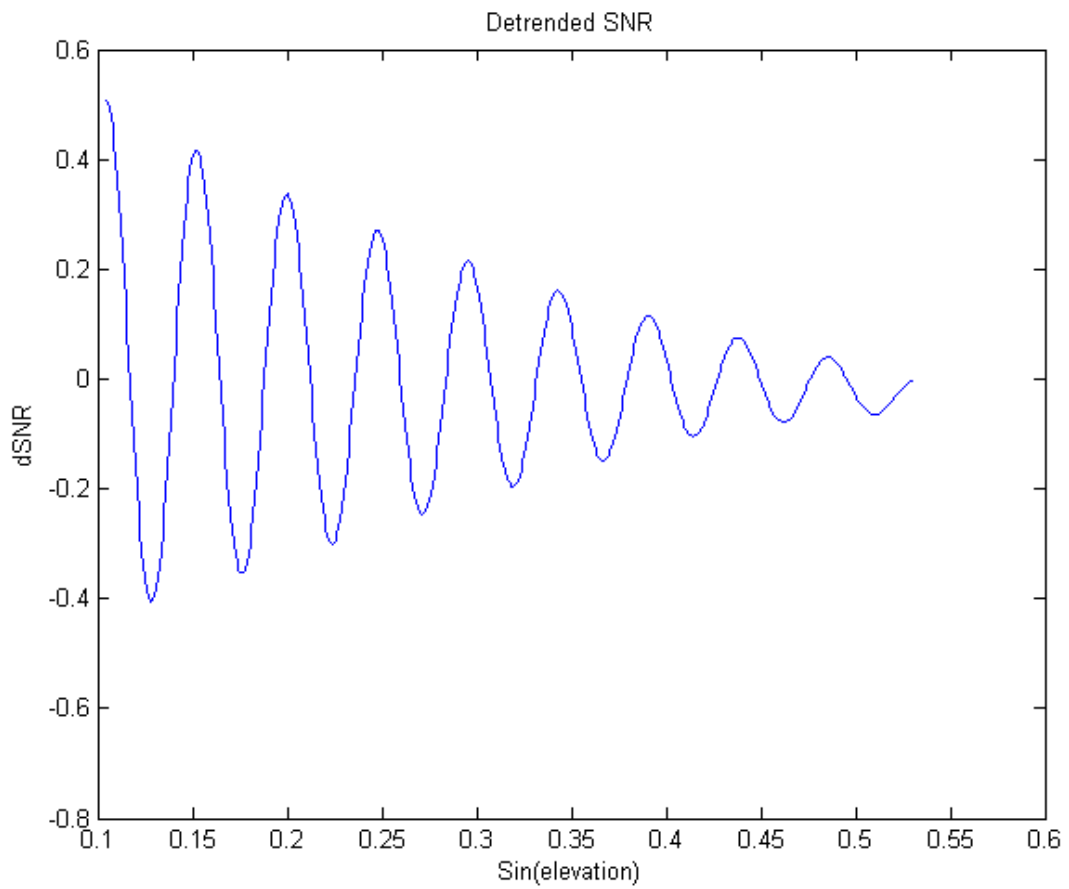


Figure 48: Detrended simulated data for LAICA AG 504 GG for an input height of 2m

5. Sea Level Measurements

5.1. Introduction

The main task of this work is to analyze the possibility of retrieving sea level variations utilizing GNSS signals affected by multipath propagation. In particular, a new configuration compared to those studied by Löfgren et al. (2010, 2011a, and 2011b) is being observed. This consists in tilting a geodetic antenna by 90° in elevation to direct the largest fraction of the gain to the horizon, where the main part of the reflected signals is coming from. At first, the configurations used will be overviewed as well as the data acquired. Later, the software will be described and the constraints imposed to elevation and azimuth angles will be presented. Successively, the sea level measurement will be observed and compared to known data. The relation between the configurations will be also observed as well as the possible effects of weather conditions on the measurements. Lastly, possible methods to enhance accuracy and time resolution of the data will be tested, along with the usage of combination of multiple antennas for data cross-check.

5.2. Experiment Configurations

As explained before three antennas were utilized to perform the experiment. This was made in order to evaluate the actual performance of the software with different input. Löfgren et al.(2010, 2011a, 2012b) have tested the feasibility of upward looking antennas of different models, and thus this configuration should produce similar results. In this case different antenna were used, one Leica AG 504

GG and two Leica AX 1202 GG as explained in 3.2 and 3.3. The location of the experiment was chosen to be near the Onsala Space Observatory, on the west coast of south Sweden, near the city of Gothenburg as shown in Figure 49. The red dot refers to the city of Gothenburg while the yellow one defines the position of the experiment. The antennas were located on a bay close to the 25 m outdoor antenna dish of the observatory, in an area of rocky seashore and in presence of islands, as shown in Figure 50. This could cause problem in term of unwanted reflections from surfaces diverse from the sea water.



Figure 49: Location of the experiment (yellow) with respect to Gothenburg (red)



Figure 50: Location of the antenna with respect to the observatory

The red arrow is pointing north, while the two lines define the range of direction from which it is supposed to receive good reflection from the sea without strong interference from the land for short distances.

Leica 504 GG "SEA1" was positioned on a rock on the side of a small cabin as depicted in Figure 51; in this image it is possible to see the narrow interval of clear sea available in front of the cabin. Figure 52 and Figure 53 show particulars of this same antenna, once again, it was positioned on a tripod with the dish looking upward to maximize the gain of the direct GNSS signal. The island on the best direction possible is almost 100 m (Löfgren et al 2010) away so it allowed to use a wide range of elevation.



Figure 51: Location of Leica AT 504 GG



Figure 52: Particular of Leica AT 504 GG



Figure 53: Particular of Leica AT 504 GG Position (Antenna not present)

Two Leica AX 1202 GG were positioned on a dock near the cabin as shown in Figure 54. One, called “SEA2” was pointing upward as for the first antenna, while the other named “SEA3” was pointing to the horizon (90° tilt) to enhance the effect of the multipath. Even in this case the presence of obstacles reduced the visibility of the antenna. Figure 55 shows the point of view of view of SEA3 and SEA2; it can be observed that in this case the limitations are less than in the previous case.



Figure 54: Particular of Leica AX 1202 GG



Figure 55: Point of view of SEA3

5.3. Experiment Parameters and Physical Constraints

From what can be seen in the previous paragraph, some limitations have to be imposed in term of the direction of the incoming signals. Firstly, the azimuth has to be evaluated: SEA1 presents a mass rock that covers one side, an island at almost 10 meters plus the cabin on the another side. From 0 to 45° the azimuth covers a portion of land so the data are not usable. From 45 until 120° the available sea surface is reduced due to the presence of the small island, in this case only high elevation angle may be used. From 120 to almost 200 degrees circa, the surface available covers a horizontal distance of almost 100 meters. Above 200° the presence of rock nullify the SNR acquired. SEA2 and SEA3 the interval of clear surface is slightly wider, from 110 to 200°. A useful visual result is presented in Figure 56, Figure 57, Figure 58 and Figure 59; these show the different segment of one satellite, drawn accordingly to their mean azimuth angle. In other word, each arc starting point fixed the mean azimuth value of the interval, thus allowing to detect the valuable angle for the analysis. Fortunately, there were not many segments at angles below the interval selected. Inside the azimuth span chosen, the arcs are sufficiently consistent with the expectation and should provide satisfying results as well as those at the borders of the intervals. The data collected using SEA1 seems less suitable for the processing needed to retrieve the height, once more due to the high capacity to suppress multipath effects. At high azimuth angles, several arcs seem to have a very regular shape and a well-defined oscillation frequency for SEA3. This could be the case of the reflection coming from the house nearby or from the jetty where the antennas were placed. These produce a SNR fluctuation that is quite steady thanks to their smooth surface and to

their fixed position, differently from the sea level, affected by tides and waves. The hypothesis of the house could be also partially justified by the fact that the frequency seems to be higher than the one of the signal reflected by the sea surface. This means in other word that the reflector is more distant from the antenna that the water surface.

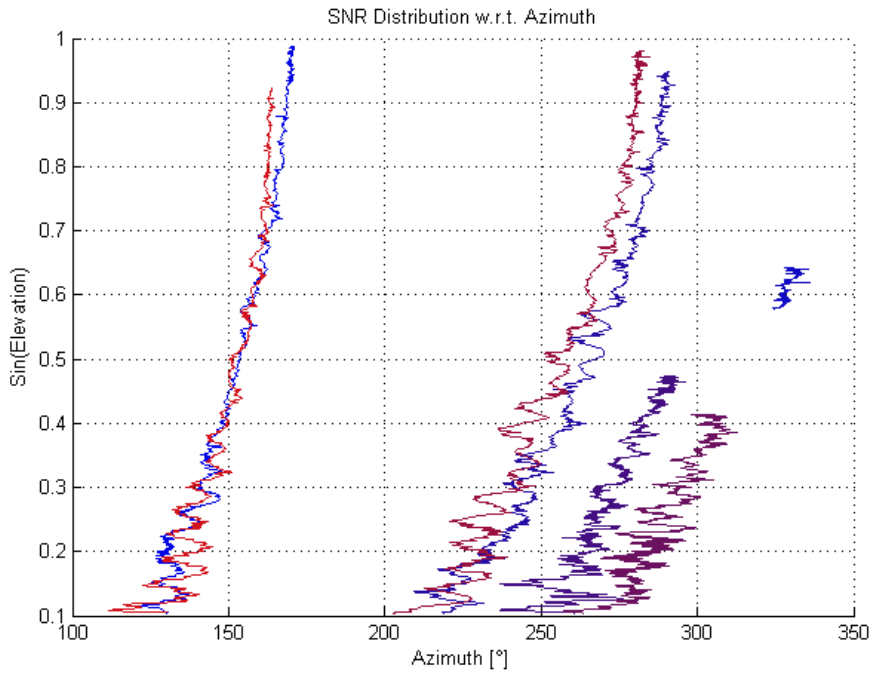


Figure 56: Typical signal distribution throughout the azimuth range of SEA1 (DOY 267)

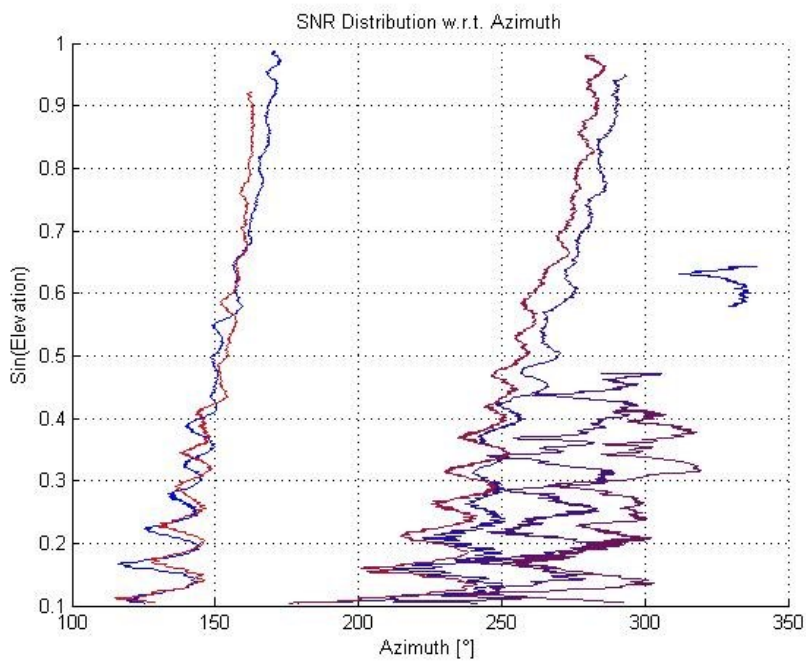


Figure 57: Typical signal distribution throughout the azimuth range of SEA2 (DOY 267)

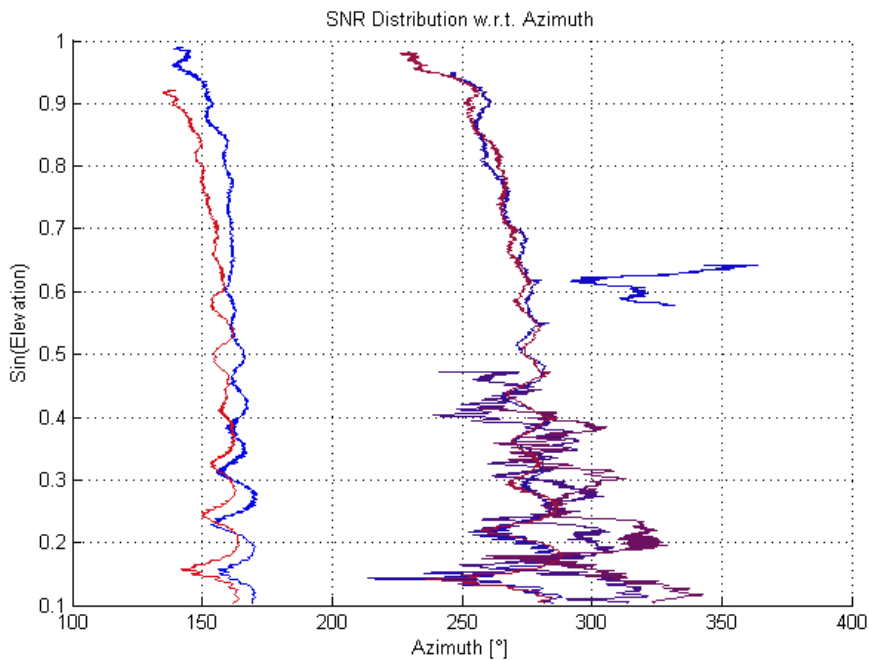


Figure 58: (A) Typical signal distribution throughout the azimuth range of SEA3 (DOY 267)

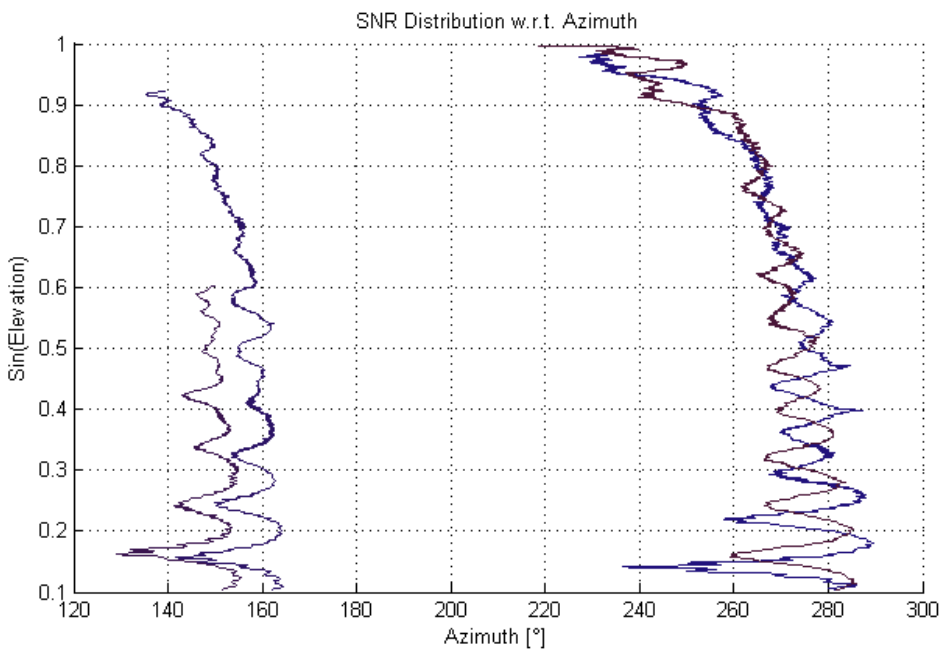


Figure 59: (B) Typical signal distribution throughout the azimuth range of SEA3 (DOY 267)

As explained before, the elevation gap is directly related to the azimuth mask selected for the experiment. For the case of land at a distance of 100 meters, supposing in the worst case a height of 2.7 meters for SEA1, the minimum elevation angle is 1.54 degrees that bring to a sine equal to 0.027. Assuming the closest distance observable to be 1.5 meters, the maximum elevation angle is of 60 degrees that lead to a sine of 0.87. When the antenna acquires SNR data from the area near the small island across 90° of azimuth the elevation interval has to be stricter. If a conservative distance of 6.5

meters is supposed, the minimum elevation it is estimated to be acceptable at 22.5°, with a sine of 0.38. Similarly, we can suppose a conservative height of 1.7 meters for SEA2 and SEA3 and thanks to trigonometric relations the relative angles can be derived. Table 9 sums the possible direction of the incoming reflected signals, while Figure 60 depicts the described azimuth constraints and highlights the area of clear sea surface.

In order to be conservative, strict intervals were chosen to facilitate the elimination of the errors. For the areas at low azimuth the interval was chosen, between 0.38 and 0.7, while for the main area the boundaries were all between 0.1 and 0.65. These was done after multiple observation of the data acquired and with the goal to provide sufficient data to the LS function while at the same time providing highly defined peaks. Due to the low quality of the results, the lower interval of azimuth was discarded in the case of SEA2 and SEA3.

Table 9: Possible intervals of signal reflection and definitions of experiment parameter

Parameter	Min Value	Max Value
Common (SEA1 / SEA2&3)		
Azimuth	85°	130°
Sin(Elevation)	0.38 / 0.27	0.7 / 0.55
SEA1		
Azimuth	130°	200°
Sin(Elevation)	0.15	0.65
SEA2		
Azimuth	125°	200°
Sin(Elevation)	0.15	0.65
SEA3		
Azimuth	125°	200°
Sin(Elevation)	0.1	0.65

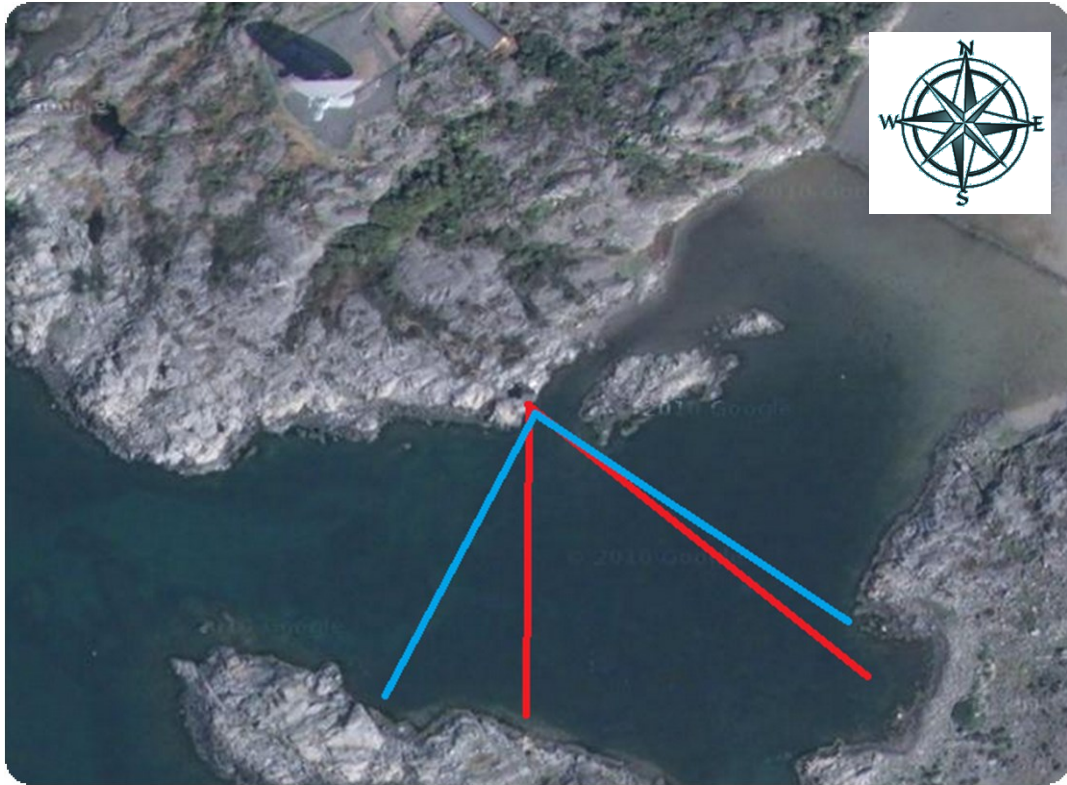


Figure 60: Antennas main reflection zones

Lastly, a constraint regarding time had to be applied: if the timespan in which the data were collected was less than around 30 minutes, the data were being discarded. This was done in order to avoid miscalculation of the height by the software due to the lack of data points and peaks in the LS analysis.

5.4. DATA Acquisition and Pressure Gauges

Various data were collected and stored in order to be able to perform this test campaign. The core data are represented by the actual SNR data acquired by the antenna. These are collected at the rate of 1 Hz and saved in Receiver INdependent EXchange format (RINEX) files by receiver such as the one shown in Figure 61. These data have then to be matched with the position of the satellite in the sky. To do so, broadcasted files have to be load in order to extrapolate the correct azimuth and elevation of each satellite with the respect to the location of the experiment (25 m outdoor antenna dish), summarized in Table 10:

Table 10: Antenna generalized position

	Longitude	Latitude	Height
Value	57.3919883015555°	11.9190013391566°	3.78315601972863 [m]



Figure 61: Acquisition system

Figure 62 shows a possible representation of such data. It is possible to observe the trend of the SNR values for each satellite with respect to time. Various colors are used to distinguish various satellites. Every set of data resemble the shape of an arc ascending or descending with respect to the motion of the satellite in the sky. A rising satellite would generate a signal that will be increasingly enhanced by the antenna gain, while when descending the outcome will be the opposite. The peak power is usually reached around 52 dB and the lowest around 28 dB. As shown, the presence of satellite over the location is generally spread out continuously throughout the day allowing sufficient coverage of the area and enough data to ensure a dense set of measurement.

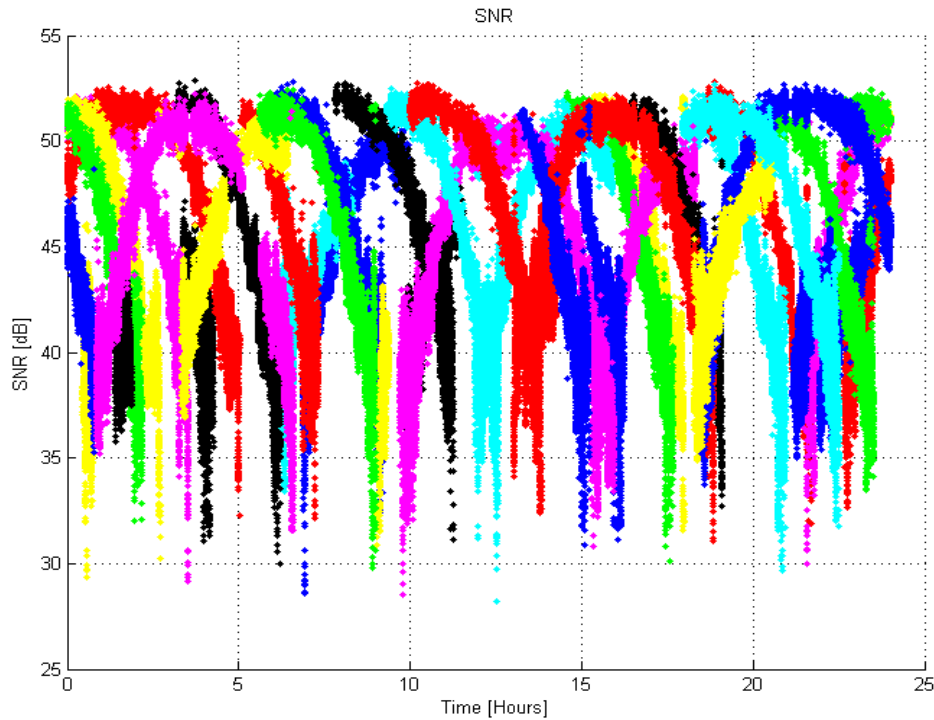


Figure 62: Visible Satellites with respect to time (one day)

Further in the analysis of the sea level, data collected at the observatory will be used to observe if and how weather conditions affect the experiment. These data can be found at <http://wx.oso.chalmers.se/>, downloadable as log files. In addition, three pressure gauges are present near the site of the antennas to perform more accurate measurements of the sea tide. As can be seen in Figure 63 for part of the year the data are not available. In this case a comparison with other tide gauges is necessary to be accomplished. Other two locations near the observatory are provided with tide gauges: one is in Gothenburg and the other in Ringhals, at north and south of Onsala, respectively. Figure 64 shows the respective position of the three locations.

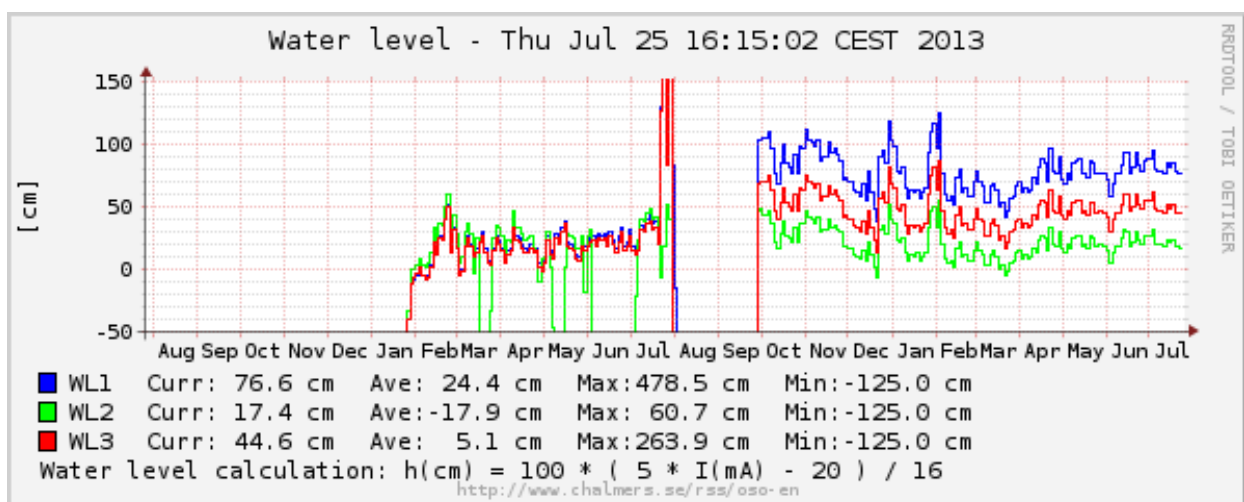


Figure 63: Pressure gauges measurements on a timespan of 2 years

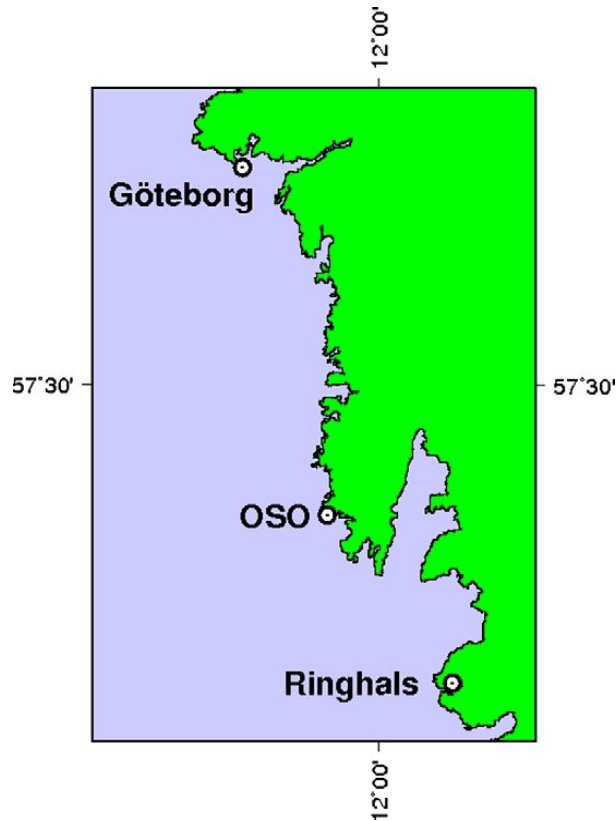


Figure 64: Sites of the three tide gauges (Löfgren et al., 2010)

In order to achieve a valid estimate of the sea level during the missing days, a least square analysis has to be performed. This is actuated using the acquired data at Onsala from day 273 to day 365 of 2012 and combining them with the data from the other locations. Thanks to the built-in MATLAB function *lsq* it is possible to determine a linear relation between the three sources of data, as shown in Equation 22:

$$ONS(day) = A \cdot GTB(day) + B \cdot RIN(day) + C$$

Equation 22: Relation between tide gauges locate at Onsala, Gothenburg and Ringhals

This can be rewritten as:

$$\begin{bmatrix} ONS(273) \\ \vdots \\ ONS(365) \end{bmatrix} = \begin{bmatrix} GTB(273) & RIN(273) & 1 \\ \vdots & \vdots & \vdots \\ GTB(365) & RIN(365) & 1 \end{bmatrix} \cdot \begin{bmatrix} A \\ B \\ C \end{bmatrix}$$

Equation 23: Matrix scheme of the relations between the tide gauges

Introducing the first two matrixes into the function, this produces the coefficients that had better generate the relation between the data. These factors, presented in Table 10, can then be multiplied to the values from Gothenburg and Ringhals in those days when there is no data from Onsala, as shown in the example of Figure 65.

Table 11: Least Square Analysis results

Parameter	Value
A	$4.8039511 \cdot 10^{-1}$
B	$5.5963136 \cdot 10^{-1}$
C	$-1.4860978 \cdot 10^{-4}$
Estimated standard errors of A	$1.7993801 \cdot 10^{-3}$
Estimated standard errors of B	$1.9867500 \cdot 10^{-3}$
Estimated standard errors of C	$9.5075969 \cdot 10^{-5}$
Mean squared error	$1.2097434 \cdot 10^{-4}$

The table also shows the estimated standard errors of the estimator. These are a measure of the accuracy of the function. Lastly, the mean squared error presented indicates the mean discrepancy between the input data and the solution given by the LSA approach. All these values are obtained combining almost 100 days of data. It is also possible to perform the calculation on a daily basis to observe the performance of the procedure. Table 12 presents typical results generated by the program. As shown, the standard errors tend to increase due to the highly reduced number of data that the function can handle to extrapolate the coefficients. On the other hand the MSE is decreased because having less data allows to have a more specific curve that resemble their relation each this standalone case. It is also interesting to observe the relation between the wind velocity and the SE depicted in Figure 66. Bear in mind that the MSE and the SE for the known term are multiplied by a factor 10 to enhance their visibility. It appears that high wind speed is related to increasing uncertainty in the calculation of the data, due to the rapid variation of the value given as input.

Table 12: Example of parameter generated via LSA on a daily basis

Parameter	Value
Estimated standard errors of A	$2.7288512 \cdot 10^{-2}$
Estimated standard errors of B	$2.5357098 \cdot 10^{-2}$
Estimated standard errors of C	$8.1115585 \cdot 10^{-4}$
Mean squared error	$9.4640468 \cdot 10^{-5}$

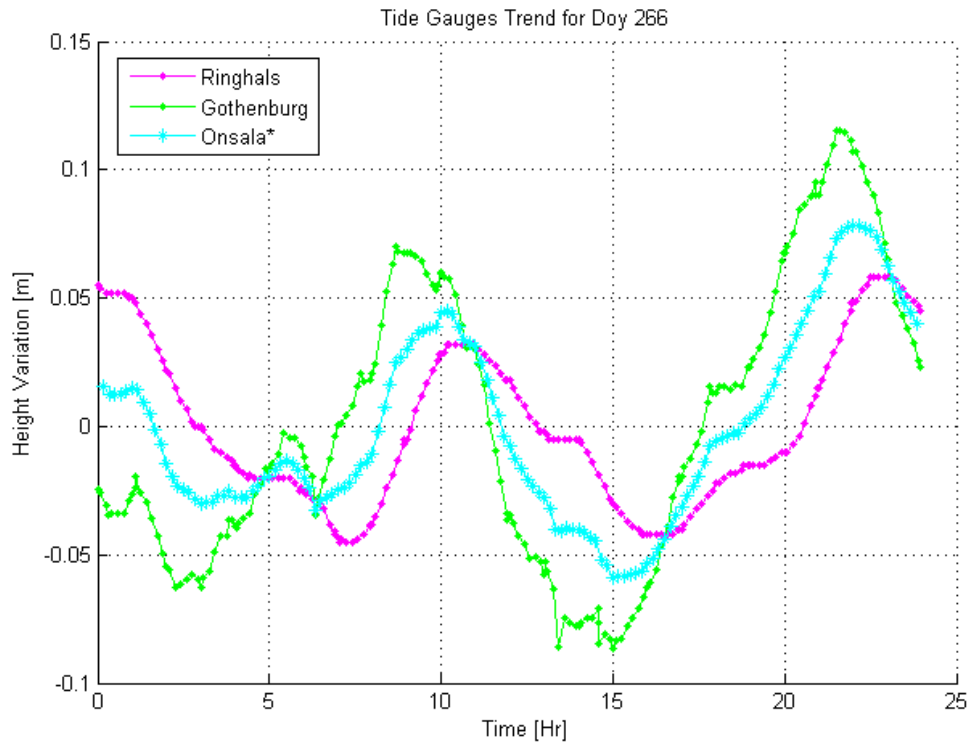


Figure 65: Height variation obtained from Gothenburg and Ringhals tide gauges with the simulated variation at Onsala

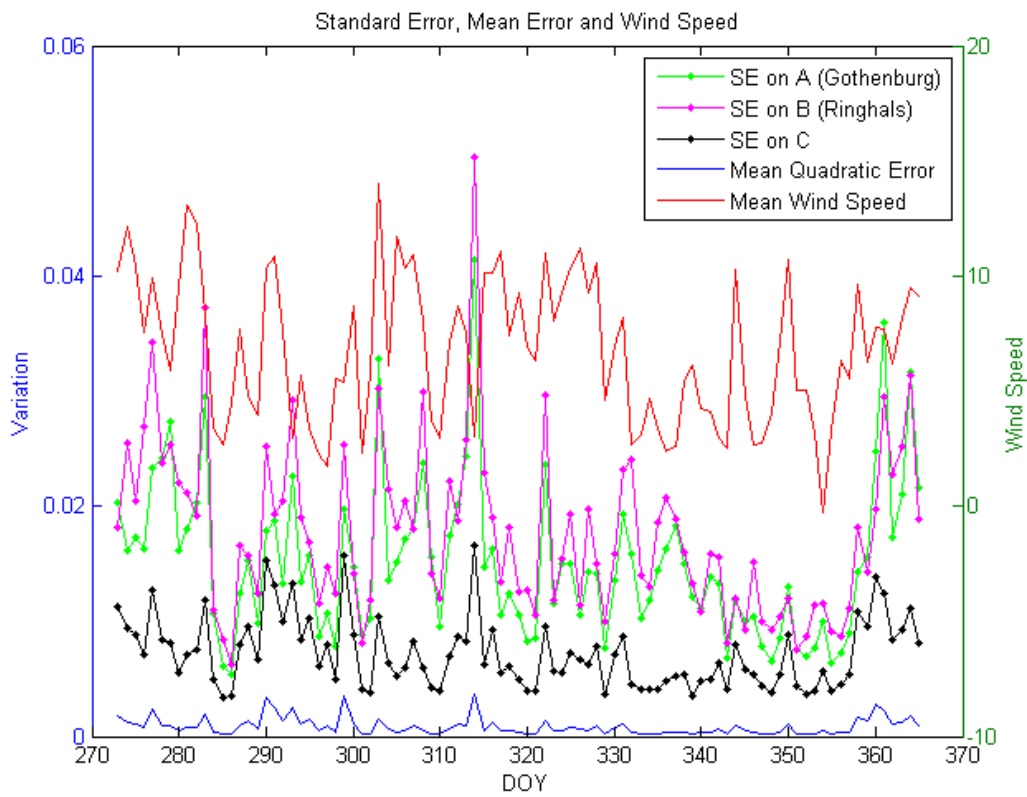


Figure 66: Error parameters and Wind Speed

5.5. Software and Procedure

The analysis was carried out using MATLAB and following the procedure depicted in Figure 70. Most of the procedures were made *ad hoc* and only a small part of them were taken from the online database at <http://www.mathworks.com/matlabcentral/>. The main script was used to impose the *day* or *day of year* observed in the analysis and to choose the antennas examined. Every operation was lately distributed to other scripts or functions in order to separate the various area of the elaboration. The first step was to load the data saved in ASCII format (Already converted from RINEX format). As shown in Figure 70 (A), the data to be loaded consisted in two different files: one contained the position of the satellite, firstly provided in .sp3 format and later in .bdc format, while the other contained the actual SNR data saved in .GS1 format. The former set of data was divided in two variables, one containing the azimuth and the other containing the elevation. All these three variables were containing the data for all the satellites of one day for the relative antenna, as shown in the graph on the right side. Once again, the time interval between two data points was of 1 second (sampling frequency of 1Hz). In this context, the due correction for the current location was applied using three geodetic coordinates as shown in Table 13 (equal to Table 10):

Table 13: Geodetic Position of the Antennas

Parameter	Longitude [°]	Latitude [°]	Height [m]
Value	57.391988301555521	11.919001339156573	3.7831560197286308

Afterward, the constraints on the coordinates were applied in order to process only the data that could contain useful information as depicted in Figure 70 (B). Table 14 sums up the relative value for each antenna within the main azimuth interval. These were deduced primarily from geometrical relation explained in 5.3 and then they were refined by looking at the results from the analysis. They refer to the mean azimuth value, hence slightly modified intervals are utilized. As explained before, the different position between SEA1 and the other two antennas permitted to widen the azimuth interval of the smaller antennas. For obvious reasons a minimum elevation angle was set. Firstly, because it was physically impossible to detect signals from satellites below 0° Elevation (below the horizon). Secondly, because for angle at low elevation the signal is usually disturbed by far objects. In fact, the signal resulted too disturbed to be utilized in the analysis. A typical trend for SNR is depicted in Figure 67. In the same figure the elevation behavior is shown as a blue line in order to easily visualize the valid interval of SNR value. The black segment represents the lower elevation allowed as valid. Figure 68 represents instead the trend for the relative azimuth angle. Combining these two graphs it is possible to

detect the arc that can be used for the analysis. It is interesting to see that the satellite usually swipes the interested area almost twice a day. This provides constant coverage and consistency on the measurements.

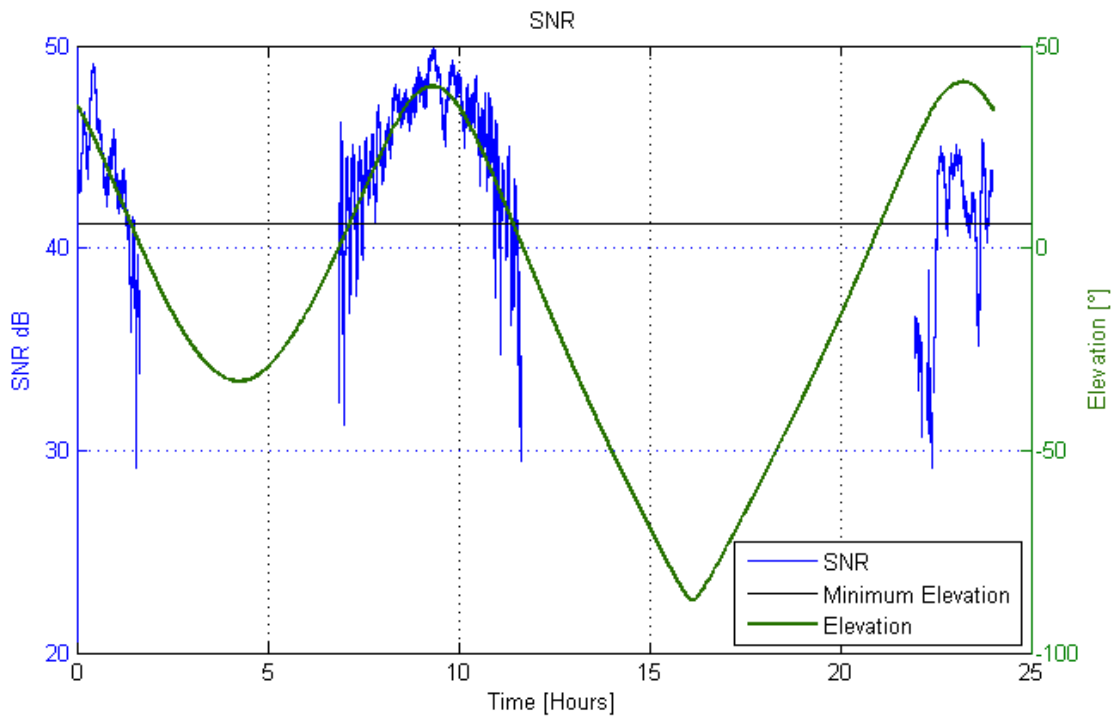


Figure 67: SNR and Elevation trend during a one day timespan

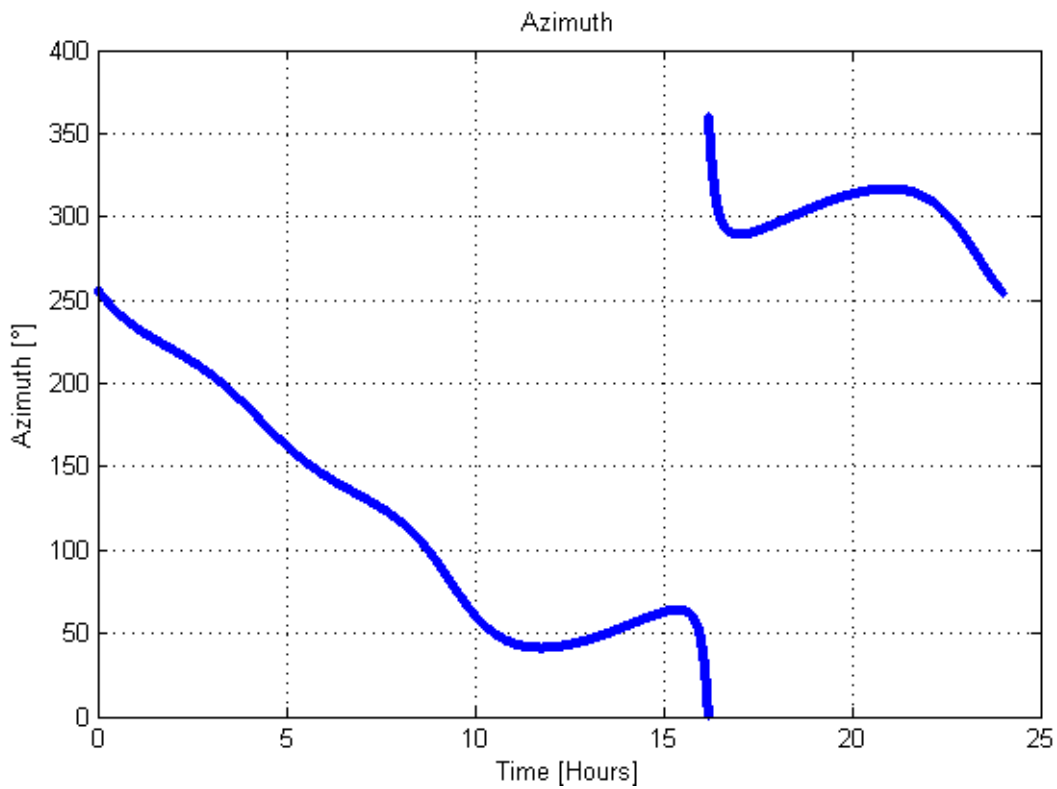


Figure 68: Azimuth angle variation during a one day timespan

Table 14: Antenna parameters and constraints

Parameter	SEA 1	SEA 2	SEA 3
Minimum Azimuth [°]	130	125	125
Maximum Azimuth [°]	200	200	200
Minimum Elevation [°]	6		

The first subscript, *Critical_Point.m*, had the task to detect and store the critical points of the SNR. These consist in all the point of positive peaks, and the starting points of every valid arc. This means of every sequence of points inside the azimuth mask and above the elevation minimum angle. In this way, it was possible to quickly detect starting and ending point for every segment. The second subscript, *DivisionSTRUCT.m*, divided and saved the single arcs. This was done by initially checking the quality of each segment. Every interval delimited by a subsequent couple of critical point was singularly analyzed. The first parameter was the actual existence of data for the *doy* loaded. If so, the interval observed was being registered at elevation and azimuth angles accepted by the specifications in Table 14. In addition, the interval timespan was calculated, which has to be above 30 minutes to be registered as valid. Finally, the set was checked in order for it to contain data and not empty values. This can happen when the antenna-receiver system has been turned on only for part of the day. An example of the segment stored can be seen in Figure 69:

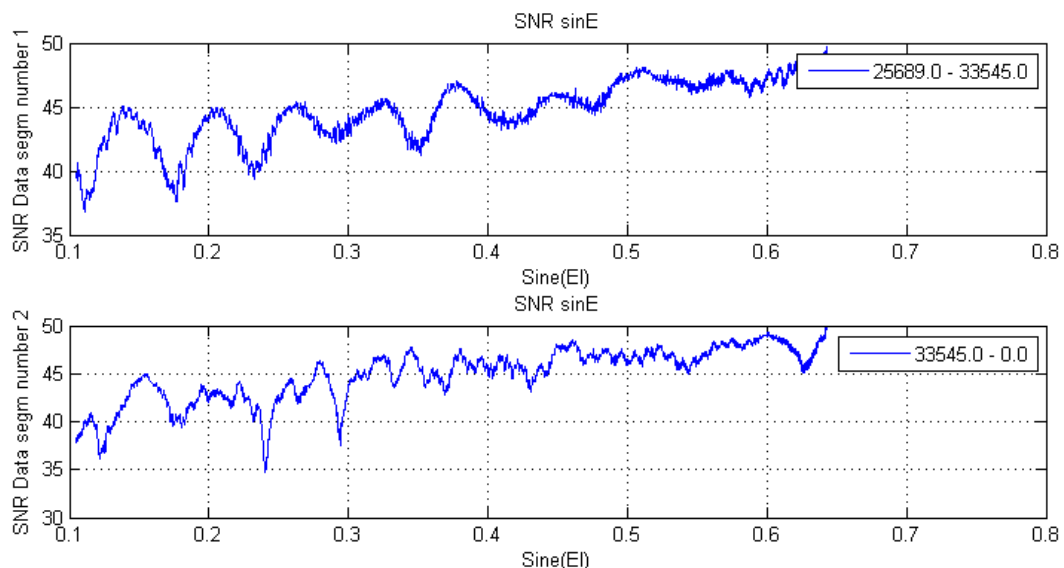


Figure 69: Typical segment obtained by the raw SNR data with respect to the SINE of elevation

As shown, the arcs present a high grade of noise and fluctuations. As shown in Figure 70 (B), in order to facilitate the processing of these data, they were smoothed using the built in MATLAB function

smooth.m. In this case the averaging span was constituted by 20 data points and produced signals as the one presented in the second graph on the right side of figure B. On the same script the data were detrended and brought to linear scale as the example on the third graph. At this point, the actual height calculation was taking place. Each arc was divided into two different segments in order to provide more results and have a higher time resolution. On the other hand, this brought to a reduction into the single timespan for each segment analyzed. The criteria used to divide the segments are provided in Table 15.

Table 15: Height calculation constraints (main azimuth interval)

Parameter	SEA1	SEA2	SEA3
Minimum Ant.Height [m]	1.9	1	0.7
Minimum Elev. (1) [°]	0.15	0.15	0.1
Maximum Elev. (1) [°]	0.55	0.5	0.55
Minimum Elev. (2) [°]	0	0.35	0.35
Maximum Elev. (2) [°]	0	0.65	0.65
Peak Relevance (Savransky)	0.6	0.6	0.6
Peak Relevance (Saragiotis)	0.7	0.7	0.7
Significance Threshold	0.9	0.9	0.9
Width of Peak [m]	0.45	0.45	0.45

The minimum antenna height was imposed in order to establish a minimum possible height of the antenna below which any result would have been stated as due to errors in the procedure. The elevations represent the start and ending points on the analysis of the data. As shown, the only variation can be noted on the minimum elevation of the first segment of SEA3. This was done because this antenna was supposed to acquire better the reflection signals at low elevation. Once the data string were adjusted to this parameter, the shrunk, detrended and smoothed arc was inserted into the Lomb function as schematized in Figure 70 (C). As explained in 4.4, the resulting output was showing a series of peaks, related to the possible height of the reflecting surface. At this point, the remaining parameters of Table 15 were used to refine the calculation. *Peak Relevance* (Savransky and Saragiotis) were used by the program to detect possible peaks other than the one used to calculate the height. As schematized, the program checks whether there are peaks higher than a percentage of the highest peak. If this happened, the analysis cannot be ensured to be accurate and the data are discarded. Similarly, the significance threshold checks that the grade of statistical significance is above a certain value. The last constraint consisted in the calculation of the width of the peak at its half magnitude. If this was smaller

than the chosen value, the related height was supposed to be statistically relevant. Otherwise the spread of the peak over a wide interval of the height made the calculation of the height too imprecise. All of these three parameters are related to the Lomb-Scargle analysis and they consist in 3 flags. The height was stored only if all of these three factors are satisfied. Moreover, the script used was performing further elaboration in case of the failing of one of this parameter. When this happened, the program was trying to widen the interval of data in order to increase the number of point used in the analysis. This brought a loss in time resolution but also the chance of having a valid result.

After the calculation of the height was completed, the main script was saving the height in an ASCII file along with mean elevation, time of the day, mean azimuth and other parameters related to the segment utilized. This was done in order to be able to load the data in a second moment. Moreover, the script allowed to load partial data and complete the analysis on the day specified without repeating the whole calculation.

At the end of the height calculation the comparison of the data was carried out. To do so, weather data (<http://wx.oso.chalmers.se/>) were also loaded. In particular, the effect of rain and wind was evaluated in order to observe a possible relation to the signal reflection.

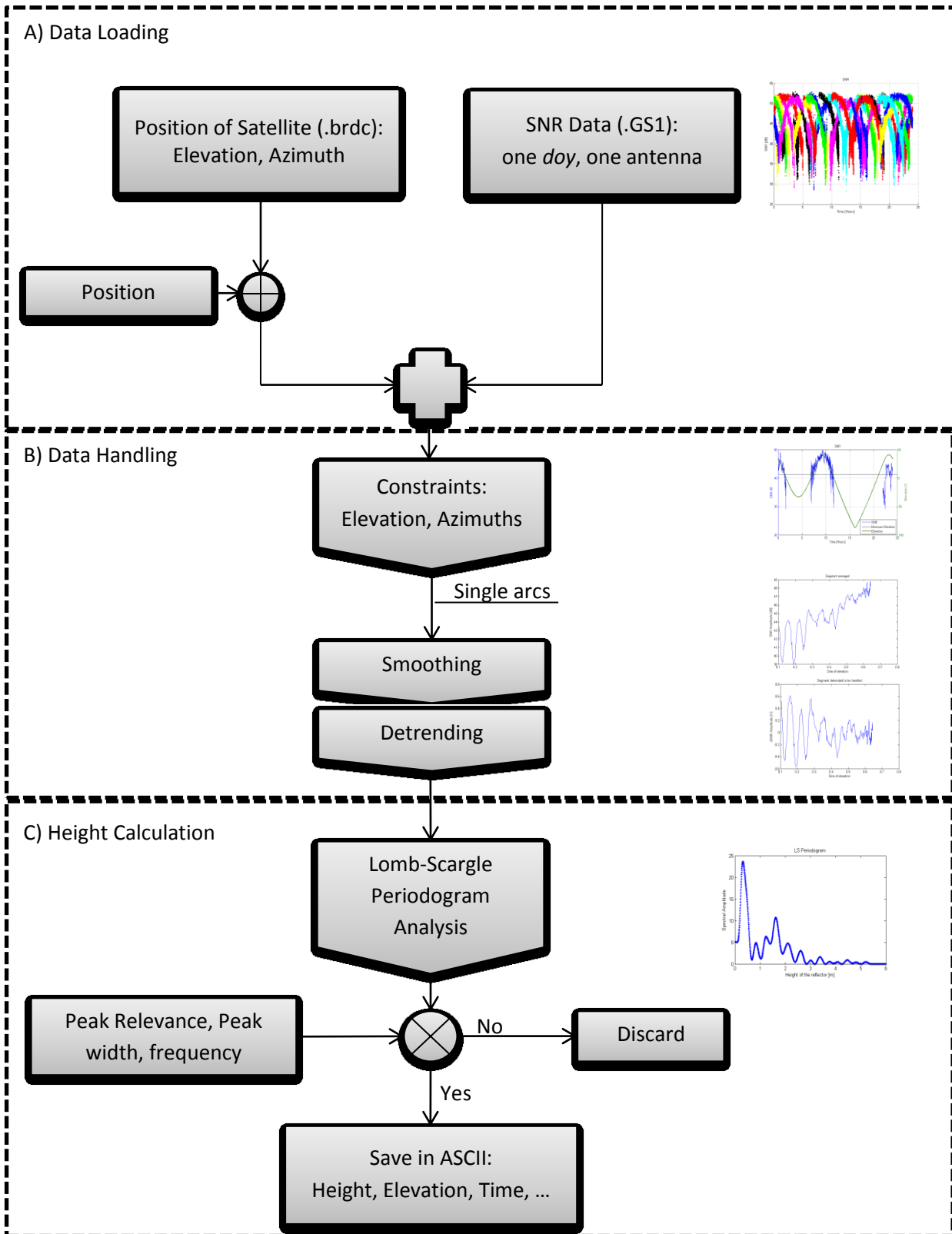


Figure 70: Block scheme for height calculation

5.6. Results

In this section the results will be presented, lately discussed in 5.7. Firstly, the output of the program will be shown only for one day, as an example of the program output. This type of output was used to observe the data collected by the antenna and fix the parameter for the height calculation. As presented in Figure 71, each calculated height was tagged with satellite number, mean azimuth angle, mean elevation angle, duration of the SNR interval (only presented for one antenna in the figure). In addition, it was possible to impose a routine using the script *sortH.m* in order to discard height solutions that were exceeding an empiric threshold. In other words, for standard deviation above 30 cm, the points with a distance from the mean of $std/2$ were discarded.

The figure presents the three sets of data collected by the configurations: red for SEA1, blues for SEA2 and black for SEA3. In the graph are also present the synthetic one (Onsala obtained as in 5.4, in light blue), the wind speed (purple) and the rain rate (yellow) to facilitate the detection of possible interactions.

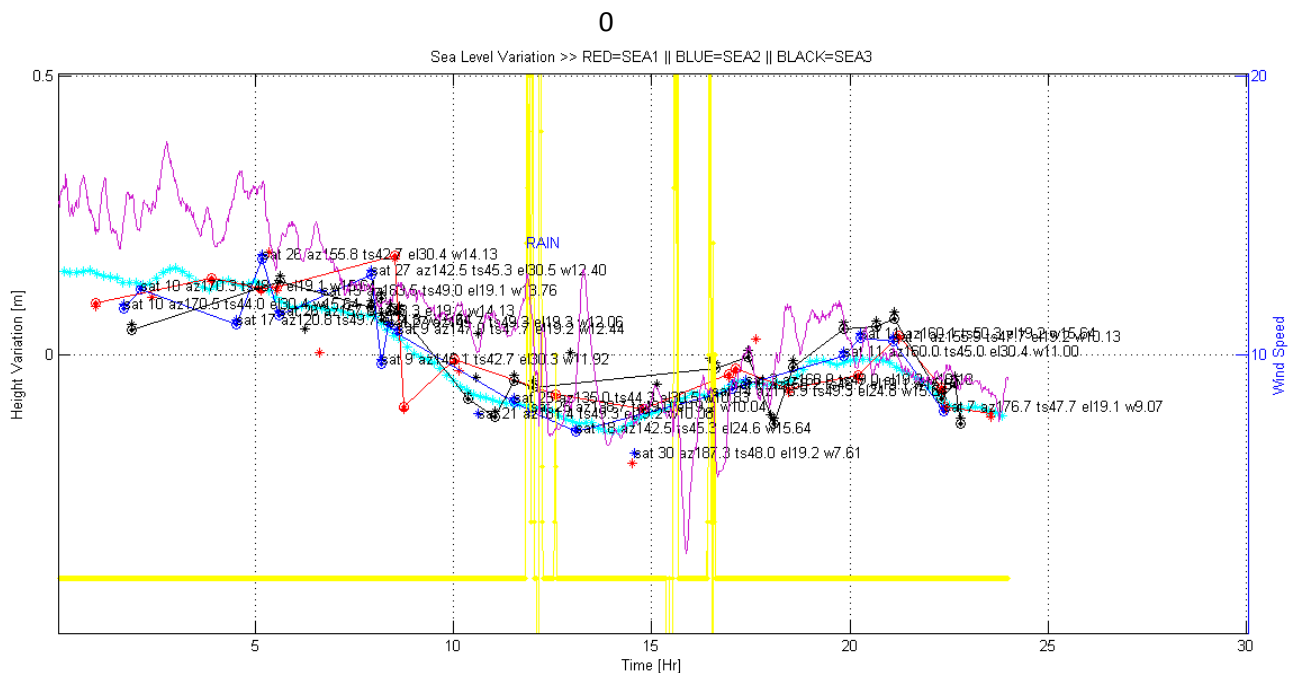


Figure 71: Result for one day all satellites data analysis (DOY 264)

5.6.1. Sea level variation

For further analysis, larger sequences of days were used together to generate a continuous solution, as shown in the following figures. This allows to obtain a more reliable statistical analysis and better fitting of the data when they were averaged. In this case, rain and wind were taken away and only the synthetic gauge was kept together with the three gauges, for direct visual comparison. The figures show

each antenna separately along with the Gothenburg synthetic gauge for a set of 22 days in Figure 72, Figure 73 and Figure 74 while a set of 8 days is shown in Figure 75, Figure 76 and Figure 77. These series of data, generated through a MATLAB routine, allowed also to perform statistical analysis on the data, producing the results shown in Table 16. The table presents the value for the mean, maximum and minimum values, the root mean square and the correlation factor between antenna data and synthetic gauge along with the standard deviation. The number of points and the length of the interval analyzed are also presented in order to highlight the distribution of points in time.

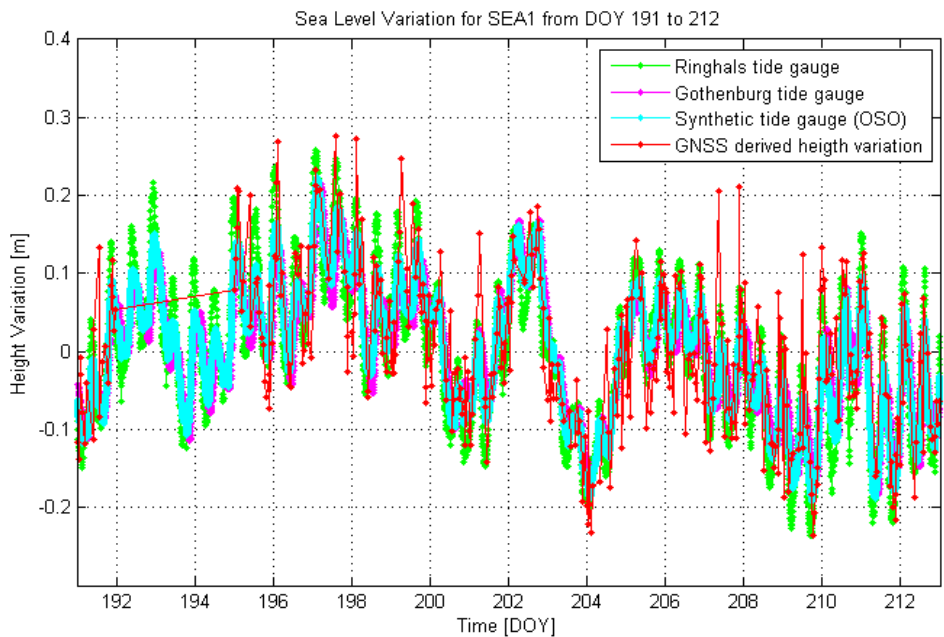


Figure 72: Reflector height resulting from data processing for SEA1 from *day* 191 to 212

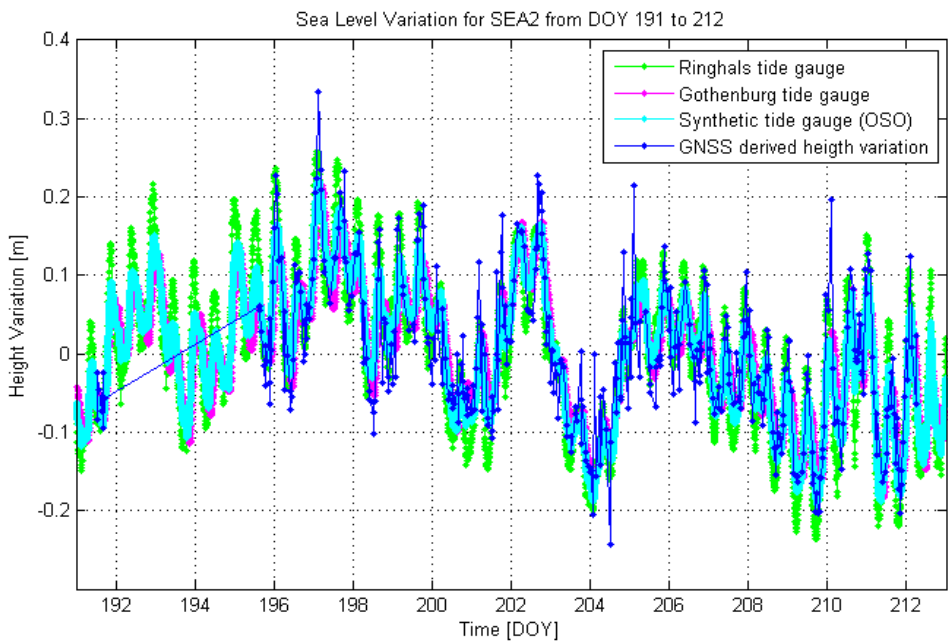


Figure 73: Reflector height resulting from data processing for SEA2 from *day* 191 to 212

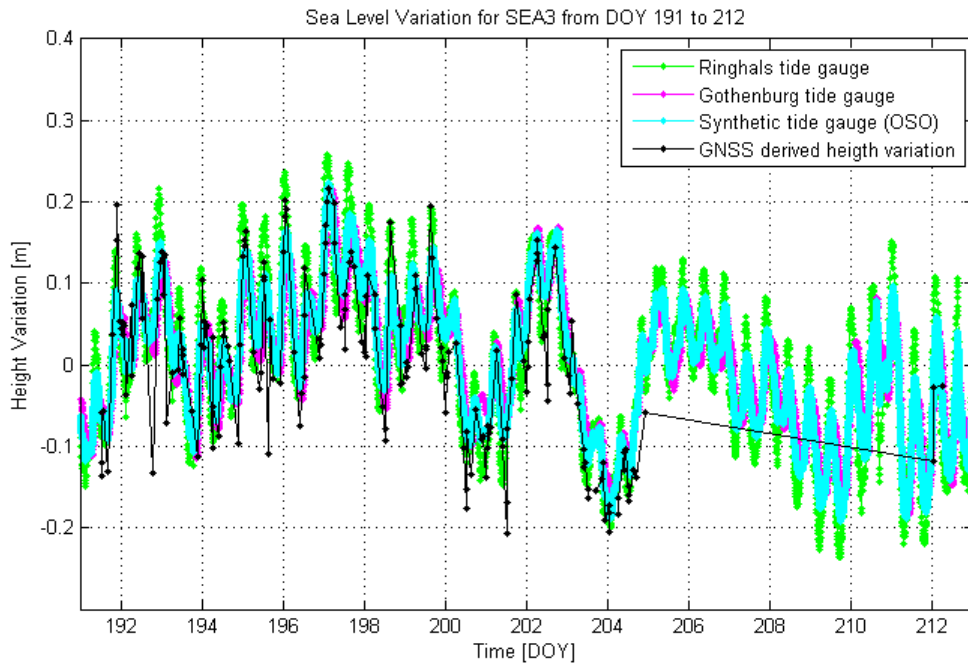


Figure 74: Reflector height resulting from data processing for SEA3 from *day* 191 to 212

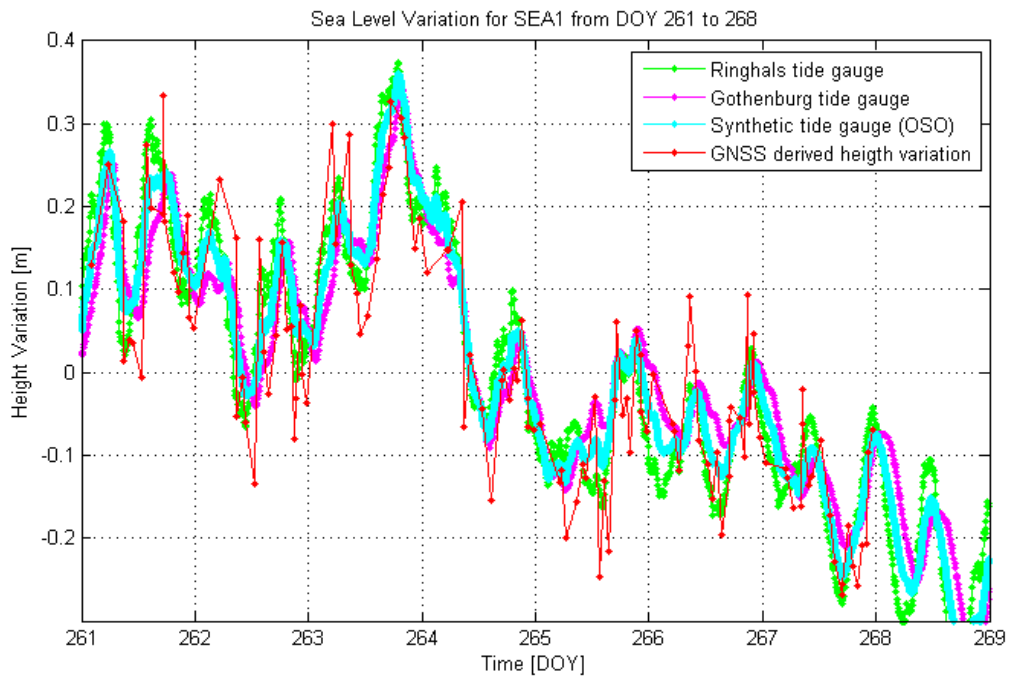


Figure 75: Reflector height resulting from data processing for SEA1 from *day* 261 to 268

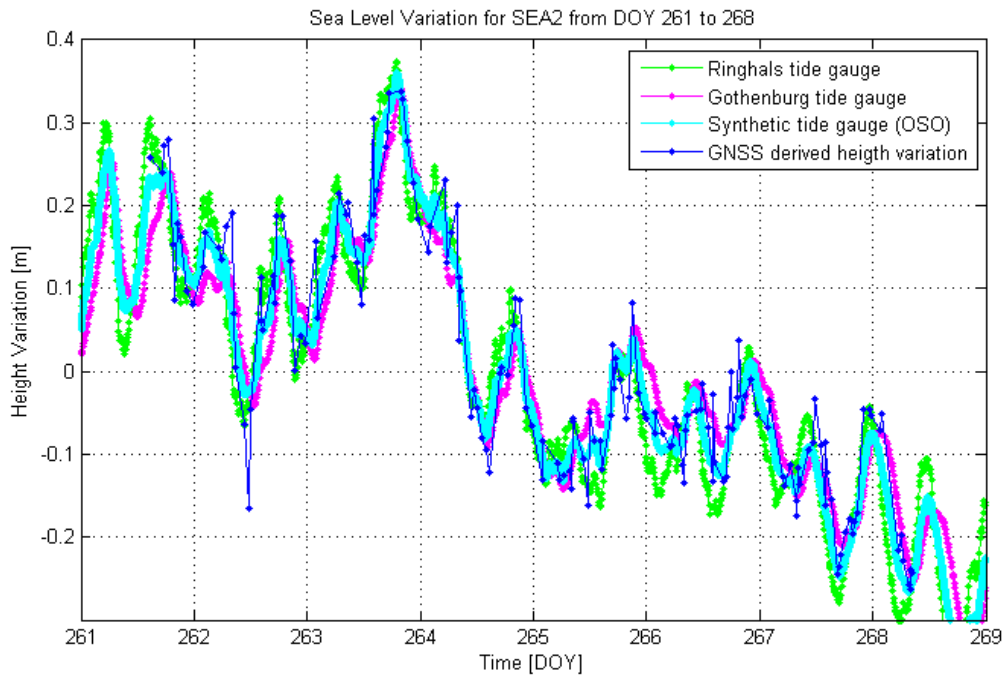


Figure 76: Reflector height resulting from data processing for SEA2 from *day* 261 to 268

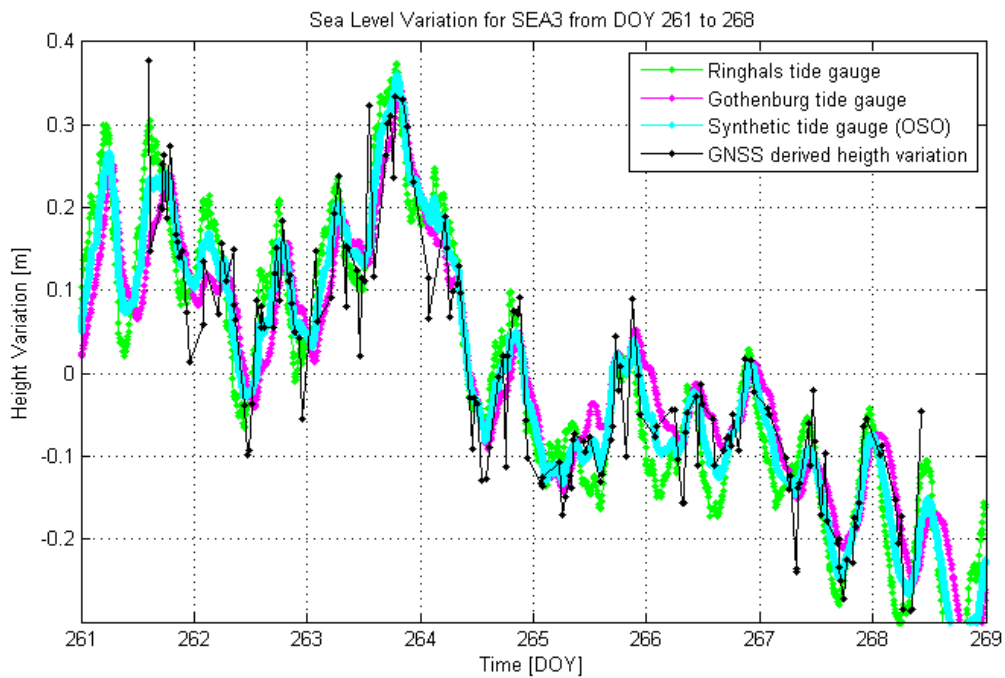


Figure 77: Reflector height resulting from data processing for SEA3 from *day* 261 to 268

Table 16: Statistical results for each antenna

Interval	Parameter	SEA1	SEA2	SEA3
191 to 212	N Points	375	414	287
	Interval Length [DOY]	18.927731	16.764977	13.611736
	Mean [m]	0.002182	0.004574	-0.027078
	Max [m]	0.207939	0.199255	0.117623
	Min [m]	-0.14288	-0.114053	-0.177310
	RMS [m]	0.059006	0.042084	0.048960
	STD [m]	0.059044	0.041885	0.040862
	Correlation Coef.	0.81275	0.896752	0.910659
261 to 268	N Points	131	168	210
	Interval Length [DOY]	6.881644	6.730799	6.832662
	Mean [m]	-0.019175	0.004845	-0.005950
	Max [m]	0.138345	0.123001	0.166973
	Min [m]	-0.153045	-0.142777	-0.164535
	RMS [m]	0.065014	0.037565	0.047516
	STD [m]	0.062361	0.037363	0.047255
	Correlation Coef.	0.898339	0.965511	0.944513

The correlation between the data from the LS analysis and the one taken from the synthetic gauge also can be seen in Figure 78 and Figure 79. In this case, the presence of a relation between the inputs can be seen in all graphs thanks to the mutual linearity of the increment in variation magnitude.

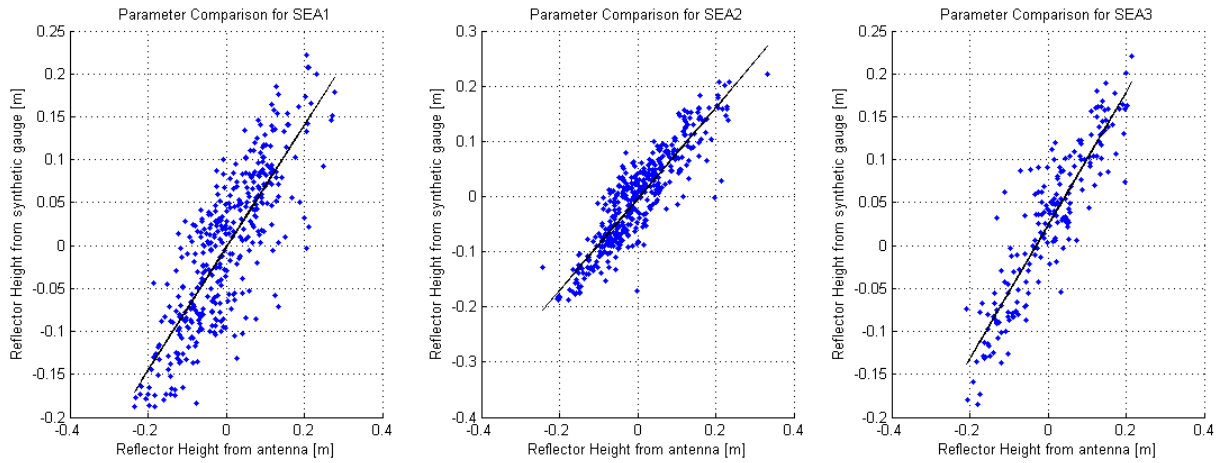


Figure 78: Comparison between antenna height and synthetic height for *day 191 to 212*

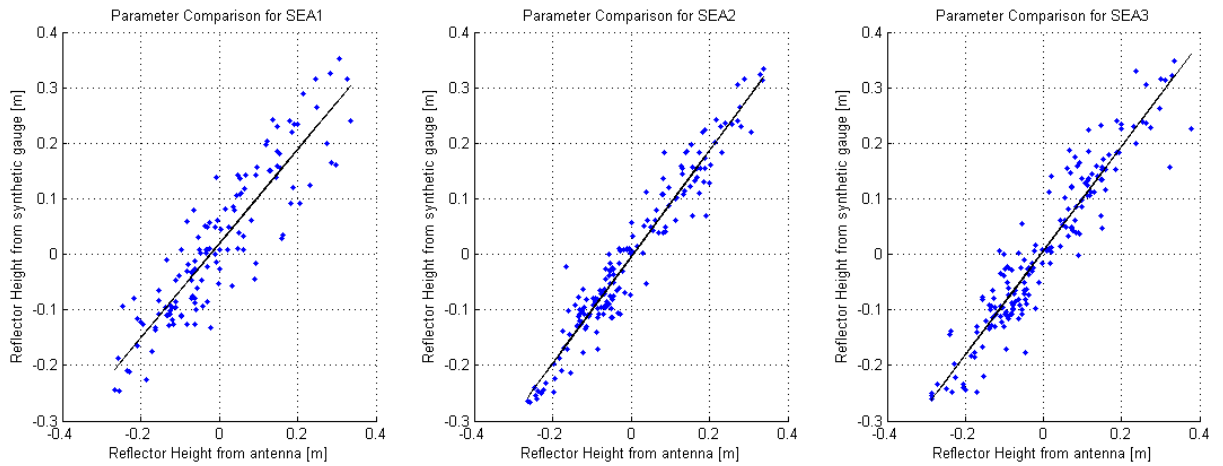


Figure 79: Comparison between antenna height and synthetic height for *day 261 to 268*

5.6.2. Error distribution and statistical parameter variation

As explained in the previous chapter, the environment of the bay constituted a challenging location for the acquisition of reflected signals. Figure 80 and Figure 81 show the error distribution with respect to the azimuth angle (red) and the elevation angle (blue). Once again, the mask allowed a range of azimuth angle from 120 to 200 circa for the small antennas, and from 60 to 200 circa for the choke ring antenna. As can be seen, the data are almost well distributed throughout this range. At the same time, the majority of the data suitable were obtained analyzing signals reaching the earth surface with an elevation angle of circa 20 and 37 degrees.

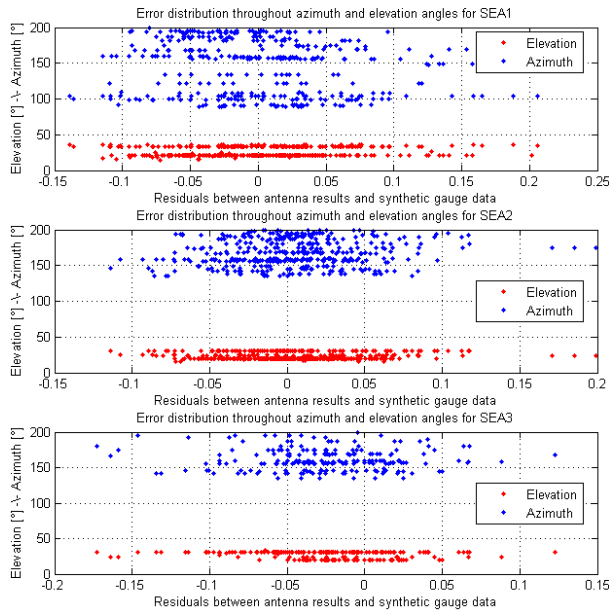


Figure 80: Error distribution with respect to elevation (red) and azimuth (blue) angle from *day* 191 to 212

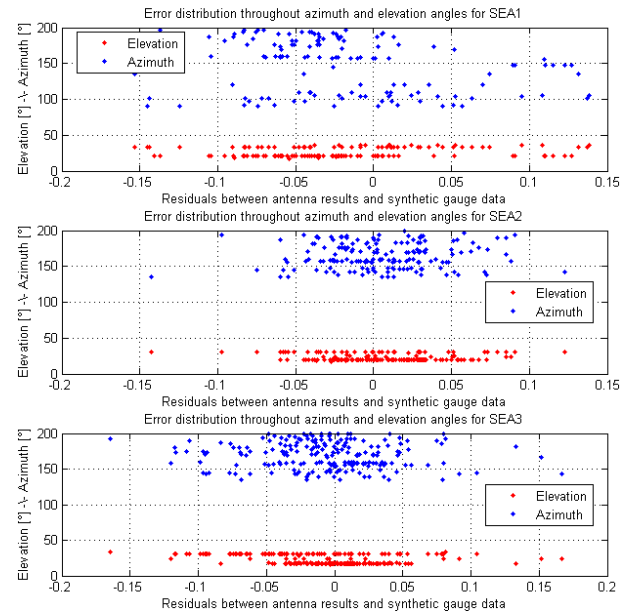


Figure 81: Error distribution with respect to elevation (red) and azimuth (blue) angle from *day* 261 to 268

It was later possible to observe the evolution of the parameter shown in Table 16 with respect to the azimuth interval. The one chosen for the final result presentation was spacing from 85 to 200 degrees of azimuth for SEA1, and from 125 to 200 for the smaller antennas. In Figure 82 and Figure 83 other intervals can be seen, in particular three different values of the upper limit were analyzed. In this way, the most suitable configuration for the height retrievals was investigated, in order to satisfy criteria on accuracy (RMS), correlation, maximal error and time resolution. Even in this case, the two same intervals of days were used. The results shown could not seem to be consistent between the two sets of data but, as also presented in Figure 72, Figure 73 and Figure 74, the longer period was not constituted by the same amount of days for each of the three antennas.

Variation of statistical Parameters with respect to the azimuth interval from day 191 to 212
 RED=SEA1 - BLUE=SEA2 - BLACK=SEA3

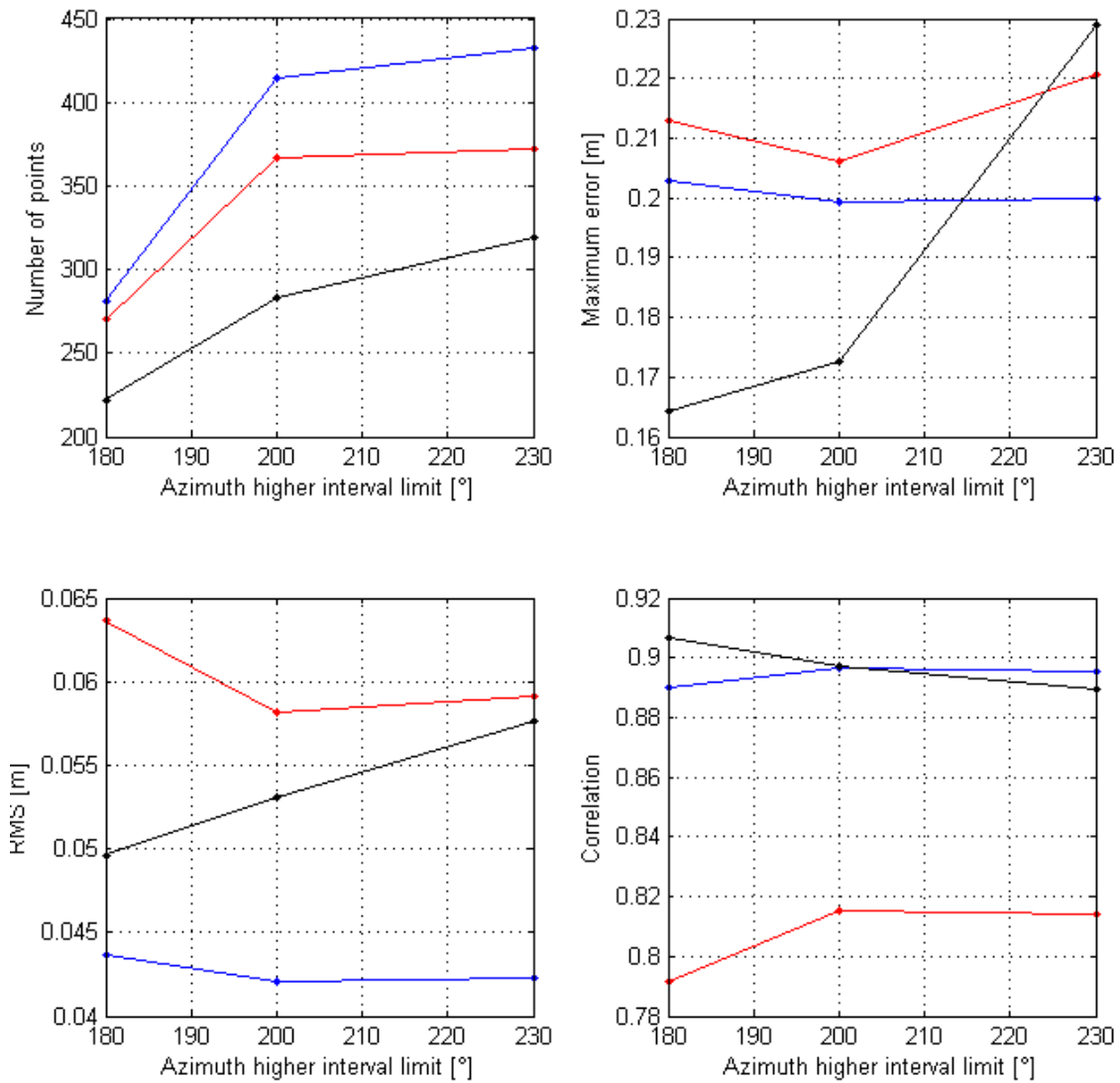


Figure 82: Variation of the statistical parameters with respect to the dimension of the azimuth interval from *day* 191 to 212

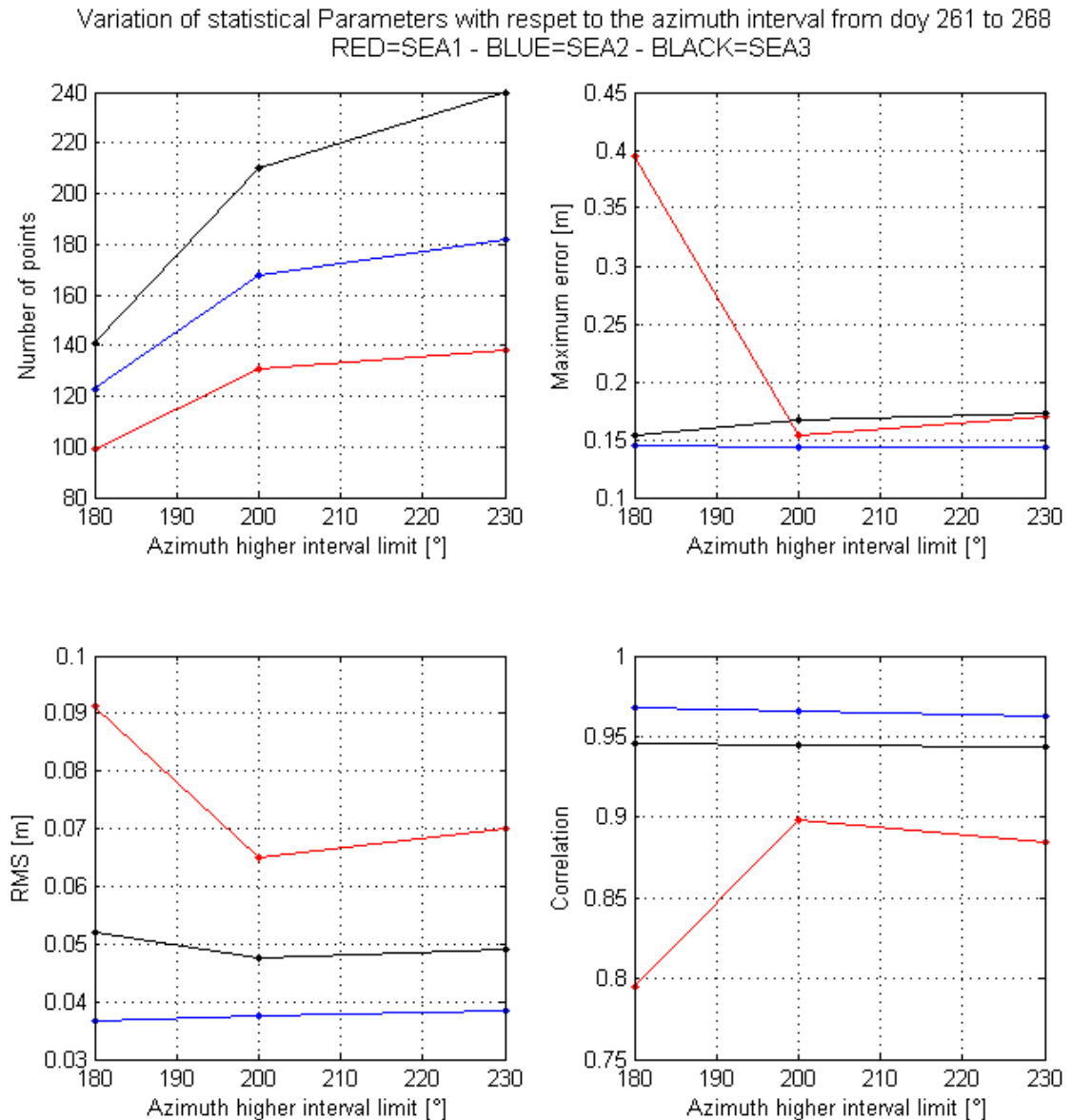


Figure 83: Variation of the statistical parameter with respect to the dimension of the azimuth interval from *day* 261 to 268

In addition, the trend of the sign of the error is presented. Figure 84 and Figure 85 present the ratio of the number of positive errors (i.e. height retrievals above the one from the synthetic gauge) over the quantity of negative errors. This could in part indicate the nature of the error: positive errors could more likely due to detection of rocks and/or islands while negative error could be due to high motility of the sea or just to processing imprecision. Moreover, in Figure 86 and Figure 87 the ratio of the mean negative and positive value with respect to the azimuth interval are presented. These indicate which kind of error contribute more to the diminishing of the accuracy of the model.

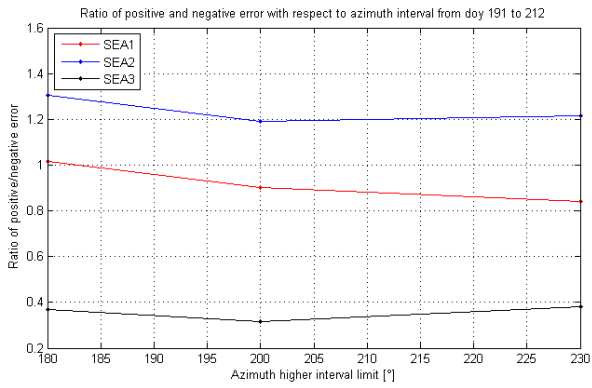


Figure 84: Ratio of negative and positive error with respect to the dimension of the azimuth interval from day 191 to 212

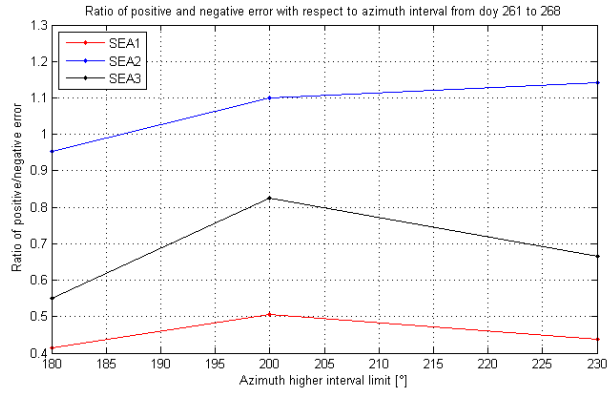


Figure 85: Ratio of negative and positive error with respect to the dimension of the azimuth interval from day 261 to 268

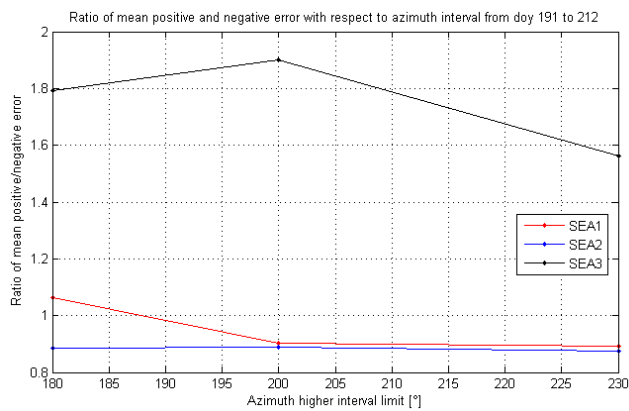


Figure 86: Ratio of mean negative and positive error with respect to the dimension of the azimuth interval from day 191 to 212

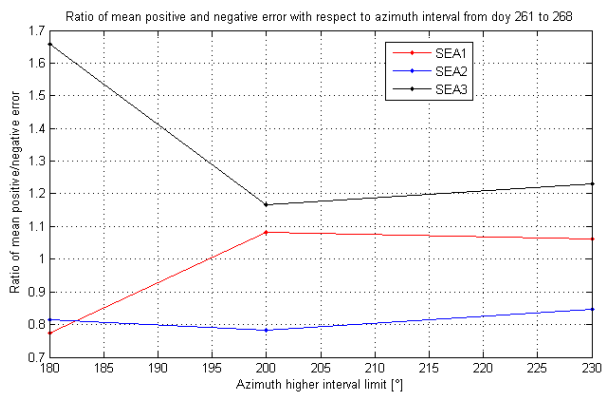


Figure 87: Ratio of mean negative and positive error with respect to the dimension of the azimuth interval from day 261 to 268

5.6.3. Antenna Comparison

In order to investigate the validity of the results, a comparison between the three antennas was carried out. In particular, the offset between one antenna and another was calculated so to observing its variation. In presence of good results, the distance between each couple of antennas should remain constant due to the firm positioning of the two and to the signal coming from the same source at the same time. The data shown in Figure 88 and Figure 89 presents the offset between SEA1 and SEA2 and between SEA2 and SEA3 with red dots. The blue dots represent the relation between the results obtained with each couple. The shapes taken by these data resemble a straight line shifted by a constant value, highlighting the mutual variation of both the antennas accordingly to each other. This correlation between the couples is furthermore shown in Table 17, where the relative coefficients are presented along with other statistical results.

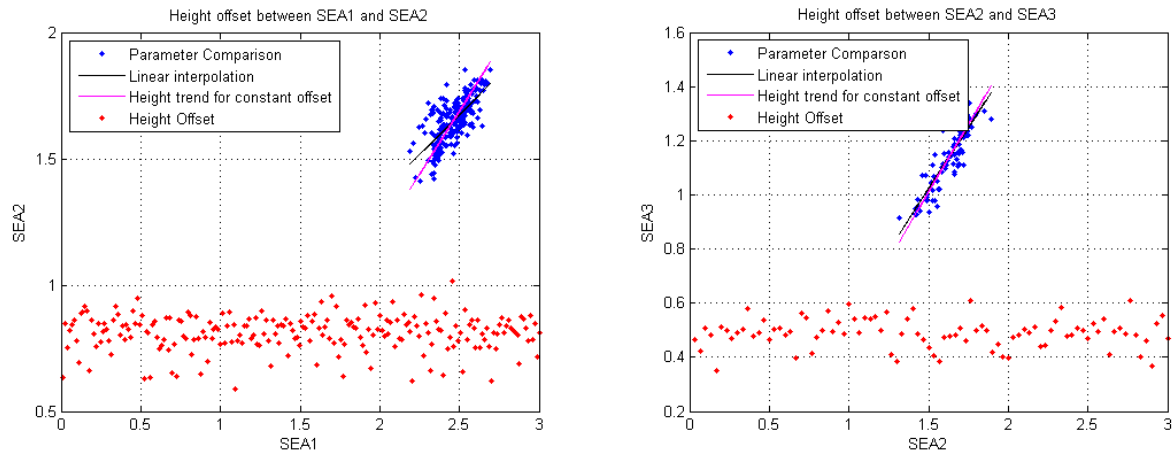


Figure 88: Height offset results from *day 191 to day 212*

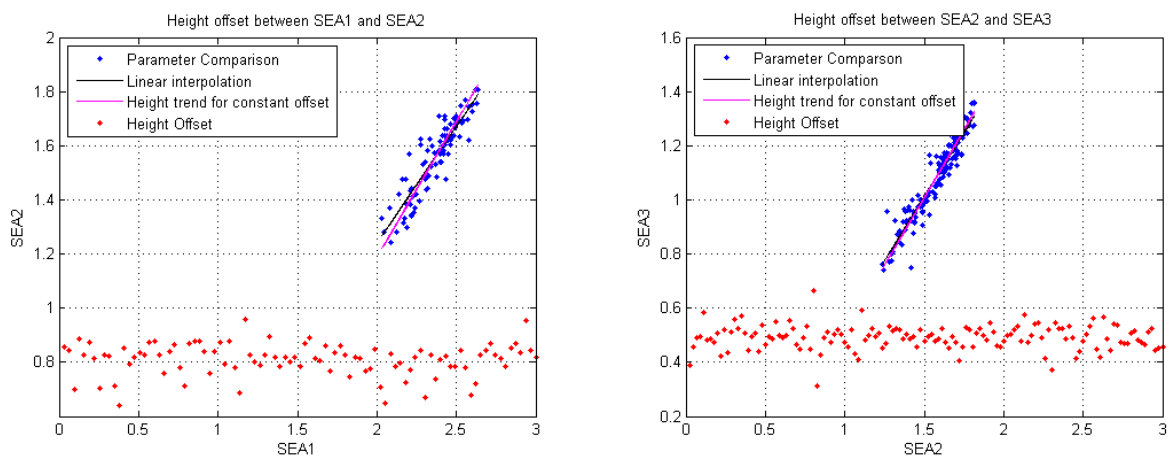


Figure 89: Height offset results from *day 261 to day 268*

Table 17: Statistical results of the antenna comparisons

Parameter	Mean	Max	Min	RMS	STD	Correlation Coef.
191 to 210						
SEA1 - SEA2	0.810945	1.017204	0.588609	0.814062	0.071332	0.715342
SEA2 - SEA3	0.489211	0.611207	0.351824	0.492159	0.05409	0.881262
261 to 268						
SEA1 - SEA2	0.81071	0.957676	0.638674	0.812912	0.06012	0.905131
SEA2 - SEA3	0.492133	0.664546	0.310589	0.494186	0.045156	0.949578

5.6.4. Weather Conditions

Subsequently, the possible interactions with weather conditions were investigated. In particular, the effect of the wind and of the rain was observed. Furthermore, not only the rain rate was analyzed, but also the rain accumulated in the past 1 hour and 24 hours in order to observe a possible rise in the tide, possible effects due to humidity, atmospheric pressure and wind direction variation were also

investigated.

Figure 90 and Figure 91 show the behavior of the offset between the calculated data and the one from the synthetic gauge with respect to the wind speed. As presented, the points are randomly distributed within the interval in terms of wind speed and height difference for all the antennas. This indicates weak relation between this two parameters, also confirmed by the correlation factors shown in Table 18.

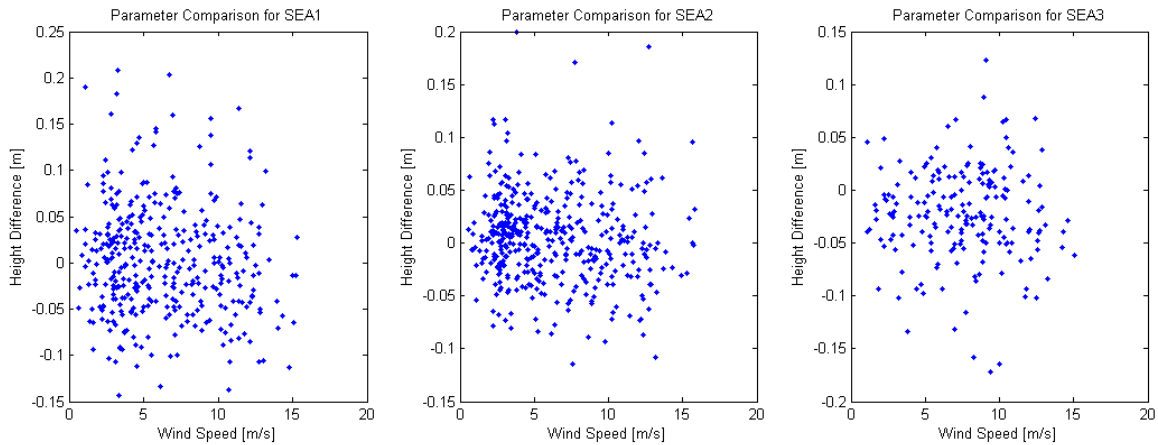


Figure 90: Wind speed interaction results for the three antennas from *day 191 to day 212*

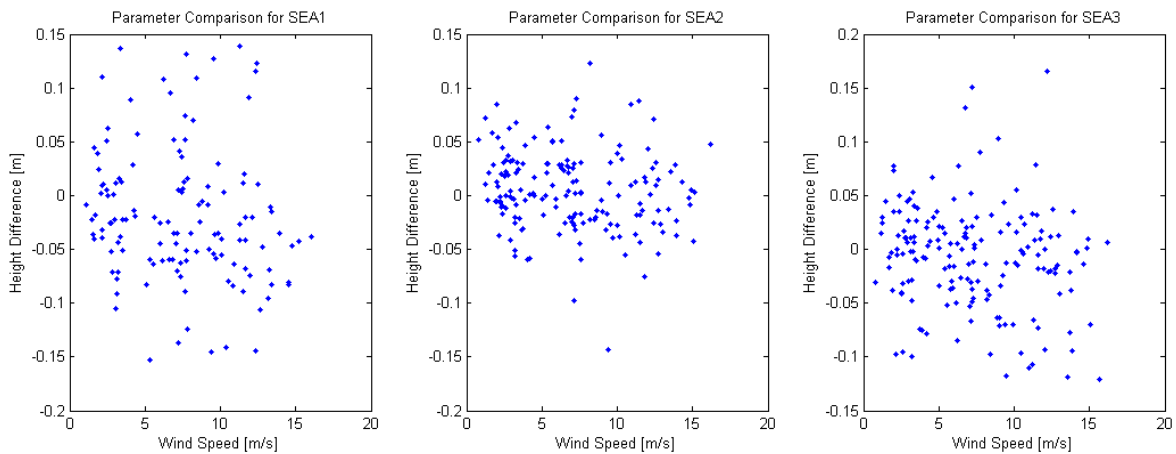


Figure 91: Wind speed interaction results for the three antennas from *day 261 to day 268*

Table 18: Correlation coefficients regarding wind speed effects on height retrievals

Parameter	Interval (DOY)	SEA1	SEA2	SEA3
Correlation Coefficient -WIND SPEED-	191 to 212	-0.110717	-0.090376	0.000441
	261 to 268	-0.15828	-0.139068	-0.166899

Analogous results were obtained when investigating the effect of wind direction, rain, atmospheric pressure and humidity on the height retrievals. In the case of 24 hour rain, there were no data available for the intervals used; the other parameters resumed in Table 19 show similar result to what already

observed for the wind. The figures for these parameters are not presented, resembling very similarly the behavior shown by the wind speed interaction.

Table 19: Correlation coefficients regarding rain effects on height retrievals

Parameter	Interval (DOY)	SEA1	SEA2	SEA3
Correlation Coefficient -WIND DIRECTION-	191 to 212	0.108567	0.090376	0.067338
	261 to 268	0.158280	0.139068	0.151927
Correlation Coefficient -RAIN RATE-	191 to 212	0.097449	0.050701	0.0374014
	261 to 268	0.022272	0.000907	0.036897
Correlation Coefficient -RAIN 1 Hour-	191 to 212	0.098191	0.078096	0.036268
	261 to 268	0.072778	0.054777	0.025706
Correlation Coefficient -PRESSURE Hour-	191 to 212	0.100061	0.002926	0.04664
	261 to 268	0.000552	0.055486	0.037476
Correlation Coefficient -HUMIDITY Hour-	191 to 212	0.046333	-0.001654	0.18467
	261 to 268	0.159194	0.10404	0.098234

An interesting aspect related to the influence of the wind direction can be observed when analyzing the larger errors. Figure 92 and Figure 93 show the distribution of the errors above 0.1 m with respect to the direction of the wind, showing a preferential presence of error for values across 250° (SW). This can be also partially confirmed by the data in Table 20, where the overall incidence of the wind from that particular direction is compared to the incidence on the detection of larger errors.

Table 20: Incidence of wind direction on the detection of larger errors

Interval (DOY)	Errors related to wind directions across 250° (±35)	Errors related to wind directions across 250° (±35) above 0.1 m [%]
191 to 212	48.3	56.6
261 to 268	44.1	65.5

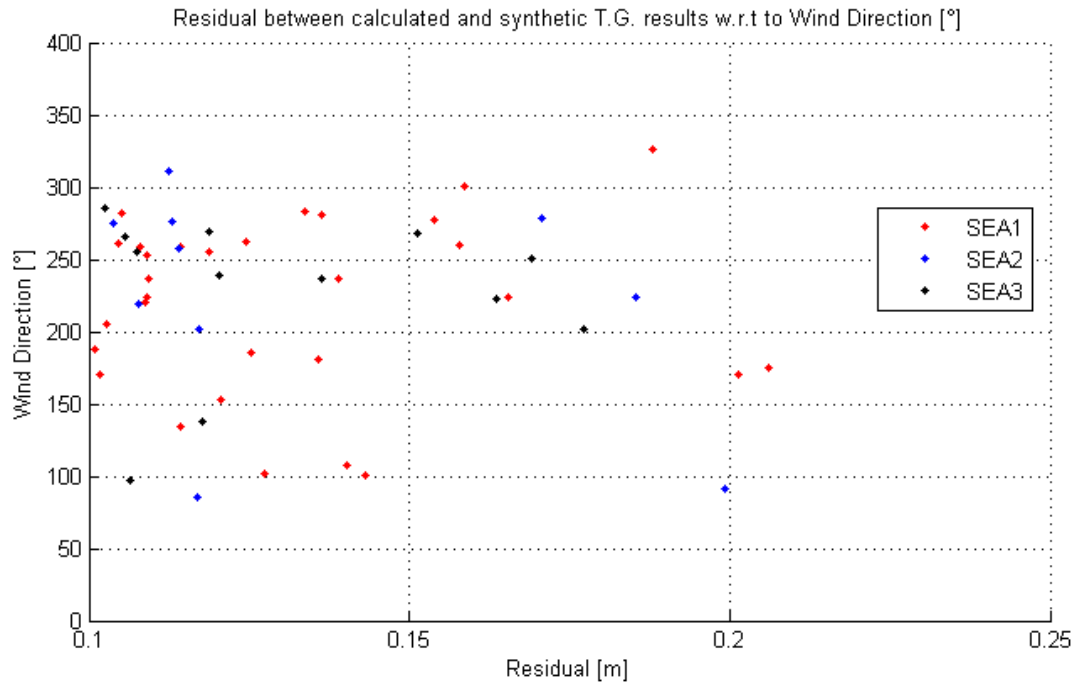


Figure 92: Wind Direction influence on the detection of larger errors for all the antennas from *day 191 to day 212*

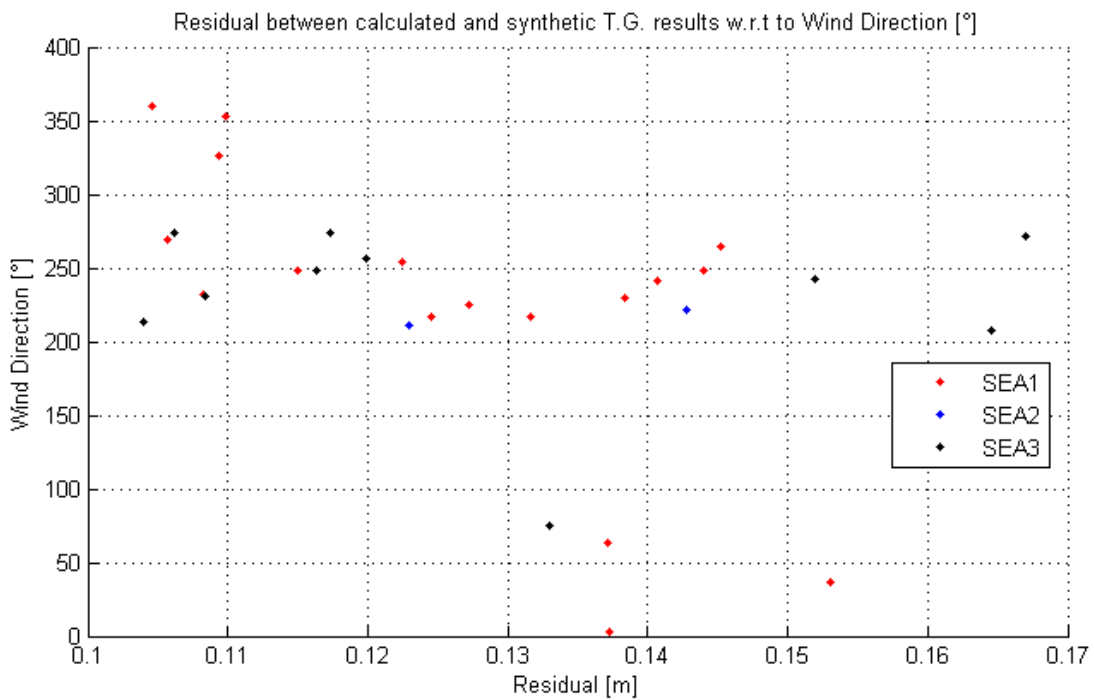


Figure 93: Wind Direction influence on the detection of larger errors for all the antennas from *day 261 to day 268*

5.6.5. Interpolation and smoothing

Due to the length of the arcs required to perform the analysis and to the quality of the signal, by using single antennas it is possible to obtain valuable data points with an average time resolution of 60- 70 minutes. In order to increase the number of points, MATLAB built in function can be used. In particular,

using linear interpolation it has been seen to provide the best results in terms of correlation coefficient and RMS. Table 21 resumes this value, highlighting a degradation on both the parameters for SEA2 and SEA3. Viceversa for SEA1 this behavior is not so strong, probably due to the lack of original data points that led to poor results. As shown in Figure 94, a number of days for all the antennas were not recorder and resulted in false interpolated points. In order to neglect this behavior, only the valid intervals were retained and analyzed, providing the value in brackets in Table 23. The interpolated data for the other interval are also presented in Figure 95.

Table 21: Correlation coefficient and RMS value for interpolated datasets

Interpolation using "linear" method: 600 Points				
		SEA1	SEA2	SEA3
191 to 212	Correlation Coeff.	0.8083 (0.8481)	0.5435 (0.3256)	0.5673 (0.5596)
	RMS	0.05592 (0.05171)	0.08039 (0.10461)	0.08866 (0.08277)
261 to 268	Correlation Coeff.	0.8639	0.6232	0.6402
	RMS	0.07420	0.11967	0.11914

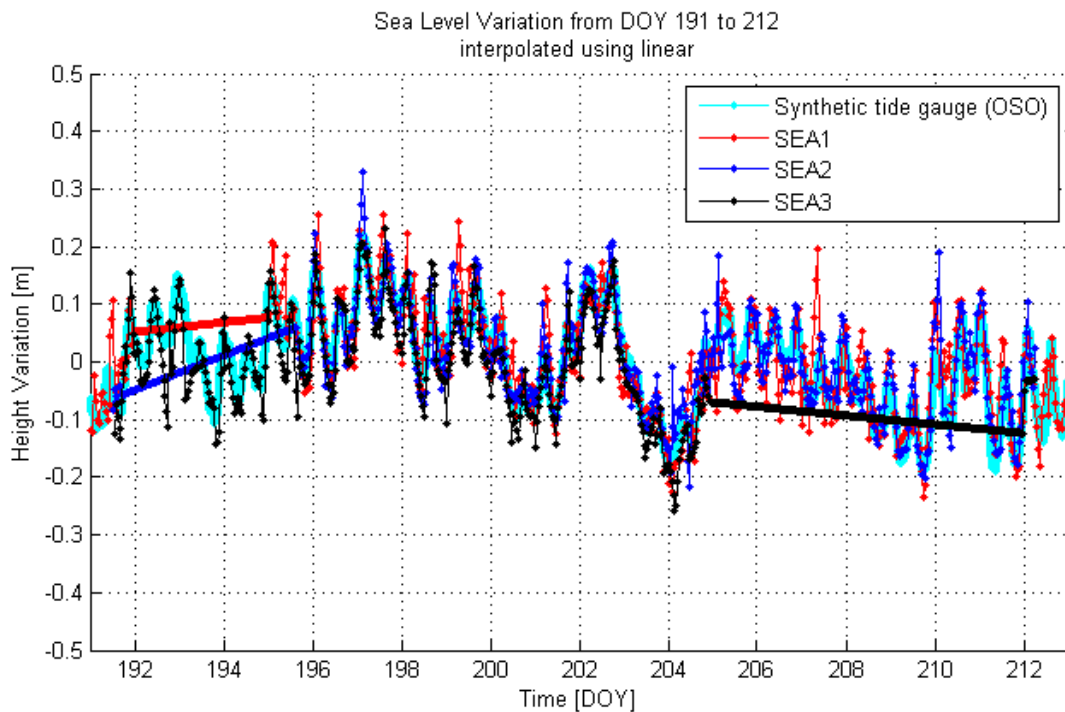


Figure 94: Interpolated (linear method) data for all the antennas from *day* 191 to *day* 212

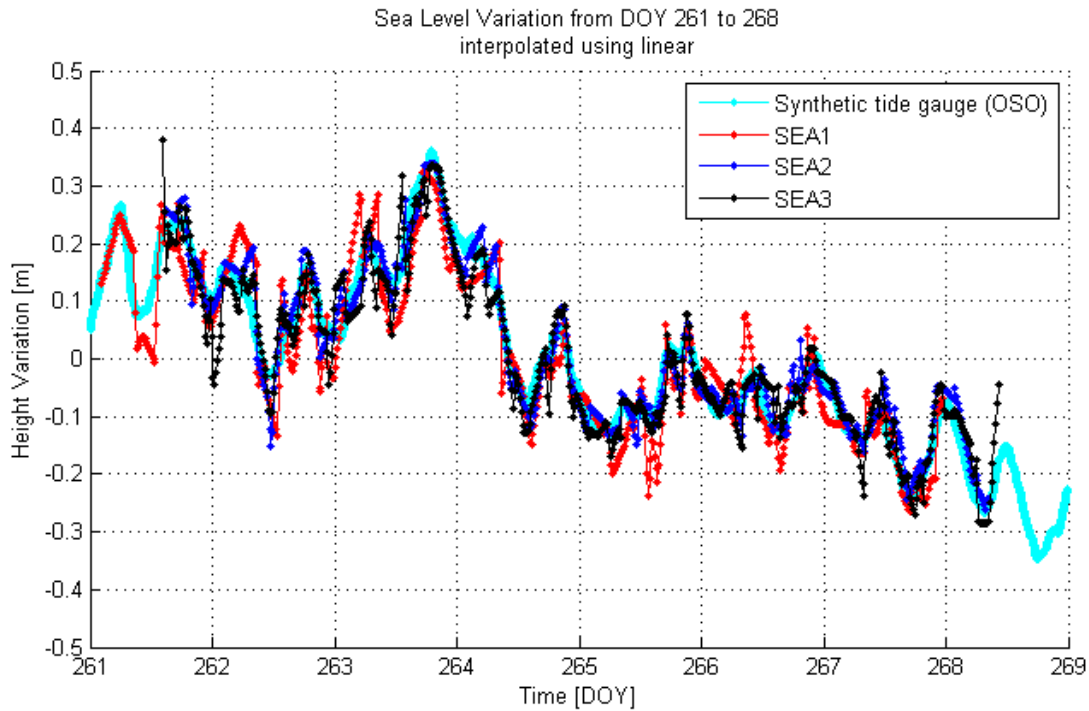


Figure 95: Interpolated (linear method) data for all the antennas from *day* 261 to *day* 268

On the other hand, another procedure can be applied to the data to enhance accuracy of the measurement. To do so, smoothing functions were applied to the original datasets in order to mitigate the variation of the data points and to better resemble the trend of sea tides. In all the cases, the algorithm of the MATLAB function that provided better result was performing the moving average of the data. Correlation coefficients and RMS values are presented in Table 22 while the time sequences are presented in Figure 96 and Figure 97 for the two *day* intervals. The table highlights the high increase of accuracy (RMS above 0.97 for short interval, and well above 0.95 for SEA2 and SEA3 in the long interval) and correlation, also observable in the figures by the lack of unwanted peaks.

Table 22: Correlation coefficient and RMS value for smoothed datasets

Smoothed using “moving” method				
	Parameter	SEA1	SEA2	SEA3
191 to 212	Correlation Coeff.	0.918609	0.957869	0.960665
	RMS	0.034893	0.025582	0.036191
261 to 268	Correlation Coeff.	0.970055	0.985996	0.978084
	RMS	0.038062	0.024648	0.030196

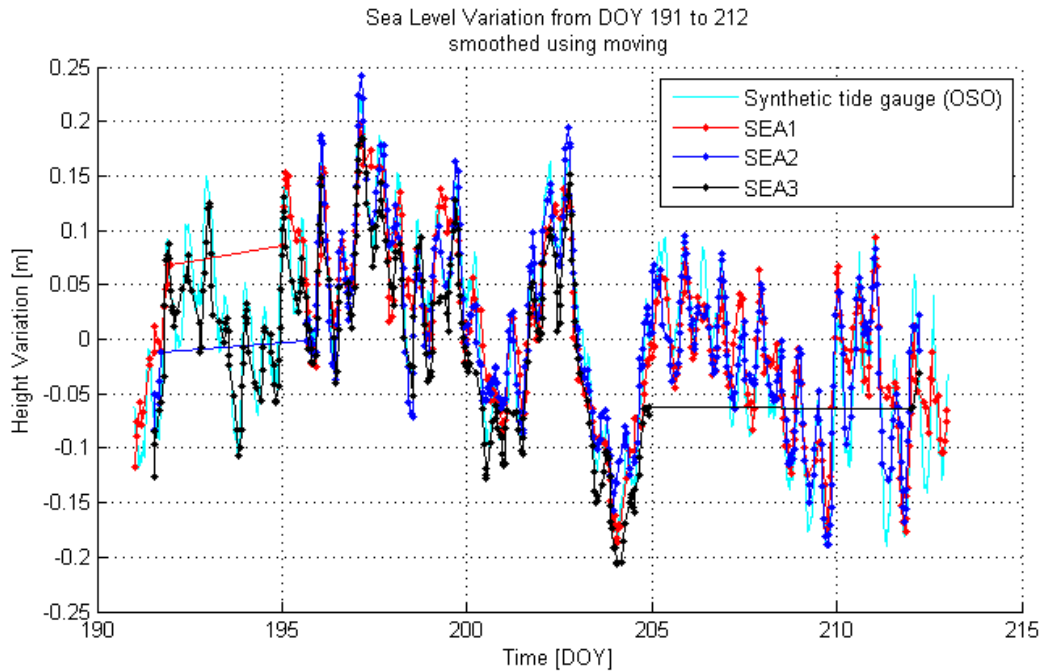


Figure 96: Smoothed data (moving method) for all the antennas from *day 191 to day 212*

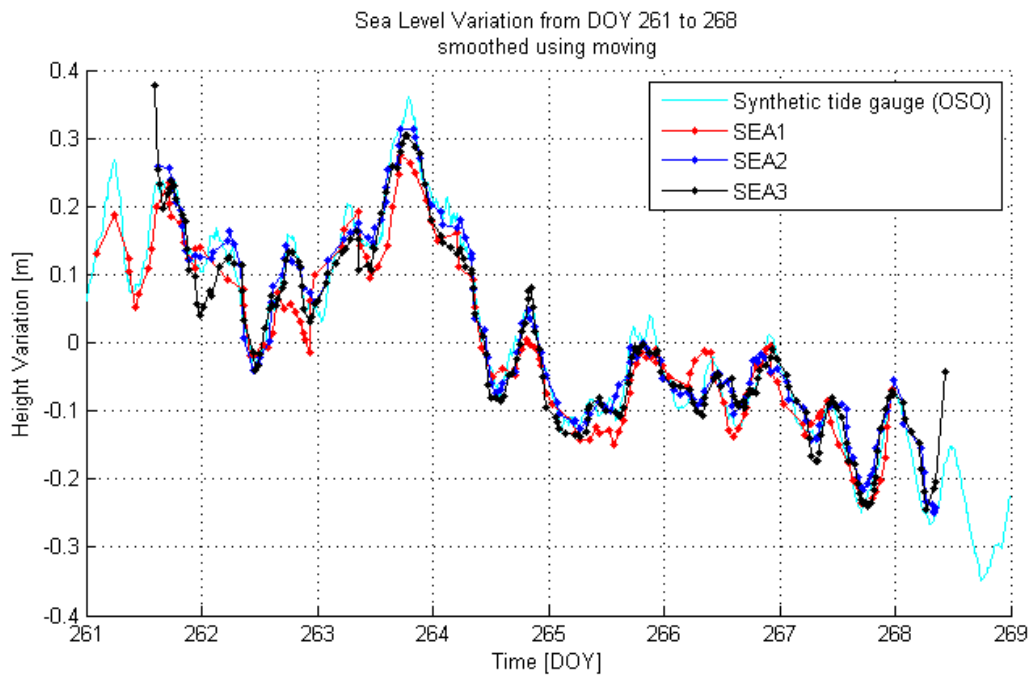


Figure 97: Smoothed data (moving method) for all the antennas from *day 261 to day 268*

At last, the two process were performed in sequence: firstly the data were interpolated to allow isolated peaks to maintain their relevance in the analysis. Lately, the smoothing function provided the time sequence characterized by the statistical results shown in Table 23. An overall degradation of these parameters can be seen, probably due to the error introduced by the interpolation and thus enhanced by the smoothing. It was observed during the analysis that incrementing the number of point did not largely modified the results.

Table 23: Correlation coefficient and RMS value for interpolated and then smoothed datasets

Interpolated and smoothed				
	Parameter	SEA1	SEA2	SEA3
191 to 212	Correlation Coeff.	0.354056 (0.562183)	0.548333 (0.641486)	0.576525 (0.571177)
	RMS	0.094934 (0.083133)	0.076865 (0.074104)	0.085852 (0.079476)
261 to 268	Correlation Coeff.	0.857622	0.671456	0.651057
	RMS	0.075245	0.111718	0.117038

5.6.6. Coupled antennas improvements

Another possible way to enhance the quality of the data, as far as the statistical parameter are concerned, is to use two antennas. This could for example be suitable for sites with more than one antennas in order to relate the measurements obtained processing the same signal by two different devices. In particular, the program investigates a possible relation between the datasets of two antennas, maintaining only the data close in time with each other. In other words, the measurement is intended as valid only if both the antennas have registered one data point within 10 minutes. This should allow to discard unreliable data and although the time resolution would be reduced, the accuracy of the data should result enhanced. Table 24 presents the results obtained using SEA2 and SEA3, which present the best comparable data. As shown, the correlation coefficient rises well above 0.915 for the long interval and above 0.955 for the short one. The RMS values provide an accuracy below 4 cm for SEA3 while for SEA2 there is no improvements with respect to Table 16. It is interesting to observe that by adding the two antennas together, the overall performances remains elevated while ensuring higher time resolution. Even in this case, if smoothing via moving average is applied, the parameters result enhanced. On the other hand, when SEA1 is used in combination with the other antennas, the results (not presented to avoid redundancy) seem to take different path. For the 22 days interval, the statistical parameters appear to be similar, correlation coefficient and RMS for SEA2/3 are above 0.92 and less than 0.41 respectively, while for SEA1 they are above 0.76 and above 6.1 cm. Differently, SEA1 and SEA2 comparison provided 211 data points while the other couple only 88. For the 8 days interval, SEA2/3 presented RMS below 3.3 cm and c.c. above 0.97 while SEA1 provided values above 6 cm and 0.9 respectively. In both cases the number of valuable data points was similar, 95 for SEA1-2 and 93 for the other case. As before, the addition of the singular series provided higher time resolution, while averaging the statistics of the two datasets.

Table 24: Statistical parameters for coupled antennas during two intervals of *doj*

Interval	Parameter	SEA2+SEA3	SEA2 C	SEA3 C
191 to 212	N Points	300	150	
	Interval Length [DOY]	9.643808	9.642859	9.643808
	Mean [m]	-0.022719	0.004574	-0.022621
	Max [m]	0.093069	0.093069	0.078847
	Min [m]	-0.175968	-0.138231	-0.175968
	RMS [m]	0.044738	0.046198	0.043229
	STD [m]	0.038605	0.040305	0.036962
	Correlation Coef.	0.926722	0.917004	0.936415
261 to 268	N Points	300	150	
	Interval Length [DOY]	6.732998	6.730799	6.730799
	Mean [m]	0.005389	0.005356	0.005422
	Max [m]	0.173044	0.090008	0.173044
	Min [m]	-0.143216	-0.143216	-0.100074
	RMS [m]	0.039004	0.037552	0.040404
	STD [m]	0.038695	0.037292	0.040173
	Correlation Coef.	0.961349	0.964159	0.958556

Additional information on the mutual relation between the coupled antennas can be found in Table 25. This presents the statistical relation between the two averaged sets. A first comparison with Table 17 shows an increasing degradation of the correlation coefficients within the relation between SEA1 and SEA3 when smoothing is applied. As said before, the best matching is defined by the two small antennas, maintaining a correlation coefficient above 0.9 for both intervals.

Table 25: Statistical information regarding coupled antennas

Interval	Points	Parameter	SEA1~SEA2	SEA1~SEA3	SEA2~SEA3
191 to 212	211 - 88 - 150	RMS [m]	0.069957	0.063612	0.045537
		Correlation Coef.	0.718634	0.760882	0.900980
261 to 268	95 - 93 - 150	RMS [m]	0.059802	0.067952	0.044110
		Correlation Coef.	0.905131	0.885796	0.949972

5.6.7. Total Campaign Dataset

Due to the discontinuity of the collected data, it is not possible to provide continuous longer time series of sea level variation. Nevertheless, the total campaign dataset containing few additional days is here presented in order to increase the generality of the results previously obtained. Figure 98 presents the time sequence for the whole year, whose statistical parameters are summarized in Table 26. A number of days near *doy* 160, 170, and 230 complete the series. The overall correlation coefficients remain stable across 0.9. A first comparison with Table 16 highlights a degradation of the RMS value for SEA2 (4.34 cm) and in particular for SEA3 (6.7 cm).

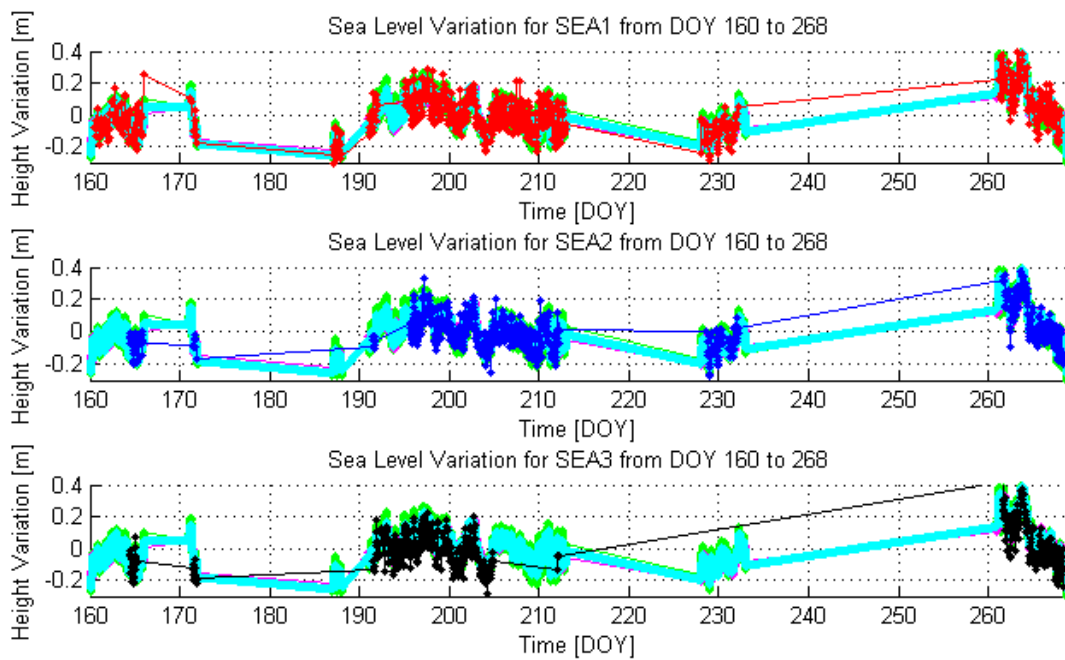


Figure 98: Sea level variation resulting from data processing for the three antennas

Table 26: Statistical results for the entire campaign

Parameter	SEA1	SEA2	SEA3
N Points	662	688	537
Interval Length [DOY]	38.105660	29.271100	22.609097
Mean [m]	-0.005423	-0.010504	-0.051258
Max [m]	0.223379	0.178624	0.119326
Min [m]	-0.144741	-0.162804	-0.212370
RMS [m]	0.057090	0.043400	0.067156
STD [m]	0.056875	0.042140	0.043429
Correlation Coef.	0.891662	0.931589	0.936450

Figure 99 shows the mutual relation between the measured sea level variation, with the one obtained from the synthetic tide gauge. The black line corresponds to the first order polynomial fitting the data. The elongated conformation of the data points indicates good correlation between each couple of sets. In particular, the closer similarity of SEA2 and SEA3 to the Onsala gauge can be observed to be superior with respect to the fairly scattered graph regarding SEA1.

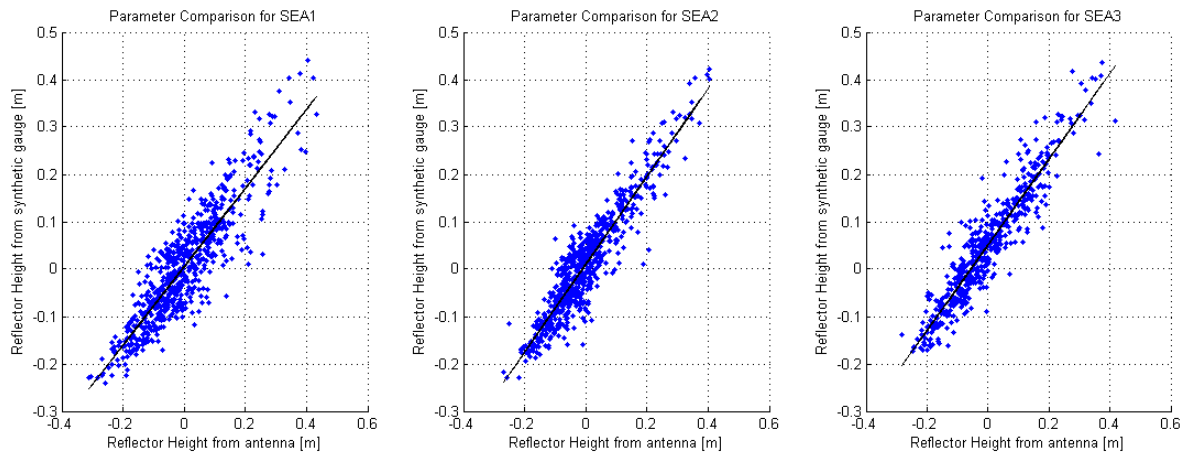


Figure 99: Comparison between antenna height and synthetic height for the whole datasets

The correlation coefficient, whose visual understanding can be grasped from the graph above, along with other statistical parameters have been observed with three azimuth intervals. The results are presented in Figure 100; the trend of the number of points available for the sea level variations seem to behave according to Figure 82 and Figure 83. The maximum error rises for SEA3 above 40 cm when wider azimuth intervals are used; viceversa it occurs for SEA1. The average value remains in any case around 20 cm. The RMS remains stable for SEA2, while for the other antennas it has a minimum for a higher azimuth angle of 200°. Nonetheless, SEA3 presents more than one third of RMS values (above 6.5 cm versus below 4.5 cm) than the “mate” antenna SEA2.

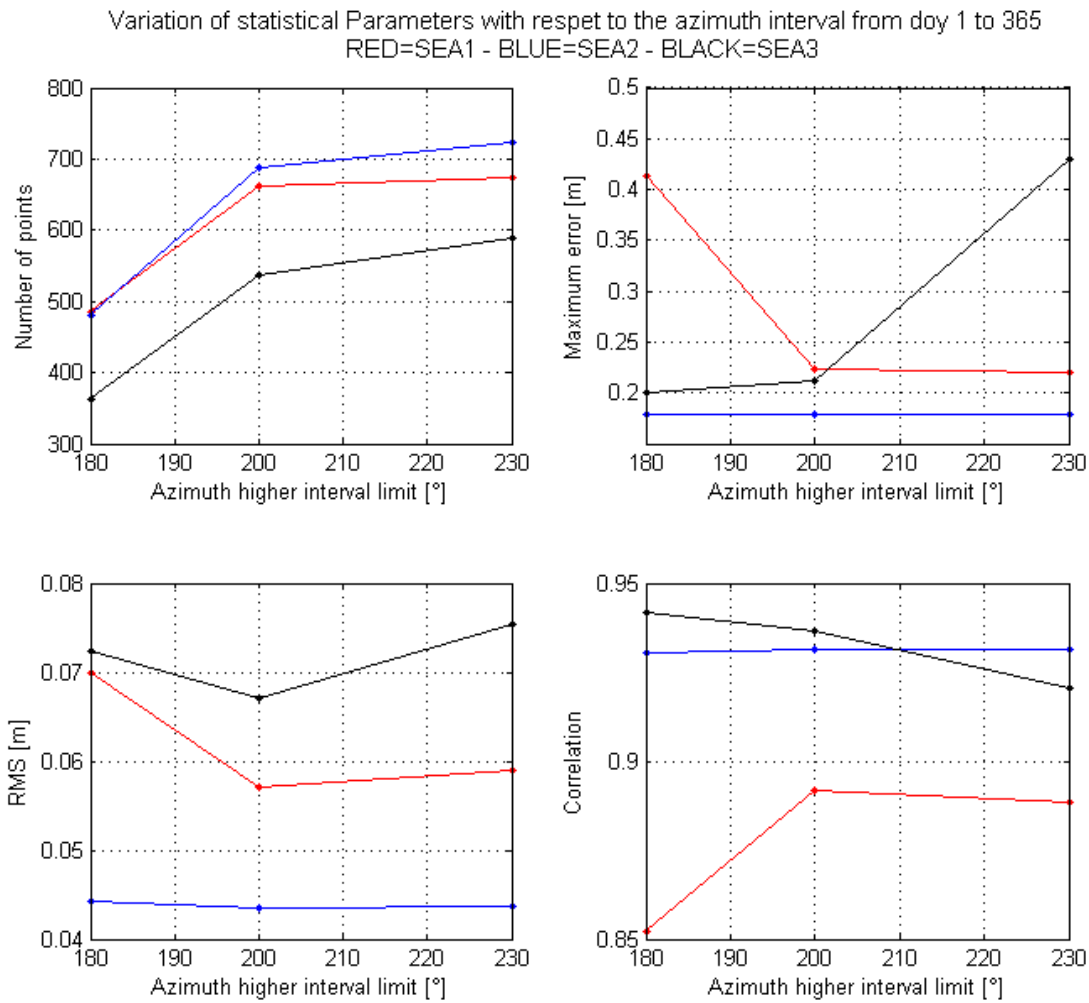


Figure 100: Variation of the statistical parameters with respect to the dimension of the azimuth interval for the whole datasets

The nature of the error can be observed in Figure 101 and Figure 102 where the predominance of positive or negative error is depicted. In particular, in Figure 101, a steady predominance of negative error is presented, particularly for SEA3 with a ratio below 0.1. Viceversa, the absolute errors seem to reach higher peaks while producing positive error for SEA3, showing a value of the ratio peaking to 1.9. Differently, SEA1 and SEA2 present similar amplitude in the mean positive and negative error, shown by the unitary value of the ratio in Figure 102.

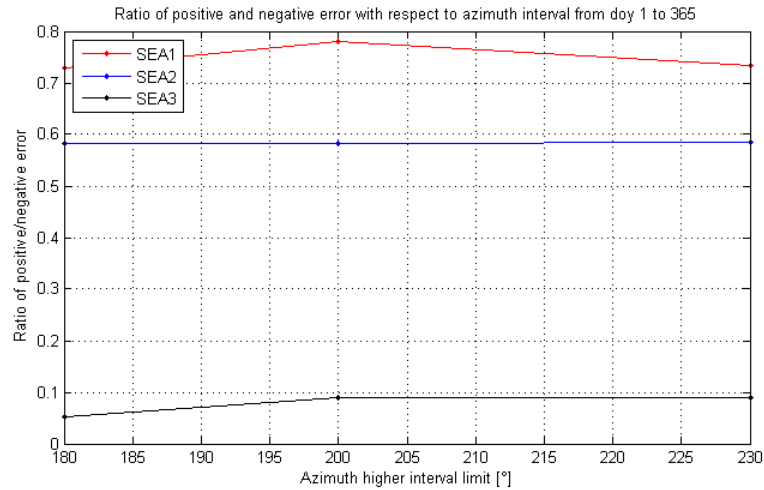


Figure 101: Ratio of negative and positive error with respect to the dimension of the azimuth interval for the whole datasets

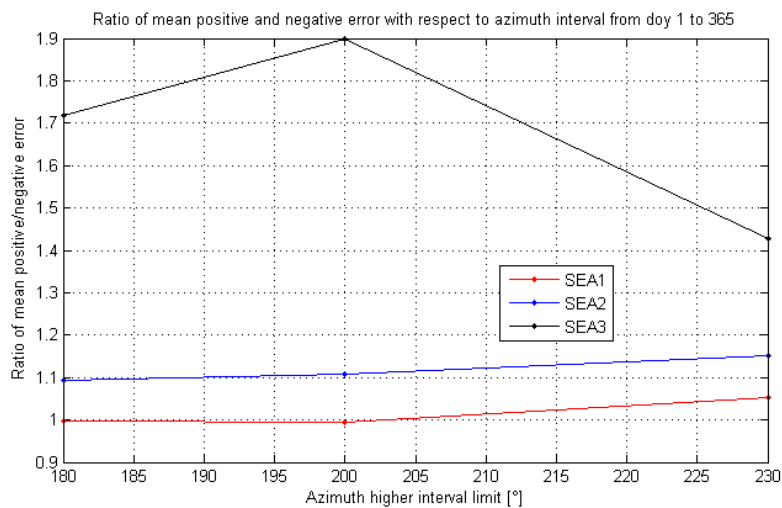


Figure 102: Ratio of mean negative and positive error with respect to the dimension of the azimuth interval for the whole datasets

This discrepancy can be also observed in Figure 103; the offset between SEA1 and SEA2 appear more restricted, and the data points do not look as scattered as for the case of the relation with SEA3. Nevertheless, in the first comparison, the black line, presenting the linear interpolation of the data points seems to deviate more from the purple line, projecting the ideal constant offset between the antennas. The most affinity is observed between the two smaller antenna, where black and purple lines are almost overlapped. This is consistent with what is found in Table 27 where the higher correlation coefficient is found when relating SEA2 and SEA3: 0.93, with an RMS of 4.5 cm. Similar correlation is shown for the first couple of antennas, with a value of almost 0.85. The RMS highly deteriorates to almost 8.2 cm, while it remains around 5.1 cm for the comparison of SEA1 and SEA3, even though the correlation between the two series plumps to 0.44.

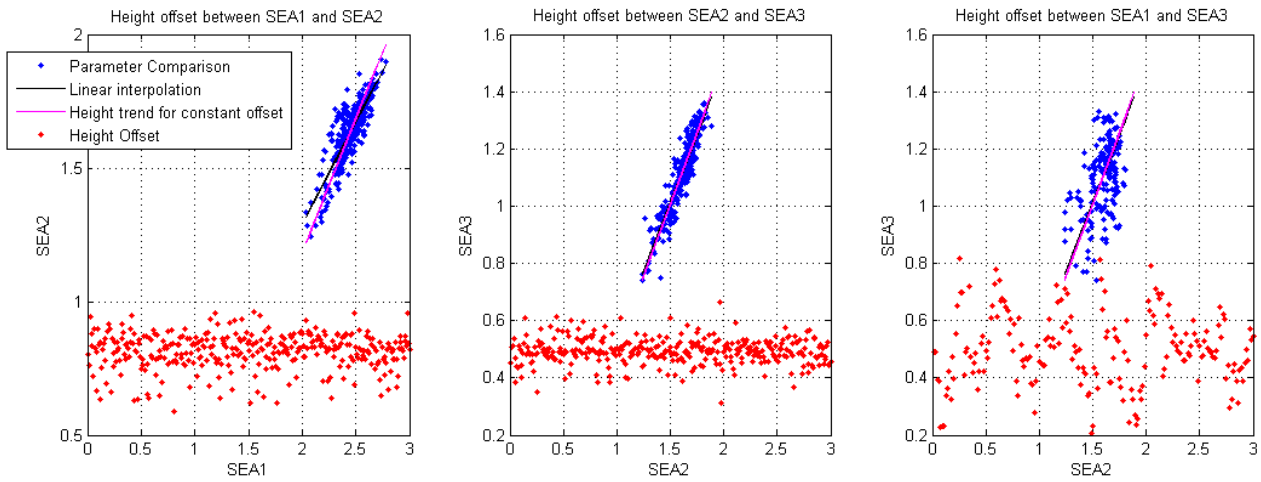


Figure 103: Height offset between the three antennas for the whole datasets

Table 27: Statistical results of the antenna comparisons for the whole datasets

Parameter	Points	Mean	Max	Min	RMS	STD	Correlation Coef.
SEA1 – SEA2	342	0.814363	0.961391	0.588609	0.817070	0.066552	0.849399
SEA2 – SEA3	323	0.493483	0.664546	0.310589	0.495548	0.045266	0.934245
SEA1 – SEA3	192	0.499111	0.815792	0.206348	0.514745	0.126227	0.442634

As far as the weather condition are concerned, even on a general overlook the parameters such as wind speed, humidity, pressure and temperature do not seem to be influent on the error generations. The correlation coefficients are positioned mainly below 0.1, highlighting unlinked behavior between the trends. Only the direction of the wind seems to have preferential azimuth angle when it comes to the presence of error of relevant entity (i.e., above 10cm), as shown in Figure 104. This can be partially confirmed by observing that only 43.1 percent of all the data points present an error for wind direction across 250°, while almost 60 % of points present values above 10 cm when the wind direction was across 250°.

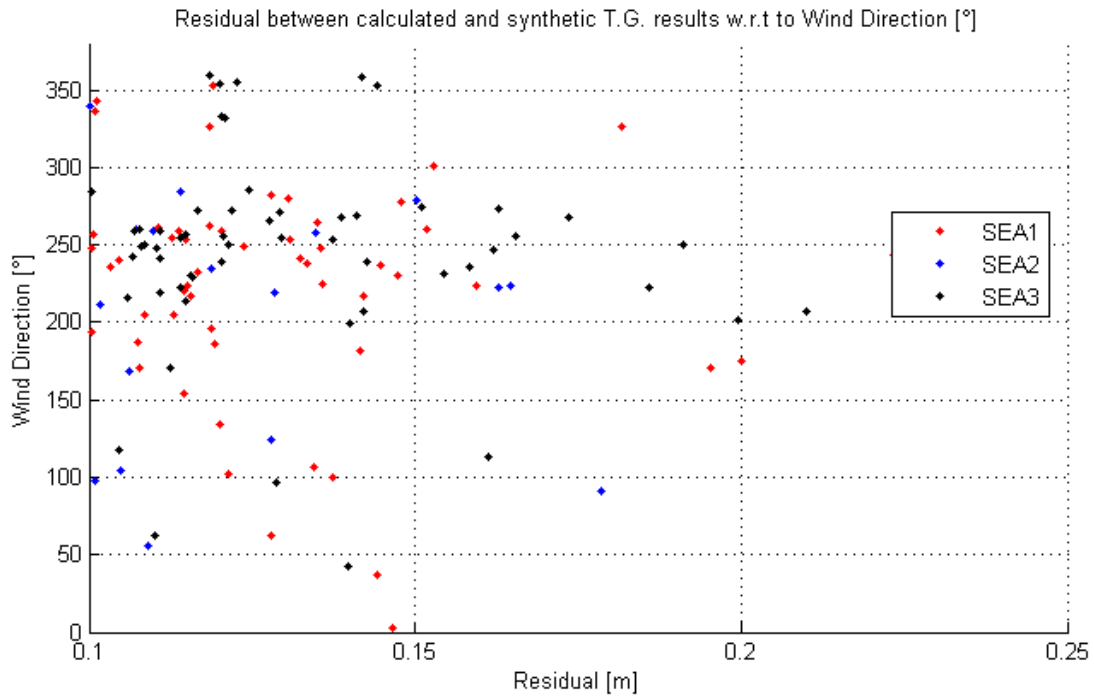


Figure 104: Wind Direction influence on the detection of larger errors for the whole datasets

Due to the distribution of available *day* throughout the year, an interpolation of the unified time series is not feasible. Nonetheless, in order to improve the data and in particular the statistical parameter, smoothing procedure can be applied to the height variations. Table 28 resumes the main parameters resulting by applying a smoothing function using moving average method. All the antennas provide a correlation coefficient above 0.95, with SEA3 reaching a peak of 0.975. On the other hand SEA2 registered the minor RMS, 3 cm, while SEA3 remained below 6 cm along with SEA1.

Table 28: Correlation coefficient and RMS value for smoothed for the whole datasets

Smoothed using “moving” method			
Parameter	SEA1	SEA2	SEA3
Correlation Coeff.	0.952813	0.968763	0.974713
RMS	0.035993	0.030966	0.057848

As explained in 5.6.6, the RMS can be partially reduced by performing a cross analysis on the data from different antennas. Better improvements can be achieved with similar devices, e.g. in this case SEA2 and SEA3 as justified below. Table 29 presents the main results using for each antenna only the data obtained in similar times by both antennas along with a longer time sequence obtained by the combination of the two stand alone. All the series present a correlation coefficient across 0.95, while the RMS has values around 6.2 for all the datasets. More accurate result can be obtained by applying the smoothing process

alluded above, gaining circa plus 0.02 in the correlation coefficient and 0.5 cm in RMS for all cases. From the table, it can be also noted that the maximum absolute errors are not mitigated in this process, presenting for both antennas values around 20 cm. Using SEA1 as comparison antenna does not bring to similar improvements in the sea variation measurements. As deductible from 5.6.6, the affinity between the small antenna with the choke ring one results to be poorer. Table 30 reflects the behavior already observed in Table 25, with a constant good correlation of 0.93 between SEA2 and SEA3, more than 0.05 points above the other couples. Similar relation link the RMS value, achieving 4.5 cm circa for the first case, 2 cm less than the value for the comparison with SEA1.

Table 29: Statistical parameters for coupled antennas for the whole datasets

Parameter	SEA2+SEA3	SEA2 C	SEA3 C
N Points	646	323	
Interval Length [days]	17.398565	17.388241	17.391273
Mean [m]	-0.048987	-0.049060	-0.048915
Max [m]	0.117545	0.065728	0.11754
Min [m]	-0.203752	-0.197283	-0.203752
RMS [m]	0.062654	0.062983	0.062323
STD [m]	0.039091	0.039558	0.038679
Correlation Coef.	0.949784	0.947990	0.951645

Table 30: Statistical information regarding coupled antennas for the whole datasets

Points	Parameter	SEA1~SEA2	SEA1~SEA3	SEA2~SEA3
342 - 192 - 323	RMS [m]	0.066454	0.064809	0.045196
	Correlation Coef.	0.849399	0.869148	0.934245

5.7. Discussion

Firstly, it has to be said that no measurement on the absolute reflector height were obtained due to the lack of references in situ to prove the data. For this reason, only differential measurements were performed, also allowing to neglect possible bias error of the system. Tropospheric and Ionospheric errors were neglected due to the coupled usage of direct and reflected signal, that make these effect to have no impact on the SNR fluctuation frequency. As proved by Table 16, the test campaign yielded successful results showing an overall correlation of about 0.95 for a timespan on a short term of 8 days in the case of SEA2 and SEA3, while it decreases to around 0.9 for 22 days. Differently the values for SEA1 were found to be 0.9 circa for the short period and 0.81 for the longer one. However, analyzing the entire sets of data SEA1 maintained the good correlation observed in the first case, with a value near 0.9, similarly to the behavior of the smaller antennas. The relevant increment in the statistics of SEA1 is probably related to the strong increase of available data points, obtained enlarging the *doy* intervals. Viceversa, a visible degradation in the RMS of SEA3 is due to the scattered nature of the additional days, causing a non-continuous stream of information. In all cases, the mean time resolution of the data fluctuated from 46 to 70 minutes for SEA2 and SEA3 and was above 70 minutes for SEA1, being able in this way to map the variation of the sea level constantly. Regardless the increase in data points, the time resolution of the choke ring antenna rose to 83 minutes when analyzing the whole days available, while it stabilized to 60 minutes for other two sets. The data concerning the correlation between GNSS data and synthetic gauge data and furthermore between the various antenna suggest an important aspect. From these data it seems that the key role in the reliability of the data is due to the antenna model, more than in the orientation of the antenna itself. This could be justified by the fact that the SNR signal is detrended by the program and the only necessary information contained in that is the frequency. In addition, Figure 78, Figure 79 and Figure 99 bring more evidences of this behavior. It has to be said, that SEA2 and SEA3 are place very closed to each other, even though SEA1 it is not so far away to suppose such different kind of signal received by the antennas. The discrepancy can then also justified by environmental characteristics that could have distorted the signal. If we look at the location of SEA2 and SEA3 in Figure 54 and in Figure 55 the antennas are isolated, just above the sea with no other source of signal than the one coming from the direct and reflected signal of the azimuth mask. At certain angles also the small cabin near the antenna could have produced some sort of reflection at an angle around 150°. This issue has been seen in the analysis at times, even though it is not so relevant. This effect, which can be called *backscatter* induced multipath, could differently because of major error for SEA1 or bad data rejection. The high presence of rocks, the nearby cabin the vegetation behind the antenna could have create additional sources of multipath, creating a disturbance in the SNR not directly derivable from the sea surface status. This, in addition to the different gain patter, could have brought to lower results if

compared to the other two cases. Consistently to this reasoning, in Figure 80 and Figure 81 the error distribution for SEA1 shows lack or absence of data nearby 150° of azimuth, and an increase of the error for the following $15-20^\circ$ of azimuth. Moreover, similar behavior can be seen around the 100° azimuth angle. In this case, the probable cause of error can be given to the presence of the small island that was producing additional multipath reflection. The smaller antennas do not show any particular behavior with respect to the azimuth angle, and the peak value of the error could be intended as random errors. On the other hand, the errors for these antenna seems to be higher for higher elevation angles. This should be linked to the shape of the SNR, being less defined in terms of its sinusoidal shape. In addition, location closer to the antenna could be more affected by the sea motility and thus resulting less precise in some cases.

Figure 82, Figure 83 and Figure 100 show the behaviors of the statistical parameters at the increasing of the azimuth mask interval. As reasonable, the number of available points increase with the widening of the interval, in all cases with the same ratio with respect to the antenna layout. The reason behind this trend can be found in the fact that at high azimuth the effect of the surrounding environment affects more the reflected signal, thus making impossible to retrieve the height. The two smaller antennas show a more stable trend of the correlation factor thus indicating more reliability on the measurement. The lower factor in the longer interval is probably due to the larger amount of data available for the analysis. The absolute maximum error behaves smoothly for the small antennas in the shorter interval of days. SEA1 showed a high error for azimuth upper limit equal to 180, not seen in the following results, probably due to the few data available and the limitations of the program (e.g. std cutoff). Differently, for *day* from 191 to 212 the error remains smaller for SEA3, probably due to the fewer days interested in the analysis. In fact, with higher number of point and wider azimuth interval the error rises above the one from the other two antennas. A behavior confirmed by Figure 100, where the maximum error of SEA3 rises above 40 cm, highlighting the unsuitable width of the interval. Finally, the RMS value maintained similar distinction for both time intervals. SEA1 resulted to be the less accurate antenna, with SEA2 being the most one. Strangely, SEA1 showed to be less accurate for shorter intervals of time, probably due to the lack of data points available. SEA2 and SEA3 behaved more stably, even though the RMS of SEA3 rose well above 5.5 cm, more than 1.5 cm more than SEA2 RMS for the widest interval. On the other hand, for an azimuth limit of 200 the RMS seems more acceptable. This can be extended to the analysis performed on all days available with the exception of SEA3. In this case in fact, even though the trend remains similar to the one observed in the previous intervals, the RMS rises well above 0.65 m. Such degradation could only be justified by the poor quality of the data, and to the scattered layout of the points, given

that the RMS value of the remaining antennas are approximately an average value of those from the 8 and 22 days interval. This can be also supposed by observing that in the sets of images for the two time intervals, at similar number of data points SEA3 produces an RMS that is consistent in both cases.

As far as the error source is concerned, SEA1 shows a predominance of negative error in the shorter interval of time, showing a source probable due to the program. In addition, at higher azimuth limits, the ratio of the mean between positive and negative rises, indicating a possible source of positive error, such as the rocks visible in Figure 53. For larger periods, the figures show more stable trend of the error for SEA1, preferable of negative nature as confirmed by Figure 102. This is probably due to the mitigation induced by the higher number of points. The ratio of the mean amplitude also suggests the mutual nature of the errors. On the other hand, SEA2 was affected by higher quantity of positive errors thus remaining of smaller amplitude when compared to the negative ones in the shorter intervals. When more days are observed, the number of negative error increases also in correlation. However, Figure 102 suggests that such errors are limited in amplitude, reason why the mean of positive error tends to be superior, also consistently with the presence of obstacle at higher azimuth. Overall, the small excursion of these ratios could indicate an appropriate behavior of the antenna, and the absence of major source of error due to the environment. Oppositely, SEA3 was affected by several negative errors, while the higher magnitude of the error occurred in the case of positive errors. In particular, higher positive error is defined in the case of higher density of negative error within the shorter interval of days. Overall it seems that at higher azimuth the number and mostly the amplitude of negative error increase. This could led to assume that there could be a defined source of high positive errors that affects the measurements only at defined azimuth angles, and less likely to be due to random errors, as can be seen by the value for the azimuth limit of 200. In addition, increasing the data points the ratio of the means seems to neglect the higher values of the errors, due to cancellations internal to the software and to an homogenization of the error sources.

The relationships between the antennas show consistent results between the two different intervals of time and also the full datasets. Even though the comparison between SEA1 and SEA3 produced results concentrated in a restricted area, both the shape of this group and the one composed by SEA1 and SEA2 appear to separate more from the line of constant offset (in purple). In particular, for the wider interval of 22 days, a rounded shape is acquired by the cluster, showing high discordance, partially noticeable also in Figure 103. On the other hand, as to be expected, a fairly constant offset of around 0.5 meters is

detectable from the figure and confirmed by Table 17 and Table 27. In the comparison between SEA2 and SEA3 from Figure 88 to Figure 89, it is possible to see not much increment in the data points: this is due to the different actual days of data available for both antennas. It is noticeable that in all the figures the points remain constraint in a narrower strip, as also indicated by the similarity of the two line (black and purple). Differently, when comparing SEA1 and SEA2 and even more SEA1 and SEA3, the points remained scattered even in the shorter interval, showing a chronic tendency to the generation of higher errors and a general discrepancy on the two antenna models.

Weather conditions showed no apparent interaction with the measurements. Not wind nor rain seem to highly affect the SNR, the data analysis or the antenna receptivity of the interested signals. The wind direction could however interact with the sea surface creating waves in particular direction that could partially induce to higher error as suggested by Figure 104. On the other hand, the wind speed once above 2 m/s does not affect the analysis, given also the fact that absence of wind (or presence below 2m/s is hardly rare along the shoreline. Hence, the method illustrated seems to suitably be used in coastal environment, in presence of precipitations and active sea surface motility.

In the end, manipulation of the useful data on sea level variation have brought to different results. Interpolating the data did not bring to any improvements in any of the intervals analyzed. This is partially due to the non-continuity of the data. Better results were obtained by SEA1, probably related to the original small number of available data points collected. The application of smoothing procedures brought nonetheless to great enhancing both in correlation and in accuracy. This is due to the pseudo regular trend of the tides, that can be nicely fitted by sinusoidal shapes. In particular, the high coefficient of SEA3 should be due to the reduced number of data points (if compared to SEA2) that allowed finer corrections. The enhancement on the RMS is also due to the breakdown of the major errors. The other methodology to enhance the quality of the measurements utilizing two antenna in combination is a low cost approach suitable for specific sites. With this approach an increase in statistic parameters can be obtained while not sacrificing much time resolution. In fact, by analyzing only the data coming from two antenna at the same time it is possible to discard unsure data and mediate between two input. This led to correlation coefficients above 0.93 in all cases, and in particular above 0.945 while analyzing the whole sets of data. This remains constant also when adding the contribution of the two antennas together, thus providing a higher resolution. Nonetheless, it has to be said that this improvement in time resolution is due to the presence of couple of point close to each other and thus it does not provide a generalized

higher density of the measurements. In addition, an important aspect can be observed in the relevant decrement in accuracy within the results for the whole campaign. The RMS of SEA2 and SEA3 combined plumps to 6.3 cm while for the two intervals were stable below 4.1 cm. This is due to the distribution of the additional point that does not bring to major affinity between the two time series and to the probable exclusion of major standalone peaks. However, applying smoothing function brings to improved results, given the positioning “in couples” that strengthen the importance of the singular points in the analysis. This could result useful in location with multiple pre-installed antennas that could work in combination.

6. Conclusions

6.1. Simulator

A simulator made in-house was presented in order to observe the behavior of SNR signals and to test the program calculating the height of the reflector from the antenna. Multiple features have been tested such as the antennas orientation, the polarization of the antennas and different heights. The simulator was able to rapidly create an idealized sinusoid that gave the opportunity to understand the interaction of the characteristics of both the antennas and the environment. The data obtained using sea water as reflector were later analyzed through a Lomb-Scargle periodogram to retrieve the height and compare it to the value given in input. In the case of trended data, the two upward looking antennas showed high fluctuating error, reaching peaks above 10 cm of error. Differently, when the data were detrended this error remained under 4.5 cm. The antenna pointing to the horizon showed no major enhancement when the data were detrended, showing an error of less than 3 cm for the majority of the interval. These level of error is probably due by the assumption of using sea water as reflector, not known by the program calculating the height. When the reflector material was switched to perfect reflector, the error in all cases was less than 5 mm, showing the suitability of the process to calculate sea level variations.

6.2. Sea Level Measurements

During this test campaign, two different antennas in 2 configurations were tested. A choke-ring antenna (LEICA AT504GG) was set to point upward, while two other smaller antennas (LEICA AX1202) were

pointing one upward and one to the horizon. This last layout was done to maximize the effect of an important phenomenon: the Multipath. Using SNR data coming from the antennas, good correlation has been found between the periodogram analysis of the antenna data and the tide gauge-derived values. For a set of 22 days, the two small antennas showed a correlation not less than 0.89 with a RMS value below 0.05 m. Differently the choke ring antenna showed worse results probably due to its position and to its gain pattern, the correlation was below 0.9 and a RMS of more than 5.5 cm. The time resolution fluctuated around 1 hour or slightly more. In particular, the small upward looking antenna showed the best time resolution and best RMS value: 4 cm. It has to be said that, by lowering the azimuth mask, along with a decrease of time resolution/data points and of the accuracy, an increase was found on the correlation of the choke ring antenna. For a set of 7 days, similar relations between the data were found, showing an overall better accuracy and RMS for all the configuration, due to the lower number of points. Analyzing the data collected during the whole campaign, hence adding variable number of days to those referenced above, the antennas pointing upward maintained useful statistical parameters. The choke ring provided a correlation coefficient above 0.88 with an RMS slightly higher than 5.5 cm while the smaller antenna had constant RMS at 4.3 cm and coefficient at 0.93. Similar correlation parameter was provided by the antenna point to the horizon, even though the RMS rose as high as 0.67 in the best case. Doubt are still unclear on the sudden lack of accuracy, probably due to the poor quality of the additional data. The statistical parameters, and in particular the relation observed between the coupled antennas, suggest a higher relevancy of the antenna model than of the angle of tilting of the antenna itself on the height variation retrievals. Environment disturbances have also to be taken in count, even though weather conditions seems not to have provided any relevant source of error to the analysis. This suggest the possibility to use similar antennas in coastal environment also in presence of adverse weather condition without losing in reliability. Applying interpolation algorithms does not seem to enhance the data, even though smoothing procedures enhance both the accuracy and the correlation, obtaining in isolated cases, values above 0.97. Another methodology to validate the results was consisting in combine data from two antennas in order to discard standalone uncertain data. This was shown to improve the correlation to value across 0.95 and isolated RMS value around 4 cm, even though the complete datasets provided poorer value around 6.3 cm. Clues suggest that the cause of the degradation in the quality of the result could be given to the lack of data, and to the poor quality and homogeneity of the one added to the two wider intervals. However, a combination of more antennas could be ideally free of charge while bringing higher correlation in specific pre-existing suitable circumstances.

7. Future Work

Even though the remote sensing methodology is not likely to replace the current tide gauge system, the widespread antenna network could give important information for altimeter calibration or for low cost-easy positioning measurements. Given the high density of upward looking antennas for geodesy studies, it could be useful to perform studies similar to the one exposed, utilizing different type of antenna to understand their behavior in the case of multipath phenomenon. In addition, different location should be analyzed, in order to neglect or better define the constrictions on the signal direction due to environment shape. By doing so, the usage of geodetic data/signal could be organized and simplified. Multiple antennas with multiple setups, where provided, could also be used in combination to provide higher accuracy and time resolution. On the other hand, it would be very useful to make use of different GNSS signals, such as GLONASS or GALILEO, in order to increase the temporal resolution and perhaps comparing similar results to obtain better accuracy.

8. References

Auerbach, J., *“GPS and Worldwide GNSS Interoperability”*, Office of Space and Advanced Technology, U.S. Department of State, Washington, D.C., USA, 2010.

Bedford, L. et al, *“LEICA AR25 –White Paper-”*, Leica Geosystems AG, Heerbrugg, Switzerland, 2009a.

Bedford L., Brown N., Walford J., *“Leica AR25: White Paper”*, Leica Geosystems AG, Heerbrugg, Switzerland, 2009b.

Bindoff, N.L., Willebrand, J., Artale, V., et al. *“Observations: oceanic climate change and sea level, in: Solomon, S., Qin, D., Manning, M., et al. (Eds.), Climate Change 2007: The Physical Science Basis. Contribution of Working Group I to the Fourth Assessment Report of the Intergovernmental Panel on Climate Change.”* Cambridge University Press, Cambridge, United Kingdom and New York, NY, USA, 2007.

Braun, J.J., *“Assessing the Impact of the SCIGN Radome on Geodetic Parameter Estimates”*, Boulder, CO, USA, 2007.

Craymer, M.R., *“The Least Squares Spectrum, Its Inverse Transform And Autocorrelation Function: Theory And Some Applications In Geodesy”*, University of Toronto, Toronto, CANADA, 1998.

Danti,E., Sarmineto, R., *“Trattato Dell’uso Et Della Fabbricazione Dell’astrolabio Con L’aggiunta Del Planisfero Del Roia”*, Firenze, FI, Italy, 1569.

Doberstein, D., *"Fundamentals of GPS Receivers: A Hardware Approach"*, Springer Science+Business Media, New York, NY 10013, USA, 2012.

Dunne, S., et al, *"Oceanpal@, A Gps-Mflection Coastal Instrument To Monitor Tide And Sea-State"*, Starlab Barcelonn S.L., Barcelona, SPAIN, 2005.

Lodde, E., *"Manual on Sea-level Measurements and Interpretation, Volume IV : An update to 2006"*. Paris, Intergovernmental Oceanographic Commission of UNESCO. 78 pp., Paris, FRANCE, 2006.

Hannah, B.M., *"Modelling and Simulation of GPS Multipath Propagation"*, The Cooperative Research Centre for Satellite Systems, Queensland University of Technology, AUSTRALIA, 2001.

Hofmann-Wellenhof, B. et al, *"GNSS – Global Navigation Satellite Systems"*, Springer-Verlag, Wien, AUSTRIA, 2008.

Istituto e museo di storia della scienza, *"L'Astrolabio"*, Firenze, FI, Italy, 2004

Kaplan, Elliott D. et Hegarty, C. (Christopher J.), *"Understanding GPS: principles and applications-2nd ed."*, ARTECH HOUSE INC, Norwood, MA, USA, 2006.

Li J., *"Lomb-Scargle Periodogram"*, Univerity of Florida, 2009

Larson, K. M., Small, E. E. , Gutmann, E. D. , Bilich, A., Braun, J. J. , and Zavorotny, V. U., "Use of GPS receivers as a soil moisture network for water cycle studies," *Geophys. Res. Lett.*, vol. 35, p. L24405, 2008, DOI:10.1029/2008GL036013.

Larson, K.M. Ethan D. Gutmann, Valery U. Zavorotny, John J. Braun, Mark W. Williams and Felipe G. Nievinski, *"Can we measure snow depth with GPS receivers?"*, *Geophysical Research Letters*, VOL. 36, L17502, doi:10.1029/2009GL039430, 2009.

Larson, K.M., John J. Braun, Eric E. Small, Valery U. Zavorotny, Senior Member, IEEE, Ethan D. Gutmann, and Andria L. Bilich, *"GPS Multipath and Its Relation to Near-Surface Soil Moisture Content"*, *Ieee Journal Of Selected Topics In Applied Earth Observations And Remote Sensing*, VOL. 3, NO. 1, 2010.

Larson, K. M. et Nievinski, F.G., *"GPS snow sensing: results from the EarthScope Plate Boundary Observatory"*, Department of Aerospace Engineering Sciences, University of Colorado, Boulder, Boulder, CO 80309-0429, USA, 2012a.

Larson, K.M., et al. *"Coastal sea level measurements using a single geodetic GPS receiver"*. *J. Adv. Space Res.*, <http://dx.doi.org/10.1016/j.asr.2012.04.017>, 2012b.

Löfgren, J.S., Haas, R., Johansson, J.M. “Sea Level Monitoring Using a GNSS-Based Tide Gauge”, in *Proceedings of 2nd International Colloquium - Scientific and Fundamental Aspects of the Galileo Programme*, Proceedings CD-ROM, European Space Agency, 2009.

Löfgren, J.S., Haas, R. Johansson, J.M. “High-rate local sea level monitoring with a GNSS-based tide gauge”, in: *Proceedings of the 2010 IEEE IGRSS, 25–30 July, Honolulu, HI, USA*, pp. 3616–3619, 2010.

Löfgren, J.S., Haas, R., Johansson, J.M. “Monitoring coastal sea level using reflected GNSS signals”. *Adv. Space Res.* 47 (2), 213–220, 2011a.

Löfgren J. S., Haas, R., Scherneck, H.G. and Bos, M.S., “Three months of local sea level derived from reected GNSS signals”, Department of Earth and Space Sciences, Chalmers University of Technology, Gothenburg, Sweden, 2011b.

Lowe, S. T., Zuffada, C., LaBrecque, J.L., Lough, M., Lerma, J., and Young, L. E., “An Ocean-Altimetry Measurement Using ReflecteGdP S Signals Observed from a Low-Altitude Aircraft”, Jet Propulsion Laboratory, California Institute of Technology, Pasadena, California, USA, 2002a.

Lowe, S. T., Zuffada, C., Chao, Y., Kroger, P. and Young, L.E., “5-cm-Precision aircraft ocean altimetry using GPS reflections”, Jet Propulsion Laboratory, California Institute of Technology, Pasadena, California, USA, 2002b.

Lowe, S. T., Zuffada, C., Labrecque, J.L., Romans, L.J., Young, L.E., Hajj, G.A.et al.: “First Spaceborne Observation of an Earth-Reflected GPS Signal”, JPS, California Institute of Technology, Pasadena, CA, USA, 2002c.

Manz, A., “Radome Influence on Weather Radar Systems: Principles and Calibration Issues”, Gematronig GmbH, Neuss, Germany, 2001.

Markvart, T. et Cantañer, L., “Practical Handbook of Photovoltaics: fundamentals and Applications”, Elsevier Science Ltd. The Boulevard, Langford Lane, Kidlington, Oxford, OX5 1GB, UK, 2003.

Martin-Neira, M., “A Passive Reflectometry and Interferometry System (PARIS): Application to Ocean Altimetri”, Razio-Frequency System Division, ESTEC, Noordwijk, The Netherlands, 1993.

Misra, P., Enge, P., “Global Positioning System: Signals, Measurements, and Performande – Revised Second Edition”, Ganga-Jamuna Press , Lincoln, MA, USA, 2011.

Nievinski, F.G. “A GPS multipath simulator for near-surface reflectometry and positioning applications”, University of Colorado, CO, USA, 2013.

Novatel, "GPS-701-GG and GPS-702-GG", Canada, 2011

Office of Science and Technology Policy, "Statement By The President Regarding The United States' Decision To Stop Degrading Global Positioning System Accuracy", Washington, DC, USA, 2000.

Ruffini, G., Soulat, F., Caparrini, M., Germain, O. and Mart'ın-Neira, M. (2004), "The Eddy Experiment: accurate GNSS-R ocean altimetry from low altitude aircraft", Geophys. Res. Lett., 31, L12306, doi:10.1029/2004GL019994, 2004.

Semmling, A. M., Beyerle, G., Stosius, R., Dick, G., et al, "Detection of Arctic Ocean Tides using Interferometric GNSS-R Signals", Geophysical Research Letters, 2011.

Soulat, F., Caparrini, M., Germain, O., Lopez-Dekker, P., Taani M. and G. Ruffini, "Sea state monitoring using coastal GNSS-R", Geophysical Research Letters, DOI:10.1029/, 2004.

Treuhaft, R.N, Lowe, S. T., Zuffada, C, and Chao, Y., "2-cm GPS altimetry over Crater Lake", Geophysical Research Letters, vol. 22, no. 23, pages 4343-4346, DECEMBER 1, 2001.

Walford, J., "Leica GNSS Reference Antennas –White Paper-", Leica Geosystems AG, Heerbrugg, Switzerland, 2012.

Watkins, K. et al., "Human Development Report 2007/2008: Fighting climate change-Human solidarity in a divided world", United Nations Development Programme, Palgrave Macmillan, New York, NY, USA, 2007.

Zogg, J-M, "GPS: Essentials of Satellite Navigation –Compendium-", 2001.

9. Appendix

The following chapter is intended to briefly explain the functioning of the simulator. In particular it will present the main features and parameters that can be set up for the signal generation. The link to folder containing the scripts used will also be given.

9.1. Basic Functioning of the Simulator

The simulator consists of a main script from where it is possible to access a various set of settings through specified functions and variables. Once these characteristics are set, the program introduces them into the core and it produces the data for the SNR along with information about the carrier and SNR error and interpolation calculation results.

The settings are divided in 8 main groups inside a variable of type “structure” in the program: *ref or reference, opt or general option, opt.cdma or code modulation option, opt.rec or receiver option, bias, ant or antenna, sfc or surface, sat or satellite*.

- *Reference* block is related to the layout of the experiment and the reference points of the antenna. In this section it is possible to define the height of the antenna from the surface as well as the ARP, APC offset from ARP (known from each antenna) and the distance between the monument (support) pivot point and the ARP.
- *General Options* block consists in a set of option regarding the signal itself, such as frequency, code of encrypting and satellite block name. In addition, is it possible to handle the shape of the

output by forcing a partial simulation, absence of losses, absence of correlation between elevation and power acquired. Other general option regards physical optics features and their specification.

- *Code Modulation Options* block contains the option to enable or disable code modulation, assuming small interferences. Furthermore, it allows the user to specify the term of convergence of the correlator, its spacing and its type. The function of the correlator in GNSS systems is to match the incoming signal from the satellite with a replica produced in the receiver in order to acquire the signal and to be able to decrypt the information contained in it.
- *Receiver Option* block consents to define the noise temperature of the receiver, as well as its noise bandwidth and density.
- *Bias* block lets the user to input several biases regarding power, height adjustment, reflected power and phase bias coefficients. It also allows to define biases for the fitting function and to plot intermediary results.
- *Antenna* block consists on the actual positioning of the antenna, thus concerning boresight azimuth and elevation as well as the axial rotation. It contains also the model of the antenna, the option of radomes and the possibility to switch to LHCP gain. In particular this block of options is decisive to instruct the program on which predefined gain data that has to be loaded. In an appropriate folder there have to be in fact the necessary data to reconstruct the antenna gain. In this case the gain of the antennas used in the experiment and in the simulation was taken from the graph presented in Figure 18 and Figure 23. The file is usually formatted with the gain offset at the beginning and the normalized gains following, so the program can easily reproduce the correct trend. The gain is unique for each antenna and it has a decisive impact on the amplitude of the SNR.
- *Surface* block consents to choose the materials of a maximum of three layers through which the signal travels. As the name said, the purpose of this structure is to define the behavior of the GNSS wave when it reaches the reflecting surfaces. In particular, it is possible to define a top material a bottom material, and if needed additional middle ones. In the simulation, only two layers have been used: air and sea water. Some materials are already implemented into the program allowing the user to just input their names. For other material compositions additional options have to be entered, such as density and temperature. By calling external functions it is possible to define the layout of the material. For this experiment, homogenous materials have been used, but in case of the presence of additional middle layers, these can be inserted supposing a layered surface. This also allows adding on top of the bottom layer a number of other materials with defined thickness, density, moisture and temperature. Moreover, it is

possible to design a surface profile in term of parametric formulas for given coefficients or to express two contiguous layer as a matter of interpolation between different stacks. This would allow a gradient transition between the layer smoothing sharp discontinuities. In this section it is also possible to set the slope of the surface that in other word can also be intended as the tilting angle of the antenna facing the signal. Furthermore the geometry can be modeled and the number of specular reflections that create multipath.

- *Satellite* block contains useful parameters to define physical constraint and position of the satellites sending the signal. One value defines the number of observations, i.e. the number of points captured by the hypothetical receiver. It has to be kept in mind that with the increasing of the height the frequency of the SNR is supposed to augment as well. Hence, it is appropriate to raise the number of observations in order to fulfill the Nyquist -Theorem, i.e. for each sinusoidal cycle there have to be at least 2 observations. An elevation and azimuth mask is also applicable in order to define the position of the satellite and its interaction with the antenna gain pattern.

Once these blocks are set, the program is able to define permittivity, phasor of the signal, hence its power as well as the SNR and the error on code and carrier pseudorange due to multipath. Lastly it is possible to disable code modulation for small delay reflections to speed up the calculation since the error due to this effect is not significant.

In order to observe the behavior of the simulator with a wider range of input, heights from 2 to 30 meters were simulated. Moreover the number of point was incremented and the elevation gap was modified. Figure 105 depict five different sub-configuration implemented for SEA2 (similar behavior were obtained for other antennas): all the data were detrended before LSSA analysis so to assume suitable input data. As it is shown in the graph, increasing the number of point does not affect the result strongly. Only 3 points are slightly different for the case with 500 observations. This allows asserting that the usage of 500 points is a good compromise between accuracy and speed in calculations. For this case, around 200 seconds were necessary to complete the test while when 2000 observations were used, the time needed was over 900 seconds. On the other hand, changing the elevation gap affects with more importance the results. By increasing the elevation the results tend to fluctuate more for SEA2. This could be due to the fact that the same amount of points is spread in a wider interval. For the other configurations the behavior is similar but the trend is below the one representing the smaller elevation gap. These could highlight the fact that in case of high power coming from the receiver, using wider elevation intervals allow to utilize also those fluctuation that still are present at higher elevations. On the other hand, when the signal is low the higher elevation does not contain useful information to the analysis and this could result slightly misleading. Nevertheless, the trend to increase seems to be

affecting all the antennas not regarding the number of observations or the elevation interval. This could be due to an internal precision limit of the simulator or of the LS Periodogram processing itself.

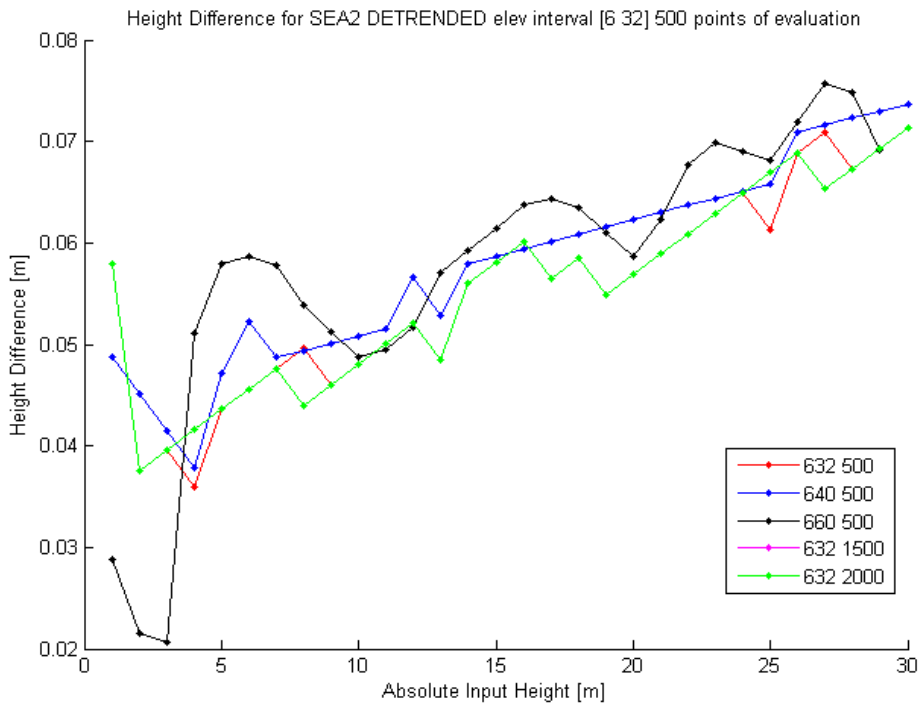


Figure 105: Performance overview for LEICA AX 1202 GG (detrended)

The same test is been carried out without detrending the simulated data, as can be observed in Figure 106. The graph show a highly fluctuating error that reduces with elevation while the mean value remain almost constant around 5 cm. Even in this case there is a slight increment in the mean but it is almost covered by the error introduced by the not detrended data. Figure 105 and Figure 106 are consistent with the trend shown in Figure 41, where a smaller interval was presented but with double the resolution.

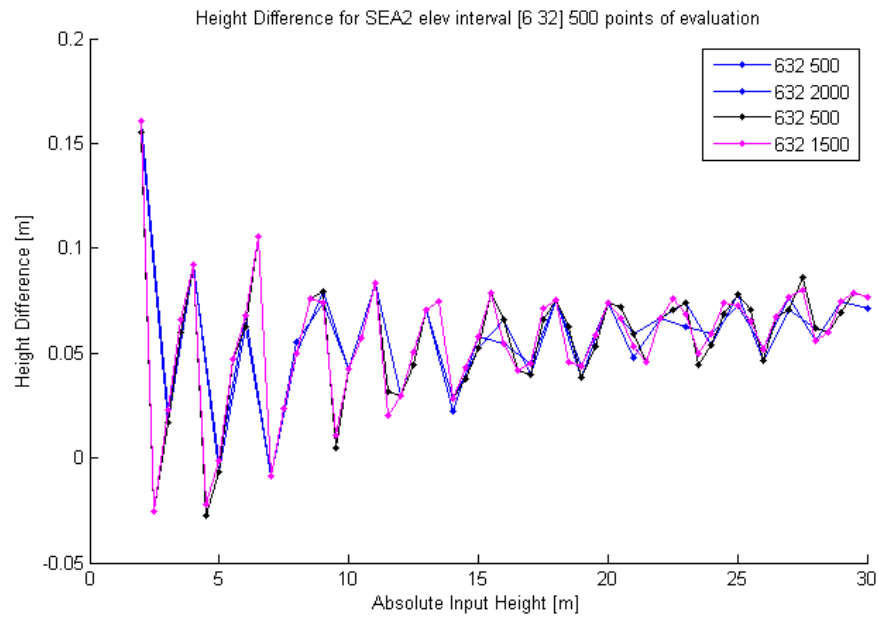


Figure 106: Performance overview for LEICA AX 1202 GG (trended)

9.2. Scripts

The following link takes to a Google Drive folder containing the scripts used. Not all of them are available since part of them are property of Chalmers University of Technology:

<https://drive.google.com/folderview?id=0B-NhRvY4KWEJNXI0eDVQYkd6LU0&usp=sharing>

Acknowledgments

This research project would not have been possible without the support of many people. The author wishes to express her gratitude to her supervisor, Prof. Dr. Paolo Tortora who was helpful and offered invaluable assistance, support and guidance in many situations and Prof. Alessandro Avanzi, for his instantaneous support and helpfulness. Deepest gratitude are also due to the members of the “Swedish supervisory committee” from Chalmers University of Technology, Prof. Dr. Rüdiger Haas and specially PhD student Johan Löfgren without whose knowledge and assistance this study would not have been successful. Thanks also to the academic staff at the Onsala Space Observatory and at the Department of Earth and Space Sciences for providing all the useful data for the completion of this thesis and for always being kind and helpful.

~ o ~

Infinite thanks to his family, lil’ Hully the Blonde, elder Tia the Wise, Cristina, Andrea and Michelle (The Liu one) for the multifaceted help and understanding they have provided so far in his life. Thanks to the relatives that have always take good care of him.

Special thanks also to all his graduate friends, especially group members: Buccio the Pragmatic, Albi the Outsider, Campa the Saint (Thomas), Giò the Mechanic, the good old Fed di Nic (with a Long Island), the gym-mate “Magic” Mike for giving him good time both inside and outside the university, as well as Albi L. and his study session. Thanks to the pro Albi Ferr. (“LAAAAG”) for his imba tactics (I got all in cd), for the nice words through Skype, for letting the author feed but most of all for his constant and prodigal help and support during his Erasmus. Not forgetting the ladies: Sarah, Cri, Vero, Bene and in particular Rebe,

which stood out from the engineering environment. Many thanks also to all the “northern” friends, Rob (don’t touch my car), Kate for being always being there, Gab and the Franch family for the food, the electric power but moreover for the kindness and happiness with whom they have always treated me. Thanks to Greg, Max, Jessica and Barbara for maintaining the contact alive, and to Jacuz and Ale for the holidays. Thanks for the always growing group of the Pacate, in particular Eli, Michelle and Jex for the good time they always provide.

The author wishes to express his love and gratitude to his flatmates: his “twin” brother Vale, for everything, there is too much to be thankful for, and to Valentina, for being the wise component of our trio.

Special thanks to miss Roxana K. for the ginger tea, the failed movie night and for the support given during this last months of madness, for explaining that Arabic is not Iranian-Persian and for her loving kindness.

Thanks to 4200 corridor, in particular to Mr. Anton Palmquist (palm branch) for the cooking session, and for being only my Swedish mate. Thanks to Alfredo and the dinners, the Erasmus friends but in special to Pau (Jolo, yes...) for her support, her kindness, her vitality and smile in every situation! Thanks to the guys from Best summer weeks, in particular to Rafal for the good time and Genya for being my guide and bodyguard. Thanks to the friends from Overseas, i.e. Mareike, Sophia, Haeri and Brad as well as Fung Tin Kwan and his daily escort in HK. Thanks to his spell- and life-checker, miss Merrion B., and to the troublemaker miss Amy B., he owes them a lot. The author wishes to express his gratitude to the Rizzi families from overseas, for their help and kindness, as well as to Mr. Andrew F.

The author would also like to convey thanks to CTH and Sweden in general, from the free flow coffee and tea that kept him awake during many night session in the thesis room. Thanks to Mesh-up for being the place where I spent most of my forth year with many friends, to John Shepherd, H to the Husky “Husky”, Trump, Tobi Wan, TB and more for the entertainment.

Thanks also to all the people that walked alongside with the author, sharing knowledge, ideas, hopes, projects, laughs, time and also feelings.

May the force be with you all, and thank you again!

“The Day lasts forever, only the planets rotate”